공학박사학위논문

큰 진폭 진동의 유체-구조물 상호 작용과 수동 제어

Fluid-structure interactions of large-amplitude vibrations and their passive controls

2017 년 8 월

서울대학교 대학원

기계항공공학부

김 우 진

큰 진폭 진동의 유체-구조물 상호 작용과 수동 제어

Fluid-structure interactions of large-amplitude vibrations and their passive controls

지도교수 최 해 천

이 논문을 공학박사 학위논문으로 제출함

2017 년 7 월

서울대학교 대학원

기계항공공학부

김 우 진

김우진의 공학박사 학위논문을 인준함

2017 년 7 월

위 원 장 : 김 호 영

부위원장 : 최 해 천

위 원 : 방 형 민

위 원 : 최 정 인

위 원 : 김 대 겸

Fluid-structure interactions of large-amplitude vibrations and their passive controls

Woojin Kim
Department of Mechanical & Aerospace Engineering
Seoul National University

Abstract

In the present study, we present a weak coupling approach for fluid-structure interaction with low density ratio (ρ) of solid to fluid and conduct unsteady three-dimensional simulations of flows around structures: elastically mounted rigid circular and helically twisted elliptic (HTE) cylinders in the super-upper branch, flexible circular and HTE cylinders in a linearly sheared flow, and the Tacoma Narrows Bridge.

For accurate and stable solutions in a weak coupling approach, we introduce predictors, an explicit two-step method and the implicit Euler method, to obtain provisional velocity and position of fluid-structure interface at each time step, respectively. The incompressible Navier-Stokes equations, together with these provisional velocity and position at the fluid-structure interface, are solved in an Eulerian coordinate using an immersed-boundary finite-volume method on a staggered mesh. The dynamic equation of an elastic solid-body motion, together with the hydrodynamic force at the provisional position of the interface, is solved in a Lagrangian coordinate using a finite element method. Each governing equation for fluid and structure is implicitly solved using second-order time integrators. The overall second-order temporal accuracy is preserved

even with the use of lower-order predictors. A linear stability analysis is also conducted for an ideal case to find the optimal explicit two-step method that provides stable solutions down to the lowest density ratio. With the present weak coupling, three different fluid-structure interaction problems were simulated: flows around an elastically mounted rigid circular cylinder, an elastic beam attached to the base of a stationary circular cylinder, and a flexible plate ($\rho = 0.678$), respectively. The lowest density ratios providing stable solutions are searched for the first two problems and they are much lower than 1 (ρ_{min} = 0.21 and 0.31, respectively). The simulation results agree well with those from strong coupling suggested here and also from previous numerical and experimental studies, indicating the efficiency and accuracy of the present weak coupling.

Flow around an elastically mounted rigid circular cylinder is simulated at the mass ratio of 2, the reduced velocity of 6, the damping ratio of 0, and the Reynolds number of 4200. Vibration with the transverse displacement amplitude of $1.19D$ is induced by large pressure difference between the upper and lower sides, where D is the diameter of a circular cylinder or square root of the product of the lengths of the major and minor axes of the HTE cylinder: pressure is high on the side opposite to the moving direction of the cylinder due to the impingement of flow induced by starting vortices in the shear layers evolved from the front and rear sides but low on the other side due to the flow acceleration and separation delay. To suppress large amplitude vibration, a parametric study is conducted for the wavelength (λ_H) and aspect ratio (AR_H) of an elastically mounted rigid HTE cylinder. For the elastically mounted rigid HTE cylinder with $AR_H = 2.6$ and $\lambda_H = 10D$, flow-induced vibration is completely suppressed, and the mean drag coefficient is significantly decreased compared to that for an elastically mounted rigid circular cylinder but slightly higher than

that for a stationary circular cylinder.

Flow around a flexible circular cylinder is simulated at the mass ratio of 7.64, tension coefficient of 4.55, bending coefficient of 9.09, the ratio of the maximum to minimum velocity of 3.67, the ratio of length to diameter of 200, and the Reynolds number of 330 based on the maximum velocity in a linearly sheared inflow. Lock-in occurs for three frequencies of 0.148, 0.162, and 0.174 in the high velocity region, which induces multi-mode response and traveling waves propagating from the high velocity region to low velocity region. The transverse displacement amplitude is less than $1D$ and standing waves as well as traveling waves are observed. In the wake, two single vortices shed per cycle (2S mode). Flow around a flexible circular cylinder is simulated at the mass ratio of 2.55, tension coefficient of 5, bending coefficient of 10, the ratio of the maximum to minimum velocity of 9, the Reynolds number of 4000 based on the maximum velocity in a linearly sheared inflow. A flexible circular cylinder vibrates with the wavelength two times the spanwise domain size (mode 1). The transverse displacement amplitude is greater than $2D$ and streamwise displacement severely fluctuates near the middle of a flexible circular cylinder. Strong starting vortices are generated from the shear layers and located near the side opposite to the moving direction of the cylinder. For both cases of multi-mode and single-mode responses, the flexible HTE cylinder with $AR_H = 2.6$ and $\lambda_H = 10D$ completely suppresses flow-induced vibration and reduces the deflection in the streamwise direction.

Flow around the Tacoma Narrows Bridge is simulated at the Reynolds number of 300 based on the height of the deck. Vortex shedding behind the Tacoma Narrows Bridge is alternatively generated along the spanwise and transverse directions when the Tacoma Narrows Bridge torsionally vibrates with the wavelength of L_T, where L_T is the length of the Tacoma Narrows Bridge. Torsional

vibration of the Tacoma Narrows Bridge interacts with leading edge vortices: higher angle of attack of the cross section of the deck induces a stronger leading edge vortex, and again stronger leading edge vortices generate higher moment on the deck. The vortex shedding frequency matches well with the torsional natural frequency induced by the cables although the matched frequency is much lower than the frequency of vortex shedding for flow around a stationary Tacoma Narrows Bridge because a leading edge vortex stays longer near the leading edge as the angle of attack of the cross section of the deck is higher.

Keywords: fluid-structure interaction, large amplitude vibration, vortex, bluff body, passive control

Student number: 2010-20661

Contents

Abstract i

Contents v

List of Figures viii

Nomenclature xix

Chapter

1 Introduction 1

2 A weak-coupling immersed boundary method for fluid-structure interaction with low density ratio of solid to fluid 4

2.1 Motivations and objectives 4

2.2 Numerical method 8

2.2.1 Weak coupling vs. strong coupling 8

2.2.2 Numerical method for fluid flow 9

2.2.3 Numerical method for the motions of rigid and elastic bodies 11

2.2.4 Predictors for the motion of fluid-solid interface and their numerical stability 13

2.2.5 Strong coupling algorithm 18

2.3 Numerical examples 21

2.3.1 Vortex-induced vibration of a rigid circular cylinder . . . 21

2.3.2 Vortex-induced vibration of an elastic beam 25

2.3.3 Bending of a flexible plate 27

2.4 Summary 31

3 Vortex-induced vibrations of an elastically mounted rigid circular cylinder and flexible circular cylinder, and controls for them 45

3.1 An elastically mounted rigid cylinder in a uniform current . . . 45

3.1.1 Motivations and objectives 45

3.1.2 Computational details 48

3.1.3 Vortex-induced vibration of an elastically mounted rigid circular cylinder at the super-upper branch 50

3.1.4 Flow over the elastically mounted rigid helically twisted elliptic cylinder 53

3.2 A flexible cylinder in a linearly sheared current 57

3.2.1 Motivations and objectives 57

3.2.2 Computational details 59

3.2.3 Multi-mode response of a flexible circular cylinder and its control 61

3.2.4 Single-mode response of a flexible circular cylinder and its control 67

3.3 Summary 69

4 Collapse of the Tacoma Narrows Bridge 106

4.1 Objectives 106

4.2 Computational details 107

4.3 Flow-induced vibration of the Tacoma Narrows Bridge 112

4.4 Summary 115

References **122**

List of Figures

Figure

2.1 Procedures of (a) weak coupling with predictors and (b) strong coupling using an iterative scheme with an under-relaxation scheme. Here, the Navier-Stokes equations are solved with a linearlized fully implicit method, and the dynamic equation for an elastic solid-body motion is iteratively solved with a fully implicit method. 33

2.2 Schematic diagram of a discrete-forcing IB method (Kim *et al.*, 2001). 34

2.3 Lowest density ratio from the present stability analysis for weak coupling with $\chi = 0$: ——, $\rho_{min}/\max_i \mu_i = \left(-3\xi + \sqrt{9\xi^2 - 40\xi + 40}\right)/8$ for $\xi \leq 3/8$; ——, $4\xi/3$ for $\xi > 3/8$. 35

2.4 Schematic diagram of the computational domain and boundary conditions for the simulation of flow around an elastically mounted rigid circular cylinder. 36

2.5 Trajectory of the center of an elastically mounted rigid circular cylinder with $\rho = 4/\pi$: ——, present simulation (weak coupling with $\xi = 1$ and $\chi = 0.5$); – – –, present simulation (strong coupling with $\chi = 0.5$); – - –, Blackburn & Karniadakis (1993); - - - - -, Yang *et al.* (2008). 37

2.6 Contours of the instantaneous vorticity around an elastically mounted rigid circular cylinder, obtained from weak coupling with $\xi = 1$ and $\chi = 0.5$. 38

2.7 Numerical accuracy of the present method (weak coupling with $\xi = 3/4$ and $\chi = 0$) for flow around an elastically mounted rigid circular cylinder: ■, maximum transverse displacement; ♦, maximum transverse velocity. The dashed line indicates $\gamma_N = 2$. . . 39
2.8 Schematic diagram of the computational domain and boundary conditions for the simulation of flow around an elastic beam attached to base of a stationary circular cylinder in a channel. . . 40
2.9 Time traces of the point A (in figure 2.8) of an elastic beam for $\rho_s^0 = \rho_f = 1000\,\mathrm{kg}\,/\,\mathrm{m}^3$: ——, present study (weak coupling with $\xi = 1$ and $\chi = 0.5$); – – –, present study (strong coupling with $\chi = 0.5$); – - –, Turek & Hron (2006). 41
2.10 Schematic diagram of the computational domain and boundary conditions for the simulation of flow around a flexible plate. . . 42
2.11 Time traces of the streamwise and transverse displacements of the point A in figure 2.10: ——, weak coupling with $\xi = 1$ and $\chi = 0$; – – –, weak coupling with $\xi = 1$ and $\chi = 0.5$; – - –, weak coupling with $\xi = 3/4$ and $\chi = 0$. 43
2.12 Instantaneous vortical structures around a flexible plate, obtained from weak coupling with $\xi = 1$ and $\chi = 0.5$. 44
3.1 Schematic diagram of computational domain and boundary conditions for the simulation of flow around an elastically mounted rigid cylinder. 72
3.2 Time histories of the transverse and streamwise displacements of the center and lift and drag coefficients for an elastically mounted rigid circular cylinder at $U^* = 6$: (a) Y_C/D and C_L; (b) X_C/D and C_D. Red line, Y_C/D; blue line, C_L; orange line, X_C/D; green line, C_D. 73

3.3 Transverse and streamwise displacement amplitudes with the reduced velocity: (a) A_X/D; (b) A_Y/D. Black circle, present simulation; pink left triangle, Jauvtis & Williamson (2004); orange right triangle, Blevins & Coughran (2009); blue delta, Zhao *et al.* (2012); green square, Gsell *et al.* (2016); red diamond, Kang *et al.* (2017). 74

3.4 Transverse displacement frequency and time averaged phase value of the phase difference between the streamwise and transverse displacements with the reduced velocity: (a) $f_Y D/U$; (b) $\bar{\theta}_{dis}$. Black circle, present simulation; pink left triangle, Jauvtis & Williamson (2004); blue delta, Zhao *et al.* (2012); green square, Gsell *et al.* (2016); red diamond, Kang *et al.* (2017). 75

3.5 Elastically mounted rigid circular cylinder: (a) Trajectory of the center; (b) time traces of the transverse and streamwise displacements of the center and half of the lift and drag coefficients; (c) contours of the instantaneous spanwise vorticity and pressure and velocity vector fields. ① $tU/D = 56.73$; ② 57.38; ③ 58.31; ④ 59.15; ⑤ 60.31; ⑥ 60.77. Arrows at the center of the circular cylinder indicate the velocity of the circular cylinder and arrows with the magnitude of U are given at the bottom left of each contour. 76

3.6 Schematic diagram of the helically twisted elliptic (HTE) cylinder. 77

3.7 Root mean square of the transverse displacement of the center and the lift coefficient of elastically mounted rigid circular and HTE cylinders with the wavelength and aspect ratio: (a) Y_{Crms}/D; (b) C_{Lrms}. Green diamond, the HTE cylinder with the aspect ratio $(AR_H) = 1.3$; blue square, $AR_H = 2.0$; red circle, $AR_H = 2.6$; black solid line, the circular cylinder; black dashed line, a stationary circular cylinder. 78

3.8 Mean streamwise displacements of the center and drag coefficients of elastically mounted rigid circular and HTE cylinders with the wavelength: (a) $\bar{X}_C/D$; (b) $\bar{C}_D$. Green diamond, the HTE cylinder with $AR_H = 1.3$; blue square, $AR_H = 2.0$; red circle, $AR_H = 2.6$; black solid line, the circular cylinder; black dashed line, a stationary circular cylinder. 79

3.9 Instantaneous vortical structures around stationary cylinders ((a) and (b)) and elastically mounted rigid cylinders ((c)–(e)) from the side view: (a) circular cylinder; (b) HTE cylinder with $AR_H = 1.3$ and $\lambda_H/D = 4$; (c) circular cylinder; (d) HTE cylinder with $AR_H = 1.3$ and $\lambda_H/D = 4$; (e) HTE cylinder with $AR_H = 2.6$ and $\lambda_H/D = 10$. 80

3.10 Instantaneous vortical structures around stationary cylinders ((a) and (b)) and elastically mounted rigid cylinders ((c)–(e)) from the top view: (a) circular cylinder; (b) HTE cylinder with $AR_H = 1.3$ and $\lambda_H/D = 4$; (c) circular cylinder; (d) HTE cylinder with $AR_H = 1.3$ and $\lambda_H/D = 4$; (e) HTE cylinder with $AR_H = 2.6$ and $\lambda_H/D = 10$. 81

3.11 Power spectra density for an elastically mounted rigid cylinder: (a) circular cyilnder; (b) HTE cylinder with $AR_H = 1.3$ and $\lambda_H/D = 4$; (c) HTE cylinder with $AR_H = 2.6$ and $\lambda_H/D = 10$. blue line, C_L; azure line, Y_C/D; green line, v/U at $(x, y, z) = (5D, 0, 0)$; pink line, v/U at $(x, y, z) = (5D, 0, L_z/2)$ (circular) or $(5D, 0, \lambda_H/2)$ (HTE); red line, C_D; orange line, X_C/D. 82

3.12 Root mean square of (a) the sectional lift and (b) drag coefficients for elastically mounted rigid cylinders. Black line, circular cylinder; red line, HTE cylinder with $AR_H = 1.3$ and $\lambda_H/D = 4$; blue line, HTE cylinder with $AR_H = 2.6$ and $\lambda_H/D = 10$. 83

3.13 (a) Mean sectional lift and (b) drag coefficients for elastically mounted rigid cylinders. Black line, circular cylinder; red line, HTE cylinder with $AR_H = 1.3$ and $\lambda_H/D = 4$; blue line, HTE cylinder with $AR_H = 2.6$ and $\lambda_H/D = 10$. 84

3.14 Single-mode and multi-mode response regions with the ratio of the change of velocity to average velocity ($\triangle U/U_{avg}$) and number of modes in excitation frequency band (N_s) (Vandiver *et al.*, 1996). 85

3.15 Schematic diagram of computational domain and boundary conditions for the simulation of flow around a flexible cylinder. . . . 86

3.16 Mean streamwise displacement and root mean square of transverse displacement along the spanwise direction for a flexible circular cylinder: (a) $\bar{\zeta}_x/D$; (b) ζ_{yrms}/D. Red line, present simulation with the buffer region; blue line, present simulation without the buffer region; black line, Bourguet *et al.* (2011). 87

3.17 Time histories of the transverse displacement along the spanwise direction for flexible cylinders: (a) circular cylinder; (b) HTE cylinder with $AR_H = 1.3$ and $\lambda_H/D = 4$; (c) HTE cylinder with $AR_H = 2.6$ and $\lambda_H/D = 10$. 88
3.18 Time histories of the streamwise displacement along the spanwise direction for flexible cylinders: (a) circular cylinder; (b) HTE cylinder with $AR_H = 1.3$ and $\lambda_H/D = 4$; (c) HTE cylinder with $AR_H = 2.6$ and $\lambda_H/D = 10$. 89
3.19 Time histories of the streamwise displacement fluctuation along the spanwise direction for flexible cylinders: (a) circular cylinder; (b) HTE cylinder with $AR_H = 1.3$ and $\lambda_H/D = 4$; (c) HTE cylinder with $AR_H = 2.6$ and $\lambda_H/D = 10$. 90
3.20 Mean streamwise displacement and sectional drag coefficient for flexible cylinders: (a) $\bar{\zeta}_x/D$; (b) $\bar{C}_{Ds}$. Black line, circular cylinder; blue line, HTE cylinder with $AR_H = 1.3$ and $\lambda_H/D = 4$; red line, HTE cylinder with $AR_H = 2.6$ and $\lambda_H/D = 10$. 91
3.21 Root mean square of the transverse displacement and sectional lift coefficient for flexible cylinders: (a) ζ_{yrms}/D; (b) $\bar{C}_{Lsrms}$. Black line, circular cylinder; blue line, HTE cylinder with $AR_H = 1.3$ and $\lambda_H/D = 4$; red line, HTE cylinder with $AR_H = 2.6$ and $\lambda_H/D = 10$. 92
3.22 Instantaneous vortical structures around a flexible circular cylinder from the (a) side and (b) front views, the flexible HTE cylinder with $AR_H = 1.3$ and $\lambda_H/D = 4$ from the (c) side and (d) front views, and the flexible HTE cylinder with $AR_H = 2.6$ and $\lambda_H/D = 10$ from the (e) side and (f) front views. 93

3.23 Contours of the instantaneous spanwise vorticity around a flexible circular cylinder: (a) $z/D = 7$; (b) 50; (c) 149. 94
3.24 Contours of the instantaneous spanwise vorticity around the flexible HTE cylinder with $AR_H = 1.3$ and $\lambda_H/D = 4$: (a) $z/D = 6$; (b) 8; (c) 50; (d) 52; (e) 150; (f) 152. 95
3.25 Contours of the instantaneous spanwise vorticity around the flexible HTE cylinder with $AR_H = 2.6$ and $\lambda_H/D = 10$: (a) $z/D = 5$; (b) 10; (c) 45; (d) 50; (e) 145; (f) 150. 96
3.26 Power spectra density of the transverse displacement $(a–c)$, sectional lift coefficient $(d–f)$, and transverse fluid velocity at $x/D = 20$ and $y/D = 0$ $(g–i)$ for flexible cylinders: ζ_y/D for (a) a circular cylinder, (b) the HTE cylinder with $AR_H = 1.3$ and $\lambda_H/D = 4$, (c) the HTE cylinder with $AR_H = 2.6$ and $\lambda_H/D = 10$; C_{Ls} for (d) a circular cylinder, (e) the HTE cylinder with $AR_H = 1.3$ and $\lambda_H/D = 4$, (f) the HTE cylinder with $AR_H = 2.6$ and $\lambda_H/D = 10$; v/U for (g) a circular cylinder, (h) the HTE cylinder with $AR_H = 1.3$ and $\lambda_H/D = 4$, (i) the HTE cylinder with $AR_H = 2.6$ and $\lambda_H/D = 10$. 97
3.27 Spanwise evolution of selected temporal mode phase angles for flexible cylinders: (a) circular cylinder; (b) HTE cylinder with $AR_H = 1.3$ and $\lambda_H/D = 4$. 98

3.28 Partial HTE cylinder with $AR_H = 2.6$ and $\lambda_H/D = 10$: (a) schematic diagram; instantaneous vortical structures around the flexible partial HTE cylinder from the (b) side and (c) front views. The partial HTE cylinder is composed of the HTE cylinder from $z/D = 0$ to 80, a circular cylinder from $z/D = 90$ to 190, and transition region from $z/D = 80$ to 90 and 190 to 200. In the transition region, the major and minor axes linearly change from the HTE cylinder to a circular cylinder and vice versa. . . 99

3.29 Partial HTE cylinder with $AR_H = 2.6$ and $\lambda_H/D = 10$: Time histories of (a) the streamwise displacement (ζ_x), (b) streamwise displacement fluctuation $(\zeta_x - \bar{\zeta_x})$, and (c) transverse displacement (ζ_y) along the spanwise direction. 100

3.30 Mean streamwise displacement and sectional drag coefficient and root mean square of the transverse displacement and sectional lift coefficient for flexible cylinders: (a) $\bar{\zeta_x}/D$; (b) $\bar{C}_{Ds}$; (c) ζ_{yrms}/D; (d) C_{Lsrms}. Black line, circular cylinder; blue line, HTE cylinder with $AR_H = 2.6$ and $\lambda_H/D = 10$; red line, partial HTE cylinder with $AR_H = 2.6$ and $\lambda_H/D = 10$. 101

3.31 Power spectra density of (a) the transverse displacement, (b) sectional lift coefficient and (c) transverse fluid velocity at $x/D = 20$ and $y/D = 0$, and (d) the spanwise evolution of selected temporal mode phase angles for the flexible partial HTE cylinder with $AR_H = 2.6$ and $\lambda_H/D = 10$. 102

3.32 Time traces of the transverse and streamwise displacements along the spanwise direction for flexible circular and HTE cylinders with $AR_H = 2.6$ and $\lambda_H/D = 10$: (a) ζ_y and (b) ζ_x of a circular cylinder; (c) ζ_y and (d) ζ_x of the HTE cylinder. 103

3.33 Instantaneous vortical structures around a flexible circular cylinder from the (a) front and (b) side views and the flexible HTE cylinder with $AR_H/D = 2.6$ and $\lambda_H/D = 10$ from the (c) front and (d) side views. 104
3.34 Contours of the instantaneous spanwise vorticity for flexible circular and HTE cylinders with $AR_H = 2.6$ and $\lambda_H/D = 10$: ω_z on the xy plane $(z/D = 25)$ for the circular cylinder at (a) tU_{max}/D = 13.6, (b) 15.9, (c) 18.5, (d) 21.1, and (e) 23.6; ω_z on the (f) $z/D = 20$, (g) 22.5, (h) 25, and (i) 27.5 at $tU_{max}/D = 49.3$ for the HTE cylinder with $AR_H = 2.6$ and $\lambda_H/D = 10$. 105
4.1 Schematic diagram of computational domain and boundary conditions for the simulation of flow around the Tacoma Narrows Bridge. Here, the effects of the cables, hangers, and towers are not considered for the simulation of flow around the Tacoma Narrows Bridge. 116
4.2 Theoretical natural frequencies of the cable and deck for the transverse and rotational motions with the mode. 117
4.3 Time traces of the rotational angle, sectional moment coefficient, transverse displacement, sectional lift coefficient, and transverse velocity along the spanwise direction: (a) θ_C (°); (b) C_{Ms}; (c) Y_C/h_T; (d) C_{Ls} ; (e) v/U at $x/h_T = 5$ and $y = 0$. 118
4.4 Instantaneous vortical structures around the Tacoma Narrows Bridge: (a) $tU/h_T = 45.5$; (b) 52.4; (c) 58.8; (d) 64.0; (e) 70.2; (f) 76.7; (g) 82.6. 119
4.5 Contours of the instantaneous spanwise vorticity at $z/L_T = 0.25$: (a) $tU/h_T = 45.5$; (b) 52.4; (c) 58.8; (d) 64.0; (e) 70.2; (f) 76.7; (g) 82.6. 120

4.6 Contours of the instantaneous spanwise vorticity at $z/L_T = 0.75$: (a) $tU/h_T = 45.5$; (b) 52.4; (c) 58.8; (d) 64.0; (e) 70.2; (f) 76.7; (g) 82.6. 121

List of Tables

Table

2.1 Lowest density ratios for stable solutions depending on the predictors, and the values of origin of oscillations for an elastically mounted rigid circular cylinder. Here, WC and SC denote the weak and strong coupling, respectively, and does the divergence of solution. 23

2.2 Origin of oscillations and oscillation frequency of an elastically mounted rigid circular cylinder with $\rho = 4/\pi$. Here, $\bar{X}_C$ is the origin of oscillations. 24

2.3 Mean drag coefficient and Strouhal number for $\rho_s^0 = \rho_f = 1000\,\mathrm{kg}\,/\,\mathrm{m}^3$. 27

2.4 Lowest density ratios for stable solutions depending on the predictors, and the values of mean drag coefficient. Here, WC and SC denote the weak and strong coupling, respectively, and $\times$ does the divergence of solution. 28

2.5 Mean drag coefficients and mean streamwise and transverse displacements of the point A ($\rho_s^0/\rho_f = 0.678$). Here, WC denotes weak coupling and $\times$ denotes the divergence of solution. 30

Nomenclature

Roman Symbols

a_q	complex modal coefficient associated with the qth mode
a_T	thickness of the railings
A_T	area of the section of the cable
A_X, A_Y	streamwise and transverse displacement amplitudes
AR_H	aspect ratio of elliptic cylinder
b_T	thickness of the deck
c_s	damping coefficient
C	unknown constant
C_s	stability constant
C_D	drag coefficient
C_{Ds}	sectional drag coefficient
C_L	lift coefficient
C_{Ls}	sectional lift coefficient
C_{Ms}	sectional moment coefficient
CFL	Courant-Friedrichs-Lewy
d	structural displacement
$\dot{d}$	structural velocity
$\ddot{d}$	structural acceleration
$\hat{d}$	intermediate structural displacement
$\hat{\dot{d}}$	intermediate structural velocity
$\hat{\ddot{d}}$	intermediate structural acceleration
$\tilde{d}$	provisional displacement of fluid-structure interface

$\tilde{\dot{d}}$	provisional velocity of fluid-structure interface
$\bar{d}_i$	scalar coefficient
D	diameter of a circular cylinder
$\boldsymbol{D_I}$	discrete divergence operator for the interior fluid velocities
$\boldsymbol{D_\Gamma}$	discrete divergence operator for the interface fluid velocities
E_{mn}	Green-Lagrangian strain tensor
E_s	Young's modulus
f_1	the first mode natural frequency
f_i	momentum forcing
f_q	frequency associated with the qth mode
f_N	natural vibration frequency
F_{im}	deformation gradient tensor
F_H	hydrodynamic force
F_D	drag force
F_L	lift force
$\boldsymbol{F_H}$	hydrodynamic force vector
$\boldsymbol{g}$	gravitational acceleration vector
g_{exact}	exact solution
g_N	numerical solution
G_T	shear modulus of the deck
$\boldsymbol{G}$	gravitational force vector
$\boldsymbol{G_I}$	discrete gradient operator for interior pressure
h_b	thickness of a beam
h_p	thickness of a plate
h_N	uniform grid spacing of the N^2 mesh
h_T	height of the deck

H_{0T}	spanwise component of the tension of the cables
H_p	height of a plate
$\boldsymbol{H_\Gamma}$	discrete operator representing the hydrodynamic force from pressure on the fluid-structure interface
I_c	area moment of inertia
I_{cx}	area moment of inertia in the streamwise direction
I_{cy}	area moment of inertia in the transverse direction
I_T	linear density of the moment of inertia of the cross section
IB	immersed boundary
k	iteration index
k_s	spring constant
k_T	torsional constant of the deck
l_T	half width of the deck
L	characteristic length
L_b	length of a beam
L_{cT}	length of the cable
L_x, L_y, L_z	streamwise, transverse, and spanwise domain sizes
L_T	length of the deck
m^*	mass ratio
m_{cs}	cylinder mass per unit length
m_s	solid mass
m_T	mass of the cable per unit length
M_T	mass of the deck per unit length
$\boldsymbol{M}$	mass matrix
$\boldsymbol{M_A}$	discrete representation of the added mass operator
n	time step
n_e	number of nodes per element

n_i	surface-normal vector
N	number of grid points
N_s	the number of potentially responding modes within the vortex-shedding frequency bandwidth resulting from a sheared flow
N_I	shape function
p	pressure
q	mass source/sink
Re	Reynolds number
$\boldsymbol{R}(\boldsymbol{d})$	internal force vector
S_T	position of the cables
SC	strong coupling
t	time
T_c	tension
T_s	sampling period
u_i (u, v, w)	streamwise, transverse, and spanwise velocity components in the Cartesian coordinates
$\hat{u}_i$	intermediate velocity
$\dot{\boldsymbol{u}}_{\boldsymbol{\Gamma}}$	fluid acceleration vector on the interface
U	characteristic velocity
U^*	reduced velocity
U_{avg}	average velocity
U_{max}	maximum velocity
U_{min}	minimum velocity
$\boldsymbol{v}_i$	eigenvectors of M_A
V_s	solid volume
V^0	initial volume of an elastic body
W	strain energy density function

WC	weak coupling
x_i (x, y, z)	streamwise, transverse, and spanwise directions in the Cartesian coordinates
X_i	current position vector
X_m^0	initial position vector
X_C, Y_C	streamwise and transverse displacements of the center
$\dot{X}_C, \dot{Y}_C$	streamwise and transverse velocities of the center
$\ddot{X}_C, \ddot{Y}_C$	streamwise and transverse accelerations of the center

Greek Symbols

α_m, α_f, β, γ	coefficients of the generalized-α method
γ_N	order of accuracy
Γ	fluid-structure interface
δ_{ij}	Kronecker delta tensor
Δt	time step
ΔU	change of velocity
ϵ	tolerance level
ζ	damping ratio
ζ_x, ζ_y	streamwise and transverse displacements of the center of a flexible cylinder
θ_C	rotational angle of the center
λ_i	amplification factor
λ_s	Lame's first parameter
λ_H	wavelength
μ_f	fluid viscosity
μ_i	ith eigenvalue of discrete representation of the added mass op-

	erator
μ_s	Lame's second parameter
ν_s	Poisson ratio
ξ	free parameter of an explicit two-step method
ξ_T	local length of the cable at rest
ρ	density ratio of solid to fluid, $\rho = \rho_s/\rho_f$
ρ_f	fluid density
ρ_s	solid density
ρ_s^0	initial density of an elastic body
ρ_{min}	lowest density ratio
$\hat{\sigma}_{mn}$	second Piola-Kirchhoff stress tensor
χ	user-specified value in the generalized-α method
ψ_q^y	spatial phase angle associated with the qth mode
$\omega^{n,k}$	under-relaxation factor at kth iteration for the current time step
ω_b	bending coefficient
ω_c	tension coefficient
Ω_e	element

Chapter 1

Introduction

When fluid flows around a bluff body with sufficiently high velocity, vortices are shed alternatively from upper and lower sides of a bluff body. This phenomenon is known as vortex shedding. Vortex shedding induces high mean drag and lift fluctuations on a bluff body because pressure is low at the core of vortex. In addition, if a structure is not stationary, the vibration of the structure is induced by the interaction between vortex shedding and the motion of the structure. The matching of the frequency of vortex shedding with the vibration frequency of a structure is defined as lock-in (Khalak & Williamson, 1999). In the lock-in condition, the amplitude of structural vibration in the transverse direction is very large, and thus vortex-induced vibration can cause severe fatigue damage on structures such as extremely long risers or destruction of structures such as the Tacoma Narrows Bridge.

Extremely long risers have received much attention in recent years due to the large demand of crude oil in the world and expansion of the exploration area to deeper water regions (Wu *et al.*, 2012). However, extremely long risers could suffer from severe fatigue damage induced by vortex-induced vibration due to a current in the ocean, so field experiments were conducted to measure strain response of a flexible circular cylinder (Vandiver *et al.*, 2009). In laboratory experiments, vortex-induced vibration with amplitude greater than $1D$ in the transverse direction was observed for a long flexible circular cylinder (Chaplin

et al., 2005; Trim *et al.*, 2005; Huera-Huarte *et al.*, 2014; Song *et al.*, 2011; Gao *et al.*, 2017; Gedikli & Dahl, 2017), where D is the diameter of a circular cylinder. However, the cause of vortex-induced vibration with very large amplitude is not completely explained. Therefore, it is required to explain the cause of vortex-induced vibration with very large amplitude and suppress it.

On the other hand, the collapse of the Tacoma Narrows Bridge is one of the famous cases of fluid-structure interaction. Before the collapse of the Tacoma Narrows Bridge due to large torsional motion, the wind blew across the Tacoma Narrows Bridge with the wind speed of 42 mph, and the frequency of the torsional motion of the Tacoma Narrows Bridge was 0.2 Hz (Farquharson, 1949). Von Karman was convinced that the culprit in the Tacoma disaster was the Karman Vortex Street (von Karman & Edson, 1967). However, at 42 mph, the frequency of natural vortex shedding according to the Strouhal relation would be close to 1 Hz, wholly out of synch with the actual catastrophic oscillation then going on (Billah & Scanlan, 1991). Until now, many researchers have tried to explain the collapse of the Tacoma Narrows Bridge through various ways such as flutter of aircraft wings (Bleich, 1948), a combination of parametric resonance (Pittel & Yakubovich, 1961, 1969; Yakubovich & Starzhinskii, 1975), negative damping (Green & Unruh, 2006), and an aerodynamically induced condition of self-excitation in a torsional degree of freedom (Billah & Scanlan, 1991). However, there are still controversial discussions about what caused the sudden change to torsional motion (Mckenna, 1999) and what is the exact cause of the collapse of the Tacoma Narrows Bridge (Scott, 2001).

This thesis is organized as follows. In Chapter 2, a new weak coupling for low mass ratio is introduced and applied to fuid-structure interaction problems with mass ratio less than 1. In Chapter 3, the cause of large amplitude vibration of an elastically mounted rigid circular cylinder in a uniform flow is revealed, and then

a parametric study is performed to find the optimal shape of the helically twisted elliptic cylinder (HTE) to suppress large amplitude vortex-induced vibration. Based on the results of flow around an elastically mounted rigid cylinder, the cause of large amplitude vibration of a flexible circular cylinder in a strongly sheared flow is presented and large amplitude vibration is suppressed by the HTE cylinder. In Chapter 4, the cause of the collapse of the Tacoma Narrows Bridge is discussed.

Chapter 2

A weak-coupling immersed boundary method for fluid-structure interaction with low density ratio of solid to fluid

2.1 Motivations and objectives

Fluid-structure interactions occur in various fields such as mechanical, aerospace, and biomedical engineering. So far, many numerical methods for fluid-structure interaction have been developed and they may be classified into monolithic and partitioned approaches, respectively (Hou *et al.*, 2012). The monolithic approach simultaneously solves the governing equations for fluid and structure by combining them into a single system, whereas the partitioned one uses separate solvers for fluid and structure, respectively. Thus, the latter approach facilitates taking advantage of a suitable solution algorithm for each governing equation of fluid and structure motions (Felippa *et al.*, 2001).

In fluid-structure interaction problems, the no-slip boundary condition should be satisfied on the fluid-structure interface when the equations for fluid flow are solved, and the hydrodynamic forces on the interface should be provided when the structure equation is solved. For this purpose, it is necessary to transfer variables such as the velocity, velocity gradient, and pressure on the interface from fluid to structure, or vice versa, through strong or weak coupling. Strong

coupling implicitly transfers variables on the interface and simultaneously (or iteratively until convergence) solves the governing equations for fluid and structure at each time step. Strong coupling guarantees the temporal accuracy of fluid and structure time integrators (Felippa *et al.*, 2001), but usually requires an iterative process which increases the computational cost per time step (Weeratunga & Pramono, 1994). Also, strong coupling may lead to unstable solutions for the problems with low density ratio (ρ) of solid to fluid (Borazjani *et al.*, 2008). To obtain stable solutions for those problems, block-Gauss-Seidel methods with an under-relaxation scheme (Borazjani *et al.*, 2008; Le Tallec & Mouro, 2001; Deparis *et al.*, 2003; Kuttler & Wall, 2008; Kassiotis *et al.*, 2011; Breuer *et al.*, 2012; Tian *et al.*, 2014; Gilmanov *et al.*, 2015) and block-Newton methods (Tezduyar, 2001; Gerbeau & Vidrascu, 2003; Matthies & Steindorf, 2003; Fernandez & Moubachir, 2005) have been applied together with strong coupling. On the other hand, weak coupling is performed in a staggered manner where the governing equations for fluid and structure are alternatively solved at each time step without iteration. Weak coupling is easier to implement and requires less computational cost per time step than strong coupling. However, weak coupling degrades the temporal accuracy at least one order lower than those of fluid and structure time integrators, and even severely restricts the stability limit for low-density-ratio problems (Piperno & Farhat, 2001).

In weak coupling, a predictor is used as a tool to prevent the degradation of temporal accuracy. Piperno *et al.* (1995) suggested implicit schemes for fluid and structure (called implicit/implicit scheme), respectively, with the position and velocity of the interface determined from the previous time step, and thus their temporal accuracy was first order. An implicit/implicit (Farhat *et al.*, 2006), explicit/explicit, and implicit/explicit schemes (Farhat *et al.*, 2010) are proposed for compressible fluid-structure interaction problems, together with

predictor and corrector schemes for the interface position and hydrodynamic force, thus satisfying a second-order accuracy. Farhat *et al.* (2010) also showed that the order of temporal accuracy depends on predictor and corrector schemes. Dettmer & Peric (2013) suggested a predictor using a second-order linear extrapolation and a corrector using a weighted average on the hydrodynamic force for incompressible fluid-structure interaction problems, and obtained a second-order accuracy. However, their method was unstable for a problem with $\rho = 1$. Yang *et al.* (2008) showed that weak coupling using a semi-implicit/explicit scheme (without a predictor) produces unstable solutions for the interaction of incompressible flow and a rigid body with $\rho = 1.07$, whereas strong coupling using Hammings fourth-order predictor-corrector method provides stable solutions but does not much increase the number of iterations even if the number of degrees of freedom of the structure increases.

For fluid-structure interaction problems with $\rho < 1$, the numerical stability of weak coupling is restricted by the added-mass effect (Causin *et al.*, 2005; Foster *et al.*, 2007; van Brummelen, 2009). The added mass of incompressible flow approaches a constant as the size of computational time step decreases, because the displacement of the interface affects the entire flow field (van Brummelen, 2009). Thus, weak coupling for incompressible flow with low ρ shows unstable solutions even for a sufficiently small size of computational time step. On the other hand, the added mass of compressible flow is proportional to the size of computational time step because the displacement of the interface affects local flow field only (van Brummelen, 2009). Foster *et al.* (2007) derived an instability condition of weak coupling with a predictor, and compared the lowest possible ρ's for different predictors. However, the velocity predictor suggested by Foster *et al.* (2007) had a first-order temporal accuracy. Therefore, it should be useful to find a predictor providing a second-order temporal accuracy for

fluid-structure problems with low ρ's.

To handle an arbitrarily moving interface, Peskin (1972) suggested an immersed boundary (called IB hereafter) method. This method is convenient and efficient, because it allows the use of a non-body-fitted or structured mesh such as the Cartesian or cylindrical mesh and does not require mesh regeneration for a moving interface problem. This IB method is called continuous forcing (Mittal & Iaccarino, 2005) in that momentum forcing is provided along the IB, and has been developed by many investigators (Peskin, 1972; Beyer & LeVeque, 1992; Saiki & Biringen, 1996; Lai & Peskin, 2000; Goldstein *et al.*, 1993; Huang & Sung, 2009). Another IB method is called discrete forcing in which forcing is applied at the grid points (or cell surfaces) (Fadlun *et al.*, 2000; Kim *et al.*, 2001). The discrete-forcing IB method sharply expresses IB and allows a high Courant-Friedrichs-Lewy (CFL) number (Fadlun *et al.*, 2000; Kim *et al.*, 2001; Lee & You, 2013). Thus, this method has been also widely used to simulate flow around an elastic body (Tian *et al.*, 2014; Luo *et al.*, 2008; Lee & Choi, 2015) as well as a rigid body (Yang *et al.*, 2008; Lee & You, 2013; Yang & Balaras, 2006; Lee *et al.*, 2011). Here, we use a discrete-forcing IB method to satisfy the no-slip condition at the fluid-structure interface (Kim *et al.*, 2001).

In the present study, we develop a weak coupling method with predictors for fluid-structure interface position and velocity, together with a discrete-forcing IB method. To preserve a second-order temporal accuracy, an explicit two-step method as a predictor is used to obtain a provisional velocity distribution on the fluid-structure interface, and then the implicit Euler method is applied to predict its position from the provisional velocity obtained. We consider both rigid and elastic bodies with $\rho < 1$: flows around an elastically mounted rigid circular cylinder, an elastic beam attached to the base of a stationary circular cylinder, and a flexible plate. The results are compared with those by strong

coupling suggested in this study and by previous numerical and experimental studies. We provide a numerical method in Sec. 2.2, and apply it to three different fluid-structure problems in Sec. 2.3, followed by summary in Sec. 2.4.

2.2 Numerical method

The governing equations for incompressible flow are solved in an Eulerian coordinate, whereas the dynamic equation for the motion of a rigid or elastic body is solved in a Lagrangian coordinate. To satisfy the no-slip condition and exert the hydrodynamic force on the interface, flow and structure variables such as the displacement, velocity, velocity gradient and pressure are transferred from the Eulerian to Lagrangian coordinates, and vice versa.

2.2.1 Weak coupling vs. strong coupling

The procedures of weak coupling with predictors and strong coupling using an iterative scheme are introduced in figures 2.1(a) and (b), respectively. Weak coupling with predictors consists of three steps (figure 2.1(a)): 1) obtaining provisional displacement and velocity on the fluid-structure interface from the information at the previous time step $(n-1)$; 2) updating the velocity and pressure of fluid at the current time step (n) with the provisional displacement and velocity; 3) updating the displacement, velocity and acceleration of structure with the hydrodynamic force obtained at the current time step (n). On the other hand, strong coupling (figure 2.1(b)) iteratively solves the governing equations of fluid and structure motions, respectively, with the interface position (and velocity) and the hydrodynamic force obtained at the previous iteration until $\|\dot{\boldsymbol{d}}^{n,k} - \dot{\boldsymbol{d}}^{n,k-1}\|_\infty < \epsilon$ (figure 2.1(b)), where $\dot{\boldsymbol{d}}$ and ϵ are the structural velocity and tolerance level, respectively. During iteration, an under-relaxation

is applied to the displacement, velocity and acceleration of structure, together with the Aitken method (Kuttler & Wall, 2008; Irons & Tuck, 1969) to determine an optimal under-relaxation factor for fast convergence. Computational time for weak coupling is much less than that for strong coupling, and accurate and stable solutions for the problems with low ρ's can be obtained by weak coupling when predictors are well designed. Nevertheless, the lowest possible ρ's for strong coupling are still lower than those for weak coupling (see below and also Borazjani *et al.* (2008), Dettmer & Peric (2013), and Yang *et al.* (2008)).

2.2.2 Numerical method for fluid flow

The governing equations for unsteady incompressible flow are the Navier-Stokes and continuity equations. Their non-dimensional forms using a discrete-forcing IB method (Kim *et al.*, 2001) are

$$\frac{\partial u_i}{\partial t} + \frac{\partial u_i u_j}{\partial x_j} = -\frac{\partial p}{\partial x_i} + \frac{1}{\mathrm{Re}} \frac{\partial^2 u_i}{\partial x_j \partial x_j} + f_i, \tag{2.1}$$

$$\frac{\partial u_i}{\partial x_i} - q = 0, \tag{2.2}$$

where $x_i = (x, y, z)$ is the Cartesian coordinates (streamwise, transverse, and spanwise directions, respectively), $u_i = (u, v, w)$ is the corresponding velocity, p is the pressure, f_i is the momentum forcing, and q is the mass source/sink. All variables are non-dimensionalized by the characteristic velocity (U), length (L) and fluid density (ρ_f). The Reynolds number is $\mathrm{Re} = \rho_f U L / \mu_f$, where μ_f is the fluid viscosity.

For time advancement, an implicit fractional step method (Choi & Moin, 1994) with linearization (Kim *et al.*, 2002) is used:

$$\frac{\hat{u}_i^n - u_i^{n-1}}{\Delta t} = \frac{1}{2\,\mathrm{Re}}\frac{\partial^2}{\partial x_j \partial x_j}(\hat{u}_i^n + u_i^{n-1}) - \frac{\partial p^{n-1}}{\partial x_i} - \frac{1}{2}\frac{\partial}{\partial x_j}(\hat{u}_j^n u_i^{n-1} + u_j^{n-1}\hat{u}_i^n) + f_i^n, \tag{2.3}$$

$$\frac{\partial^2 \delta p}{\partial x_j \partial x_j} = \frac{1}{\Delta t}\left(\frac{\partial \hat{u}_j^n}{\partial x_j} - q^n\right), \tag{2.4}$$

$$u_i^n = \hat{u}_i^n - \Delta t \frac{\partial \delta p}{\partial x_i}, \tag{2.5}$$

$$p^n = p^{n-1} + \delta p, \tag{2.6}$$

where $\hat{u}_i^n$ is the intermediate velocity and Δt is the computational time step. For spatial discretization, the second-order central difference is used for all spatial derivative terms. The velocity and pressure are defined on the cell faces and centers, respectively, on a staggered mesh. The momentum forcing f_i^n is applied at the grid cell faces on or inside the IB to satisfy the no-slip condition, and the mass source/sink q^n is applied at the grid centers for the cells containing and inside the IB to satisfy local and global mass conservation (figure 2.2). The momentum forcing f_i^n in equation (2.3) is determined in advance to satisfy the no-slip condition of $\hat{u}_i^n$ instead of u_i^n, which still preserves a second-order temporal accuracy because $u_i^n = \hat{u}_i^n - \Delta t \partial \delta p / \partial x_i = \hat{u}_i^n + O(\Delta t^2)$. See (Kim *et al.*, 2001) for the details of determining the momentum forcing and mass source/sink. In moving-body problems, the locations of momentum forcing and mass source/sink are updated every time step, as given in (Lee & Choi, 2015).

2.2.3 Numerical method for the motions of rigid and elastic bodies

The motion of a rigid body in a mass-damper-spring system is given as

$$\ddot{\boldsymbol{d}} + 2\zeta\left(\frac{2\pi}{U^*}\right)\dot{\boldsymbol{d}} + \left(\frac{2\pi}{U^*}\right)^2 \boldsymbol{d} = \frac{L^3}{\rho V_s}\boldsymbol{F_H} + \boldsymbol{g}, \tag{2.7}$$

where $\ddot{\boldsymbol{d}}$, $\dot{\boldsymbol{d}}$, and $\boldsymbol{d}$ are the acceleration, velocity and displacement vectors, respectively, $\zeta\left(= c_s/2\sqrt{k_s m_s}\right)$ is the damping ratio, c_s is the damping coefficient, k_s is the spring constant, m_s is the solid mass, $U^*\,(= U/f_N L)$ is the reduced velocity, $f_N\left(= (1/2\pi)\sqrt{k_s/m_m}\right)$ is the natural vibration frequency, $\rho\,(= \rho_s/\rho_f)$ is the solid-to-fluid density ratio, ρ_s is the solid density, V_s is the solid volume, $\boldsymbol{F_H}\left(= \int_\Gamma \left[-pn_i + n_j\left(\partial u_i/\partial x_j + \partial u_j/\partial x_i\right)/\,\mathrm{Re}\right] dS\right)$ is the hydrodynamic force vector, Γ is the fluid-structure interface, n_i is the surface-normal vector, and $\boldsymbol{g}$ is the gravitational acceleration vector.

A finite element formulation derived from the standard virtual work method is used to solve the motion of an elastic body:

$$\boldsymbol{M}\ddot{\boldsymbol{d}} + \boldsymbol{R}(\boldsymbol{d}) = \boldsymbol{F_H} + \boldsymbol{G}, \tag{2.8}$$

where $\boldsymbol{M}$ is the mass matrix, $\boldsymbol{R}(\boldsymbol{d})$ is the internal force vector, $\boldsymbol{F_H}$ is the hydrodynamic force vector, and $\boldsymbol{G}$ is the gravitational force vector. Employing a lumped mass matrix (Hinton *et al.*, 1976) and a total Lagrangian approach provides

$$\boldsymbol{M} = M_{iIjJ} = \frac{1}{\rho_f L^3}\varrho_e M_{II}\delta_{ij}\delta_{IJ} \text{ (no summation for } I), \tag{2.9}$$

$$\boldsymbol{R}(\boldsymbol{d}) = R_{iI} = \frac{1}{\rho_f U^2 L^2}\int_{V^0}\left(F_{im}\hat{\sigma}_{mn}\frac{\partial N_I}{\partial X_n^0}\right) dV, \tag{2.10}$$

$$\boldsymbol{F_H} = (F_H)_{iI} = \int_\Gamma \left[-pn_i + \frac{1}{\mathrm{Re}} \left(\frac{\partial u_i}{\partial x_j} + \frac{\partial u_j}{\partial x_i} \right) n_j \right] N_I dS, \tag{2.11}$$

$$\boldsymbol{G} = G_{iI} = M_{iIjJ} g_{jJ}, \tag{2.12}$$

where $\varrho_e = M_e / \sum_{I=1}^{n_e} M_{II}$, $M_e = \int_{\Omega_e} \rho_s^0 d\Omega$, Ω_e is an element, ρ_s^0 is the initial density of an elastic body, I and J are the indices of nodes within an element, n_e is the number of nodes per element, $M_{II} = \int_{\Omega_e} \rho_s^0 N_I N_I d\Omega$ (no summation for I), N_I is the shape function, δ_{ij} is the Kronecker delta, V^0 is the initial volume of an elastic body, $F_{im} = \partial X_i / \partial X_m^0$, X_i is the current position vector, X_m^0 is the initial position vector, $\hat{\sigma}_{mn}$ is the second Piola-Kirchhoff stress tensor, and g_{jJ} is the gravitational acceleration vector. In the present study, an elastic body is considered as a hyper-elastic material, and then the second Piola-Kirchhoff stress tensor is expressed as $\hat{\sigma}_{mn} = \partial W / \partial E_{mn}$, where W is the strain energy density function and $E_{mn} = 0.5 \left(F_{im} F_{in} - \delta_{mn} \right)$. The strain energy density function of the Saint Venant-Kirchhoff model is expressed as

$$W = \frac{\lambda_s}{2} \left[\mathrm{tr} \left(E_{ij} \right) \right]^2 + \mu_s \, \mathrm{tr} \left(E_{ik} E_{kj} \right), \tag{2.13}$$

where $\lambda_s = E_s \nu_s / \left[(1 + \nu_s) (1 - 2\nu_s) \right]$, $\mu_s = E_s / 2 (1 + \nu_s)$, E_s is the Young's modulus, and ν_s is the Poisson ratio.

Nine-node quadrilateral and twenty-node hexahedral elements are employed for two-dimensional and three-dimensional problems, respectively. The Gauss quadrature is used for the surface and volume integrations. A second-order implicit generalized-α method (Chung & Hulbert, 1993) is used for the time advancements of equations (2.7) and (2.8), respectively:

$$(1-\alpha_m)\ddot{\boldsymbol{d}}^n + \alpha_m \ddot{\boldsymbol{d}}^{n-1} + 2\zeta\left(\frac{2\pi}{U^*}\right)\left[(1-\alpha_f)\,\dot{\boldsymbol{d}}^n + \alpha_f \dot{\boldsymbol{d}}^{n-1}\right] + \left(\frac{2\pi}{U^*}\right)^2\left[(1-\alpha_f)\,\boldsymbol{d}^n + \alpha_f \boldsymbol{d}^{n-1}\right]$$
$$= \frac{L^3}{\rho V_s}\left[(1-\alpha_f)\,\boldsymbol{F}_{\boldsymbol{H}}^n + \alpha_f \boldsymbol{F}_{\boldsymbol{H}}^{n-1}\right] + (1-\alpha_f)\,\boldsymbol{g}^n + \alpha_f \boldsymbol{g}^{n-1}, \tag{2.14}$$

$$\boldsymbol{M}\left[(1-\alpha_m)\,\ddot{\boldsymbol{d}}^n + \alpha_m \ddot{\boldsymbol{d}}^{n-1}\right] + (1-\alpha_f)\,\boldsymbol{R}\left(\boldsymbol{d}\right)^n + \alpha_f \boldsymbol{R}\left(\boldsymbol{d}\right)^{n-1}$$
$$= (1-\alpha_f)\left(\boldsymbol{F}_{\boldsymbol{H}}^n + \boldsymbol{G}^n\right) + \alpha_f\left(\boldsymbol{F}_{\boldsymbol{H}}^{n-1} + \boldsymbol{G}^{n-1}\right), \tag{2.15}$$

$$\boldsymbol{d}^n = \boldsymbol{d}^{n-1} + \Delta t \dot{\boldsymbol{d}}^{n-1} + \Delta t^2\left[(0.5-\beta)\,\ddot{\boldsymbol{d}}^{n-1} + \beta \ddot{\boldsymbol{d}}^n\right], \tag{2.16}$$

$$\dot{\boldsymbol{d}}^n = \dot{\boldsymbol{d}}^{n-1} + \Delta t\left[(1-\gamma)\,\ddot{\boldsymbol{d}}^{n-1} + \gamma \ddot{\boldsymbol{d}}^n\right], \tag{2.17}$$

where $\alpha_m = (2\chi-1)/(\chi+1)$, $\alpha_f = \chi/(\chi+1)$, $\beta = 0.25\,(1-\alpha_m+\alpha_f)^2$, $\gamma = 0.5-\alpha_m+\alpha_f$, and $\chi \in [0,1]$ is the user-specified value. Here, a high-frequency solid-body motion is more dissipated as χ decreases from 1 to 0 (Chung & Hulbert, 1993). The Broyden-Fletcher-Goldfarb-Shanno (BFGS) method (Matthies & Strang, 1979) is applied to solve equations (2.15)–(2.17).

2.2.4 Predictors for the motion of fluid-solid interface and their numerical stability

As described in Sec. 2.2.1, weak coupling requires predictors for the position and velocity of fluid-structure interface to obtain accurate and stable solutions.

As predictors, we consider an explicit two-step method and the implicit Euler method to obtain provisional velocity and displacement of fluid-structure interface ($\tilde{\dot{\boldsymbol{d}}}^n$ and $\tilde{\boldsymbol{d}}^n$), respectively:

$$\tilde{\dot{\boldsymbol{d}}}^n = \dot{\boldsymbol{d}}^{n-1} + \Delta t \left[\xi \ddot{\boldsymbol{d}}^{n-1} + (1-\xi)\, \ddot{\boldsymbol{d}}^{n-2} \right], \tag{2.18}$$

$$\tilde{\boldsymbol{d}}^n = \boldsymbol{d}^{n-1} + \Delta t \tilde{\dot{\boldsymbol{d}}}^n, \tag{2.19}$$

where ξ is a free parameter, and $\ddot{\boldsymbol{d}}^{n-1}$ and $\ddot{\boldsymbol{d}}^{n-2}$ are the acceleration vectors obtained at two previous time steps. The computational cost to solve equations (2.18) and (2.19) is very low because of explicit treatment. These predictors are used only to obtain the provisional velocity and displacement of fluid-structure interface at each time step, and thus do not degrade the second-order temporal accuracy of fluid and structure solvers (see Sec. 2.3.1).

The stability condition for from weak coupling with a predictor is written as (Foster *et al.*, 2007)

$$\rho \geq C_s \max_i \mu_i, \tag{2.20}$$

where C_s is the stability constant, μ_i is the ith eigenvalue of $\boldsymbol{M_A}$, $\boldsymbol{M_A}$ ($= \boldsymbol{H_\Gamma} \left(\boldsymbol{D_I} \boldsymbol{G_I} \right)^{-1} \boldsymbol{D_\Gamma}$) is the discrete representation of the added mass operator, $\boldsymbol{H_\Gamma}$ is the discrete operator representing the hydrodynamic force from pressure on the fluid-structure interface, $\boldsymbol{D_I}$ and $\boldsymbol{D_\Gamma}$ are the discrete divergence operators for the interior and interface fluid velocities, respectively, and $\boldsymbol{G_I}$ is the discrete gradient operator for interior pressure. A linear stability analysis is conducted neglecting the convection and viscous terms in equation (2.1) and the internal force in equation (2.8) (see Foster *et al.* (2007) for the details). A predictor

in weak coupling does not change μ_i (and $\boldsymbol{M_A}$) but determines C_s in equation (2.20). As in equation (2.20), the lowest ρ for stable solution becomes smaller with smaller C_s. This C_s depends on the choice of the velocity predictor.

The stability condition of weak coupling using the present explicit two-step method (equation (2.18)) is derived following the procedure in (Foster *et al.*, 2007). Equations (2.15)–(2.17) with $\chi = 0$ give

$$\boldsymbol{M}\left(2\ddot{\boldsymbol{d}}^n - \ddot{\boldsymbol{d}}^{n-1}\right) + \boldsymbol{R}\boldsymbol{d}^n = \boldsymbol{F}_{\boldsymbol{H}}^n, \tag{2.21}$$

$$\dot{\boldsymbol{d}}^n = \frac{1}{\Delta t}\left(\frac{3}{2}\boldsymbol{d}^n - 2\boldsymbol{d}^{n-1} + \frac{1}{2}\boldsymbol{d}^{n-2}\right), \tag{2.22}$$

$$\ddot{\boldsymbol{d}}^n = \frac{1}{\Delta t^n}\left(\boldsymbol{d}^n - 2\boldsymbol{d}^{n-1} + \boldsymbol{d}^{n-2}\right). \tag{2.23}$$

For very small time step, the internal force is negligible because it is much smaller than the inertia and hydrodynamic forces: i.e., $\boldsymbol{M} = \rho\boldsymbol{I}$ and $\boldsymbol{R} = 0$. Then, equation (2.21) with equation (2.23) is reduced to the following equation regarding the interfacial degrees of freedom:

$$\rho\frac{1}{\Delta t^2}\left(2\boldsymbol{d}_{\boldsymbol{\Gamma}}^n - 5\boldsymbol{d}_{\boldsymbol{\Gamma}}^{n-1} + 4\boldsymbol{d}_{\boldsymbol{\Gamma}}^{n-2} - \boldsymbol{d}_{\boldsymbol{\Gamma}}^{n-3}\right) = \boldsymbol{F}_{\boldsymbol{H}}^n, \tag{2.24}$$

where Γ denotes the fluid-structure interface. The convection and viscous terms in a fluid solver are also negligible compared with the time derivative of the velocity and pressure terms for very small time step, and then the hydrodynamic force can be expressed as

$$\boldsymbol{F}_{\boldsymbol{H}} = -\boldsymbol{M}_{\boldsymbol{A}}\dot{\boldsymbol{u}}_{\boldsymbol{\Gamma}}, \tag{2.25}$$

where $\dot{\boldsymbol{u}}_{\boldsymbol{\Gamma}}$ is the fluid acceleration vector on the interface. The implicit Euler method is applied to equation (2.25), and the fluid velocity on the interface is given to be the provisional interface velocity of an elastic body:

$$\boldsymbol{F}_{\boldsymbol{H}}^{n} = -\boldsymbol{M}_{\boldsymbol{A}} \frac{\boldsymbol{u}_{\boldsymbol{\Gamma}}^{n} - \boldsymbol{u}_{\boldsymbol{\Gamma}}^{n-1}}{\Delta t}, \tag{2.26}$$

$$\boldsymbol{u}_{\boldsymbol{\Gamma}}^{n} = \tilde{\dot{\boldsymbol{d}}}_{\boldsymbol{\Gamma}}^{n}. \tag{2.27}$$

The provisional velocity on the fluid-structure interface is obtained from equation (2.18) using the explicit two-step method:

$$\begin{aligned}
\tilde{\dot{\boldsymbol{d}}}_{\boldsymbol{\Gamma}}^{n} &= \dot{\boldsymbol{d}}_{\boldsymbol{\Gamma}}^{n-1} + \Delta t \left[\xi \ddot{\boldsymbol{d}}_{\boldsymbol{\Gamma}}^{n-1} + (1-\xi)\, \ddot{\boldsymbol{d}}_{\boldsymbol{\Gamma}}^{n-2} \right] \\
&= \frac{1}{\Delta t} \left(\frac{3}{2} \boldsymbol{d}_{\boldsymbol{\Gamma}}^{n-1} - 2\boldsymbol{d}_{\boldsymbol{\Gamma}}^{n-2} + \frac{1}{2} \boldsymbol{d}_{\boldsymbol{\Gamma}}^{n-3} \right) + \\
&\frac{1}{\Delta t} \left[\xi \left(\boldsymbol{d}_{\boldsymbol{\Gamma}}^{n-1} - 2\boldsymbol{d}_{\boldsymbol{\Gamma}}^{n-2} + \boldsymbol{d}_{\boldsymbol{\Gamma}}^{n-3} \right) + (1-\xi) \left(\boldsymbol{d}_{\boldsymbol{\Gamma}}^{n-2} - 2\boldsymbol{d}_{\boldsymbol{\Gamma}}^{n-3} + \boldsymbol{d}_{\boldsymbol{\Gamma}}^{n-4} \right) \right] \\
= \frac{1}{\Delta t} &\left[\left(\frac{3}{2} + \xi \right) \boldsymbol{d}_{\boldsymbol{\Gamma}}^{n-1} + (-1-3\xi)\, \boldsymbol{d}_{\boldsymbol{\Gamma}}^{n-2} + \left(-\frac{3}{2} + 3\xi \right) \boldsymbol{d}_{\boldsymbol{\Gamma}}^{n-3} + (1-\xi)\, \boldsymbol{d}_{\boldsymbol{\Gamma}}^{n-4} \right].
\end{aligned} \tag{2.28}$$

Combining equations (2.24), (2.26)–(2.28) provides

$$\begin{aligned}
&\rho \left(2\boldsymbol{d}_{\boldsymbol{\Gamma}}^{n} - 5\boldsymbol{d}_{\boldsymbol{\Gamma}}^{n-1} + 4\boldsymbol{d}_{\boldsymbol{\Gamma}}^{n-2} - \boldsymbol{d}_{\boldsymbol{\Gamma}}^{n-3} \right) + \\
&\boldsymbol{M}_{\boldsymbol{A}} \left[\left(\frac{3}{2} + \xi \right) \boldsymbol{d}_{\boldsymbol{\Gamma}}^{n-1} + \left(-\frac{5}{2} - 4\xi \right) \boldsymbol{d}_{\boldsymbol{\Gamma}}^{n-2} + \left(-\frac{1}{2} + 6\xi \right) \boldsymbol{d}_{\boldsymbol{\Gamma}}^{n-3} \right] + \\
&\boldsymbol{M}_{\boldsymbol{A}} \left[\left(\frac{5}{2} - 4\xi \right) \boldsymbol{d}_{\boldsymbol{\Gamma}}^{n-4} + (-1+\xi)\, \boldsymbol{d}_{\boldsymbol{\Gamma}}^{n-5} \right] = 0.
\end{aligned} \tag{2.29}$$

The displacement vector is expressed with the eigenvectors $\boldsymbol{v_i}$ of $\boldsymbol{M_A}$, $\boldsymbol{d}_{\boldsymbol{\Gamma}}^{n} =$

$\sum_i \bar{d}_i^n \boldsymbol{v}_i$, where $\bar{d}_i$ is the scalar coefficient, and i is the number of nodes on the interface. Then, equation (2.29) becomes

$$\begin{aligned} \rho\left(2\bar{d}_i^n - 5\bar{d}_i^{n-1} + 4\bar{d}_i^{n-2} - \bar{d}_i^{n-3}\right) + \\ \mu_i\left[\left(\frac{3}{2}+\xi\right)\bar{d}_i^{n-1} + \left(-\frac{5}{2}-4\xi\right)\bar{d}_i^{n-2} + \left(-\frac{1}{2}+6\xi\right)\bar{d}_i^{n-3}\right] + \\ \mu_i\left[\left(\frac{5}{2}-4\xi\right)\bar{d}_i^{n-4} + (-1+\xi)\,\bar{d}_i^{n-5}\right] = 0. \end{aligned} \tag{2.30}$$

The characteristic polynomial of equation (2.30) is obtained using the amplification factor λ_i with $\bar{d}_i^n = \lambda_i \bar{d}_i^{n-1}$:

$$(\lambda_i - 1)^2\left[\rho\lambda_i^2(2\lambda_i - 1) + \mu_i\left(\left(\frac{3}{2}+\xi\right)\lambda_i^2 + \left(\frac{1}{2}-2\xi\right)\lambda_i + (-1+\xi)\right)\right] = 0. \tag{2.31}$$

Since two solutions of equation (2.31) are $\lambda_i = 1$, equation (2.31) reduces to (for the purpose of stability analysis)

$$\rho\lambda_i^2(2\lambda_i - 1) + \mu_i\left[\left(\frac{3}{2}+\xi\right)\lambda_i^2 + \left(\frac{1}{2}-2\xi\right)\lambda_i + (-1+\xi)\right] = 0. \tag{2.32}$$

Equation (2.32) is stable if $|\lambda_i| \leq 1$ for all three λ_i's. The Bistritz stability criterion (Bistritz, 1984) is applied to equation (2.32) for obtaining $|\lambda_i| \leq 1$, providing the following four conditions:

$$2(\rho + \mu_i) \geq 0, \tag{2.33}$$

$$5\rho + 4\mu_i \geq 0, \tag{2.34}$$

$$\frac{2\left[8\rho^2 + 6\xi\mu_i\rho + 5\left(\xi - 1\right)\mu_i^2\right]}{2\rho + \mu_i - \xi\mu_i} \geq 0, \tag{2.35}$$

$$3\rho - 4\xi\mu_i \geq 0. \tag{2.36}$$

The first two conditions (equations (2.33) and (2.34)) are always satisfied because $\rho \geq 0$ and $\mu_i \geq 0$. To satisfy the third condition (equation (2.35)), both the denominator and nominator should be either positive or negative: the latter case does not exist for positive ρ, and the first case provides $\rho \geq \frac{1}{8}\left(-3\xi + \sqrt{9\xi^2 - 40\xi + 40}\right)\mu_i$ for $\xi \leq 1$ and $\rho > \frac{1}{2}\left(\xi - 1\right)\mu_i$ for $\xi > 1$. For the last condition (equation (2.36)), $\rho \geq \frac{4}{3}\xi\mu_i$. Comparing the magnitudes of these ρ's, the stability condition for equation (2.32) becomes $\left(\rho \geq C_s \max_i \mu_i\right)$

$$\rho \geq \begin{cases} \frac{-3\xi + \sqrt{9\xi^2 - 40\xi + 40}}{8} \max_i \mu_i & \text{for } \xi \leq \frac{3}{8} \\ \frac{4\xi}{3} \max_i \mu_i & \text{for } \xi > \frac{3}{8}. \end{cases} \tag{2.37}$$

This stability limit of ρ is drawn in figure 2.3. As shown, the lowest density ratio is obtained at $\xi = 3/8\,(\chi = 0)$. Note that equation (2.37) is obtained assuming that the convection and viscous terms in equation (2.1) and the internal force in equation (2.8) are negligible.

2.2.5 Strong coupling algorithm

Strong coupling is based on the iterative process as shown in figure 2.1(b). The procedures of strong coupling for equations (2.3)-(2.6) and (2.14)-(2.17) are

$$\frac{\hat{u}_i^{n,k} - u_i^{n-1}}{\Delta t} = \frac{1}{2\,\mathrm{Re}} \frac{\partial^2}{\partial x_j \partial x_j} \left(\hat{u}_i^{n,k} + u_i^{n-1} \right) - \frac{\partial p^{n-1}}{\partial x_i} - \frac{1}{2} \frac{\partial}{\partial x_j} \left(\hat{u}_j^{n,k} u_i^{n-1} + u_j^{n-1} \hat{u}_i^{n,k} \right) + f_i^{n,k}, \tag{2.38}$$

$$\frac{\partial^2 \delta p^{n,k}}{\partial x_j \partial x_j} = \frac{1}{\Delta t} \left(\frac{\partial \hat{u}_j^{n,k}}{\partial x_j} - q^{n,k} \right), \tag{2.39}$$

$$u_i^{n,k} = \hat{u}_i^{n,k} - \Delta t \frac{\partial \delta p^{n,k}}{\partial x_i}, \tag{2.40}$$

$$p^{n,k} = p^{n-1} + \delta p^{n,k}, \tag{2.41}$$

and

$$(1-\alpha_m)\,\hat{\ddot{\boldsymbol{d}}}^{n,k} + \alpha_m \ddot{\boldsymbol{d}}^{n-1} + 2\zeta \left(\frac{2\pi}{U^*} \right) \left[(1-\alpha_f)\,\hat{\dot{\boldsymbol{d}}}^{n,k} + \alpha_f \dot{\boldsymbol{d}}^{n-1} \right] + \left(\frac{2\pi}{U^*} \right)^2 \left[(1-\alpha_f)\,\hat{\boldsymbol{d}}^{n,k} + \alpha_f \boldsymbol{d}^{n-1} \right] = \frac{L^3}{\rho V_s} \left[(1-\alpha_f)\,\boldsymbol{F}_{\boldsymbol{H}}^{n,k} + \alpha_f \boldsymbol{F}_{\boldsymbol{H}}^{n-1} \right] + (1-\alpha_f)\,\boldsymbol{g}^{n,k} + \alpha_f \boldsymbol{g}^{n-1}, \tag{2.42}$$

$$\boldsymbol{M} \left[(1-\alpha_m)\,\hat{\ddot{\boldsymbol{d}}}^{n,k} + \alpha_m \ddot{\boldsymbol{d}}^{n-1} \right] + (1-\alpha_f)\,\boldsymbol{R} \left(\hat{\boldsymbol{d}} \right)^{n,k} + \alpha_f \boldsymbol{R} \left(\boldsymbol{d} \right)^{n-1} = (1-\alpha_f) \left(\boldsymbol{F}_H^{n,k} + \boldsymbol{G}^{n,k} \right) + \alpha_f \left(\boldsymbol{F}_H^{n-1} + \boldsymbol{G}^{n-1} \right), \tag{2.43}$$

$$\hat{\boldsymbol{d}}^{n,k} = \boldsymbol{d}^{n-1} + \Delta t \dot{\boldsymbol{d}}^{n-1} + \Delta t^2 \left[(0.5 - \beta)\, \ddot{\boldsymbol{d}}^{n-1} + \beta \hat{\ddot{\boldsymbol{d}}}^{n,k} \right], \tag{2.44}$$

$$\hat{\dot{\boldsymbol{d}}}^{n,k} = \dot{\boldsymbol{d}}^{n-1} + \Delta t \left[(1 - \gamma)\, \ddot{\boldsymbol{d}}^{n-1} + \gamma \hat{\ddot{\boldsymbol{d}}}^{n,k} \right], \tag{2.45}$$

where k is the iteration index, and $\hat{\boldsymbol{d}}^{n,k}$, $\hat{\dot{\boldsymbol{d}}}^{n,k}$ and $\hat{\ddot{\boldsymbol{d}}}^{n,k}$ are the intermediate displacement, velocity and acceleration vectors, respectively. An under-relaxation scheme is applied to the intermediate displacement vector:

$$\boldsymbol{d}^{n,k} = \boldsymbol{d}^{n,k-1} + \omega^{n,k} \left(\hat{\boldsymbol{d}}^{n,k} - \boldsymbol{d}^{n,k-1} \right), \tag{2.46}$$

where $\omega^{n,k}$ is the under-relaxation factor at the kth iteration. The acceleration and velocity vectors are obtained as

$$\ddot{\boldsymbol{d}}^{n,k} = \frac{\boldsymbol{d}^{n,k} - \boldsymbol{d}^{n-1} - \Delta t \dot{\boldsymbol{d}}^{n-1}}{\beta \Delta t^2} - \left(\frac{1}{2\beta} - 1 \right) \ddot{\boldsymbol{d}}^{n-1}, \tag{2.47}$$

$$\dot{\boldsymbol{d}}^{n,k} = \dot{\boldsymbol{d}}^{n-1} + \Delta t \left[(1 - \gamma)\, \ddot{\boldsymbol{d}}^{n-1} + \gamma \ddot{\boldsymbol{d}}^{n,k} \right]. \tag{2.48}$$

The under-relaxation factor for $k \geq 2$ is dynamically determined from the Aitken method (Kuttler & Wall, 2008; Irons & Tuck, 1969):

$$\omega^{n,k} = -\omega^{n,k-1} \frac{\left(\hat{\boldsymbol{d}}^{n,k-1} - \boldsymbol{d}^{n,k-2} \right)^T \left[\left(\hat{\boldsymbol{d}}^{n,k} - \boldsymbol{d}^{n,k-1} \right) - \left(\hat{\boldsymbol{d}}^{n,k-1} - \boldsymbol{d}^{n,k-2} \right) \right]}{\left| \left(\hat{\boldsymbol{d}}^{n,k} - \boldsymbol{d}^{n,k-1} \right) - \left(\hat{\boldsymbol{d}}^{n,k-1} - \boldsymbol{d}^{n,k-2} \right) \right|^2}. \tag{2.49}$$

Here, $\boldsymbol{d}^{n,0} = \boldsymbol{d}^{n-1}$, $\dot{\boldsymbol{d}}^{n,0} = \dot{\boldsymbol{d}}^{n-1}$, $\ddot{\boldsymbol{d}}^{n,0} = \ddot{\boldsymbol{d}}^{n-1}$, and $\omega^{n,1} = \max\left(\omega^{n-1}, 1\right)$.

2.3 Numerical examples

We apply an explicit two-step method with a free parameter ξ, equation (2.18), to determine the provisional velocity on the fluid-solid interface. The values of ξ considered are 3/2, 1 (corresponding to the explicit Euler method), 3/4, 1/2, 3/8, and 0. The linear stability analysis with $\chi = 0$ in Sec. 2.2.4 predicts the lowest density ratio at $\xi = 3/8$ for stable solutions. In this section, we show from numerical simulations that the optimal values of ξ providing the lowest density ratio is 3/4 ($\chi = 0$) and 1 ($\chi = 0.5$), and weak coupling employing the position and velocity predictors satisfies the overall second-order accuracy and requires much less computational time than strong coupling. Numerical examples of fluid-structure interaction include one rigid body and two elastic bodies. The results from the present weak coupling are compared with those from the present strong coupling and also from previous studies.

2.3.1 Vortex-induced vibration of a rigid circular cylinder

We simulate the motion of an elastically mounted rigid circular cylinder in a free stream. The dynamic equation for the motion of an elastically mounted rigid circular cylinder is same as equation (2.7) and is rewritten as

$$\ddot{X}_C + 2\zeta \left(\frac{2\pi}{U^*}\right) \dot{X}_C + \left(\frac{2\pi}{U^*}\right)^2 X_C = \frac{2}{\pi\rho} C_D \tag{2.50}$$

$$\ddot{Y}_C + 2\zeta \left(\frac{2\pi}{U^*}\right) \dot{Y}_C + \left(\frac{2\pi}{U^*}\right)^2 Y_C = \frac{2}{\pi\rho} C_L \tag{2.51}$$

where (X_C, Y_C), $\left(\dot{X}_C, \dot{Y}_C\right)$, $\left(\ddot{Y}_C, \ddot{Y}_C\right)$ are the displacement, velocity and acceleration of the center, respectively, $C_D = 2F_D/\left(\rho_f U^2 D\right)$ is the drag coefficient, $C_L = 2F_L/\left(\rho_f U^2 D\right)$ is the lift coefficient, F_D and F_L are the drag and lift

forces, respectively, and D is the diameter of a circular cylinder. The values of dimensionless material parameters are $\zeta = 0.01$, $U^* = 5$, $\rho = 4/\pi$, and the Reynolds number is 200.

Figure 2.4 shows the schematic diagram of the computational domain and boundary conditions. The computational domain size is [-10D, 30D] $\times$ [-10D, 10D], where the center of the circular cylinder is initially located at $(x, y) = (0, 0)$. The number of grid points is 897 $\times$ 481 in the streamwise (x) and transverse (y) directions. The smallest grid spacing near the cylinder surface is $\Delta x = \Delta y = 0.01D$. The Dirichlet boundary condition ($u = U$, $v = 0$) is applied at the inlet, top and bottom boundaries. A convective boundary condition ($\partial u_i/\partial t + u_c \partial u_i/\partial x = 0$) is used at the outlet boundary, where u_c is the streamwise velocity averaged over the outflow boundary. The computations are conducted at the maximum CFL number of 1 for weak coupling with $\xi = 1$ (equation (2.18)) and for strong coupling, and at $\Delta t = 0.004$ for weak coupling with $\xi = 3/2$, 3/4, 1/2, 3/8 and 0.

Table 2.1 shows the lowest density ratios (ρ_{min}) for stable solutions depending on the choices of ξ in the predictors (equation (2.18)) and χ in the second-order implicit generalized-α method for solid-body motion (equations (2.14), (2.16)–(2.17)), together with the computed origins of oscillations. As shown, ρ_{min} depends on the choices of ξ and χ. Because high-frequency motions are dissipated more at smaller χ (Chung & Hulbert, 1993), the solution becomes more stable at smaller χ: i.e., given ξ, ρ_{min} ($\chi = 0$) $\leq \rho_{min}$ ($\chi = 0.5$). Although the stability analysis predicts $\xi = 3/8$ ($\chi = 0$) for the possible lowest density ratio, the present numerical simulations show that the lowest density ratio for stable solutions is obtained at $\xi = 3/4$, and its values ($\rho_{min} = 0.21$) is much lower than 1. This value obtained from the present weak coupling is lower than that ($\rho_{min} = 1.08$) of weak coupling in Yang *et al.* (2008). On the

		WC												SC	
χ		0.0						0.5						0.0	0.5
ξ		0	3/8	1/2	3/4	1	3/2	0	3/8	1/2	3/4	1	3/2	-	-
ρ	0.70	1.15						×	×	1.15				1.14	1.15
	0.67	1.20								×					
	0.66	×													
	0.50		1.62				1.62				1.62			1.61	1.61
	0.43		1.88								×				
	0.42		×												
	0.41						1.98								
	0.40			2.03			×						2.03	2.02	2.02
	0.39												×		
	0.35			2.32											
	0.34			×											
	0.30				2.71	2.71						2.71		2.70	2.70
	0.28					2.90						×			
	0.27					×									
	0.21				3.87									3.85	3.85
	0.20				×									4.04	4.04

Table 2.1. Lowest density ratios for stable solutions depending on the predictors, and the values of origin of oscillations for an elastically mounted rigid circular cylinder. Here, WC and SC denote the weak and strong coupling, respectively, and × does the divergence of solution.

	$\bar{X}_C/D$	$St\,(=fD/U)$
Present simulation (weak coupling with $\xi = 1$ and $\chi = 0.5$)	0.623	0.186
Present simulation (strong coupling with $\chi = 0.5$)	0.622	0.186
Blackburn & Karniadakis (1993) (weak coupling)	0.620	-
Yang *et al.* (2008) (weak coupling)	0.639	-
Yang & Stern (2015) (strong coupling)	-	0.187

Table 2.2. Origin of oscillations and oscillation frequency of an elastically mounted rigid circular cylinder with $\rho = 4/\pi$. Here, $\bar{X}_C$ is the origin of oscillations.

other hand, strong coupling provides stable solutions for all ρ's considered, and its solutions agree well with those of weak coupling (Table 2.1). However, the average number of iterations per time step for strong coupling is about 6.7 for the convergence criterion of $\left|\dot{X}_C^{n,k} - \dot{X}_C^{n,k-1}\right|$ and $\left|\dot{Y}_C^{n,k} - \dot{Y}_C^{n,k-1}\right| < 10^{-5}$, which increases the CPU time by about a factor of 6 to 7 as compared to that of weak coupling.

Figure 2.5 shows the trajectories of the center of an elastically mounted rigid circular cylinder with $\rho = 4/\pi$ by weak coupling ($\xi = 1$ and $\chi = 0.5$) and strong coupling ($\chi = 0.5$), together with those of previous studies (Blackburn & Karniadakis, 1993; Yang *et al.*, 2008). The circular cylinder reaches a periodic state and draws a figure of eight motion. The trajectories from weak and strong coupling also agree well with those of Blackburn & Karniadakis (1993) and Yang *et al.* (2008), although the trajectory of Yang *et al.* (2008) is slightly shifted to the downstream side. The origin of oscillations and the oscillation frequency are compared with those of Blackburn & Karniadakis (1993), Yang *et al.* (2008) and Yang & Stern (2015) in Table 2.2, showing good agreements with others. Figure 2.6 shows the contours of the instantaneous vorticity around the circular

cylinder. The vortex shedding shown in this figure corresponds to a 2S vortex pattern (two single vortices shed during one oscillation period) and its pattern agrees well with that of Yang & Stern (2015).

To estimate the order of accuracy, γ_N, the Richardson-estimation procedure is used as in Gilmanov & Sotiropoulos (2005):

$$g_{exact} = g_N + Ch_N^{\gamma_N} + O\left(h_N^{\gamma_N+1}\right), \tag{2.52}$$

$$\gamma_N \approx \left[\log\left(\left|g_N - g_{N/2}\right| / \left|g_{N/2} - g_{N/4}\right|\right)\right] / (\log 2), \tag{2.53}$$

where g_{exact} is the exact solution, g_N is the numerical solution, h_N is the uniform grid spacing of the N^2 mesh, C is an unknown constant (but not dependent on h_N), and N is the number of grid points. The computational domain size is [-2D, 7.6D] $\times$ [-4.8D, 4.8D] following Yang & Stern (2015), and six different N's are considered such as N = 1601, 1761, 1921, 2081, 2241, 2401. The computational time step is determined as $\Delta t = h_N/(5U)$. Figure 2.7 shows the values of γ_N for the maximum transverse displacement and velocity with the number of grid points. The results show that $\gamma_N \geq 2$ for $N \geq 2081$, achieving the overall second-order accuracy.

2.3.2 Vortex-induced vibration of an elastic beam

We simulate flow around an elastic beam attached to the base of a stationary circular cylinder in a channel. The results are compared with those of Turek & Hron (2006), Breuer *et al.* (2012) and Tian *et al.* (2014). Here, Turek & Hron (2006) used a fully implicit monolithic approach, and Tian *et al.* (2014) and Breuer *et al.* (2012) adopted a strong coupling approach. Figure 2.8 shows the

schematic diagram of the computational domain and boundary conditions. The length and thickness of the beam are $L_b = 3.5D$ and $h_b = 0.2D$, respectively, where D is the diameter of a circular cylinder. The computational domain size is [-1.5D, 23.5D] $\times$ [-2D, 2.1D] following Turek & Hron (2006) and Breuer *et al.* (2012). The number of grid points is 769 $\times$ 409 in the streamwise (x) and transverse (y) directions. The smallest grid spacing is $\Delta x = 0.0125D$ and $\Delta y = 0.01D$. A parabolic velocity profile, $u/U = 1.5(2 + y/D)(2.1 - y/D)/2.05^2$, is applied at the inlet boundary. The no-slip condition ($u = v = 0$) is imposed at the top and bottom boundaries. A convective boundary condition is used at the outlet boundary.

The Saint Venant-Kirchhoff model (equation (2.13)) is considered as a solid material model and the number of elements is 36 $\times$ 1 in the length and thickness directions. The Reynolds number is $\mathrm{Re} = \rho_f UD/\mu_f = 200$. The values of parameters are $D = 0.1\,\mathrm{m}$, $U = 2\,\mathrm{m/s}$, $\rho_f = 1000\,\mathrm{kg/m^3}$, $\mu_f = 1\,\mathrm{kg/(m \cdot s)}$, $\rho_s^0 = 300 \sim 1000\,\mathrm{kg/m^3}$, $E_s = 5.6 \times 10^6\,\mathrm{N/m^2}$, and $\nu_s = 0.4$. The present computations are conducted at the maximum CFL number of 1 for weak coupling with $\xi = 1$ and for strong coupling, and at $\Delta t = 0.0002\,\mathrm{s}$ for weak coupling with $\xi = 3/2$, 3/4, 1/2, 3/8 and 0, respectively.

Figure 2.9 shows the time traces of the point A in figure 2.8 for $\rho_s^0 = 1000\,\mathrm{kg/m^3}$. The predicted transverse locations of the point A from present weak and strong coupling agree well with that of Turek & Hron (2006). The mean drag coefficient $\left(\bar{C}_D = \bar{C}_{D,cylinder} + \bar{C}_{D,beam}\right)$ and Strouhal number ($St = fD/U$) are listed in Table 2.3 and compared with those of Turek & Hron (2006), Breuer *et al.* (2012) and Tian *et al.* (2014), showing excellent agreements.

Table 2.4 shows the lowest density ratios ($\rho_{min} = \rho_s^0/\rho_f$) for stable solutions depending on the choices of ξ in the predictors (equation (2.18)) and χ in the second-order implicit generalized-α method for solid-body motion (equations

	$\bar{C}_D$	$St\,(=fD/U)$
Present simulation (weak coupling with $\xi = 1$ and $\chi = 0.5$)	2.30	0.28
Present simulation (strong coupling with $\chi = 0.5$)	2.30	0.28
Turek & Hron (2006) (monolithic)	2.29	0.26
Breuer *et al.* (2012) (strong coupling)	2.32	0.26
Tian *et al.* (2014) (strong coupling)	2.16	0.29

Table 2.3. Mean drag coefficient and Strouhal number for $\rho_s^0 = \rho_f = 1000\,\mathrm{kg}\,/\,\mathrm{m}^3$.

(2.15)–(2.17)), together with the computed mean drag coefficients. As observed in Sec. 2.3.1, ρ_{min} depends on the choices of ξ and χ. Weak coupling with $\chi = 0$ provides lower ρ_{min}'s than that with $\chi = 0.5$. The optimal ξ (=3/4) obtained from numerical simulations is larger than that ($\xi = 3/8$) from the stability analysis, and ρ_{min} (= 0.31) for $\xi = 3/4$ is much lower than that (ρ_{min} = 1.26) for $\xi = 3/8$ (Table 2.4), again indicating that the present stability analysis in Sec. 2.2.4 provides narrower density ratio for stable solutions. On the other hand, strong coupling provides stable solutions for all ρ's considered, and its solutions agree well with those of weak coupling (Table 2.4). However, the average number of iterations per time step for strong coupling at $\rho_s^0/\rho_f = 1$ is about 4.2 for the convergence criterion of $\|\dot{\boldsymbol{d}}^{n,k} - \dot{\boldsymbol{d}}^{n,k-1}\|_\infty < 10^{-4}$, which increases the CPU time by about a factor of 4 to 5 as compared to that of weak coupling.

2.3.3 Bending of a flexible plate

We simulate flow around a flexible plate, as shown in figure 2.10. The bottom surface of the plate is clamped, while other parts are allowed to freely

		WC												SC
χ		0.0						0.5						0.5
ξ		0	3/8	1/2	3/4	1	3/2	0	3/8	1/2	3/4	1	3/2	-
$\rho\ (=\rho_s^0/\rho_f)$	2.30	2.41						×	2.41	2.41				2.41
	2.28	2.40												
	2.27	×							2.40	2.40				
	1.30		2.32						×	×	2.32			2.32
	1.26		2.32											
	1.25		×								2.32			
	1.00			2.30						×	×	2.30	2.30	2.30
	0.91			2.30										
	0.90			×									2.30	2.29
	0.70						2.28						×	2.28
	0.65						2.28							
	0.64						×							
	0.50					2.27						2.27		2.27
	0.42					2.27						×		
	0.41					×								
	0.40				2.27									2.27
	0.31				2.27									
	0.30				×									2.27

Table 2.4. Lowest density ratios for stable solutions depending on the predictors, and the values of mean drag coefficient. Here, WC and SC denote the weak and strong coupling, respectively, and × does the divergence of solution.

move. The plate has the width L, height H_p (= $5L$), and thickness h_p (= $0.2L$). The computational domain size is [-$5L$, $16L$] × [0, $17L$] × [-$8L$, $8L$]. The number of grid points is 201 × 191 × 161 in the streamwise (x), transverse (y), and spanwise (z) directions. The smallest grid spacing is $\Delta x = \Delta y = \Delta z = 0.02L$. The Dirichlet boundary condition ($u = U$, $v = w = 0$) is applied at the inlet, top, bottom, and lateral side boundaries. A convective boundary condition is used at the outlet. The Saint Venant-Kirchhoff model (equation (2.13)) is used as a solid material model and the number of elements is 4 × 20 × 1 in the width, height and thickness directions. The values of non-dimensional parameters are $\mathrm{Re} = \rho_f UL/\mu_f = 1600$, $\rho_s^0/\rho_f = 0.678$, $E_s/(\rho_f U^2) = 19054.9$, $\nu_s = 0.4$, and $(\rho_f - \rho_s^0)\, gh/(\rho_f U^2) = 0.2465$ (Tian *et al.*, 2014), where g is the gravitational acceleration. The buoyancy force is also applied on the plate. The present computations are conducted at the maximum CFL number of 1 for weak coupling with $\xi = 1$, and at $\Delta t = 0.004$ for weak coupling with $\xi = 3/2$, 3/4, 1/2, 3/8 and 0, respectively.

Figure 2.11 shows the time traces of the streamwise and transverse displacements of the center of the free end (point A). The plate is largely deflected along the streamwise direction due to the cross flow. It shows that different values of ξ and χ little change the solutions once they are stable. The mean drag coefficient and mean streamwise and transverse displacements of the point A are listed in Table 2.5, together with those of Luhar & Nepf (2011) and Tian *et al.* (2014). For the given density ratio of 0.678, the solutions become stable only for three sets of parameter values (ξ, χ) = (0.75, 0), (1, 0) and (1, 0.5) with weak coupling. The stable solutions show good agreements with those of Luhar & Nepf (2011) (experiment) and Tian *et al.* (2014) (numerical simulation). Figure 2.12 shows the instantaneous vortical structures around the flexible plate, where the vortical structures are identified by the iso-surface of

	χ	ξ	$\bar{C}_D$	$\bar{d}_{xA}/L$	$\bar{d}_{yA}/L$
WC	0.0	3/2	×	× ×	
		1	1.09	2.14	0.56
		3/4	1.12	2.19	0.59
		1/2	×	×	×
		3/8	×	×	×
		0	×	×	×
	0.5	3/2	×	×	×
		1	1.13	2.20	0.59
		3/4	×	×	×
		1/2	×	×	×
		3/8	×	×	×
		0	×	×	×
Luhar & Nepf (2011) (experiment)			1.15	2.14	0.59
Tian *et al.* (2014) (strong coupling)			1.03	2.12	0.54

Table 2.5. Mean drag coefficients and mean streamwise and transverse displacements of the point A ($\rho_s^0/\rho_f = 0.678$). Here, WC denotes weak coupling and × denotes the divergence of solution.

λ_2 = -20 (Jeong & Hussain, 1995). Shear layer vortices are formed near the free end and complex three-dimensional vortical structures are generated in the wake.

2.4 Summary

In the present study, we suggested a weak coupling method for fluid-structure interaction problems without any iteration per time step, especially for low density ratios of solid to fluid. To achieve accurate and stable solutions, we introduced predictors to provide provisional position and velocity of fluid-structure interface at each time step. The provisional velocity and position were obtained using an explicit two-step method with a parameter ξ and the implicit Euler method, respectively. The incompressible Navier-Stokes equations were solved in the Eulerian coordinate, and the no-slip condition on the fluid-structure interface was satisfied using an immersed boundary method (Kim *et al.*, 2001). The dynamic equation was solved in the Lagrangian coordinate with hydrodynamic forces exerted on the fluid-structure interface.

A linear stability analysis was performed for weak coupling to obtain a stability limit of the density ratio assuming that the convection and viscous terms in fluid flow and the internal force in structure motion are negligible. It was shown that the stability condition depends on the parameter ξ in the predictor and the lowest density ratio was achieved at $\xi = 3/8$ ($\chi = 0$). Numerical simulations were conducted for three different fluid-structure interaction problems with the present weak coupling: flows around an elastically mounted rigid circular cylinder, an elastic beam attached to the base of a stationary circular cylinder, and a flexible plate, respectively. Actual simulations provided that the lowest density ratio for stable solutions is achieved at $\xi = 3/4$ ($\chi = 0$)

and its value is much lower than that at $\xi = 3/8$, indicating that the present stability analysis provides narrower density ratio for stable solutions because of the assumptions made during the analysis. The lowest possible density ratios obtained for the present fluid-structure interaction problems were much lower than 1. The results from the present weak coupling agreed well with those from previous studies and from strong coupling suggested in this study, proving the accuracy and efficiency of present weak coupling.

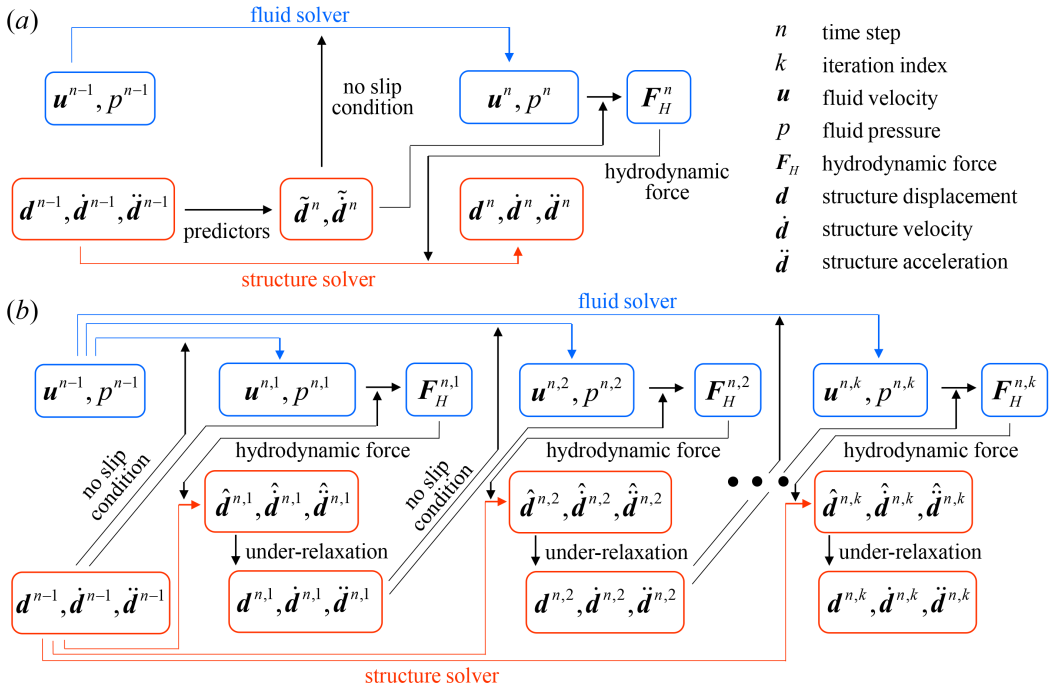

Figure 2.1. Procedures of (a) weak coupling with predictors and (b) strong coupling using an iterative scheme with an under-relaxation scheme. Here, the Navier-Stokes equations are solved with a linearlized fully implicit method, and the dynamic equation for an elastic solid-body motion is iteratively solved with a fully implicit method.

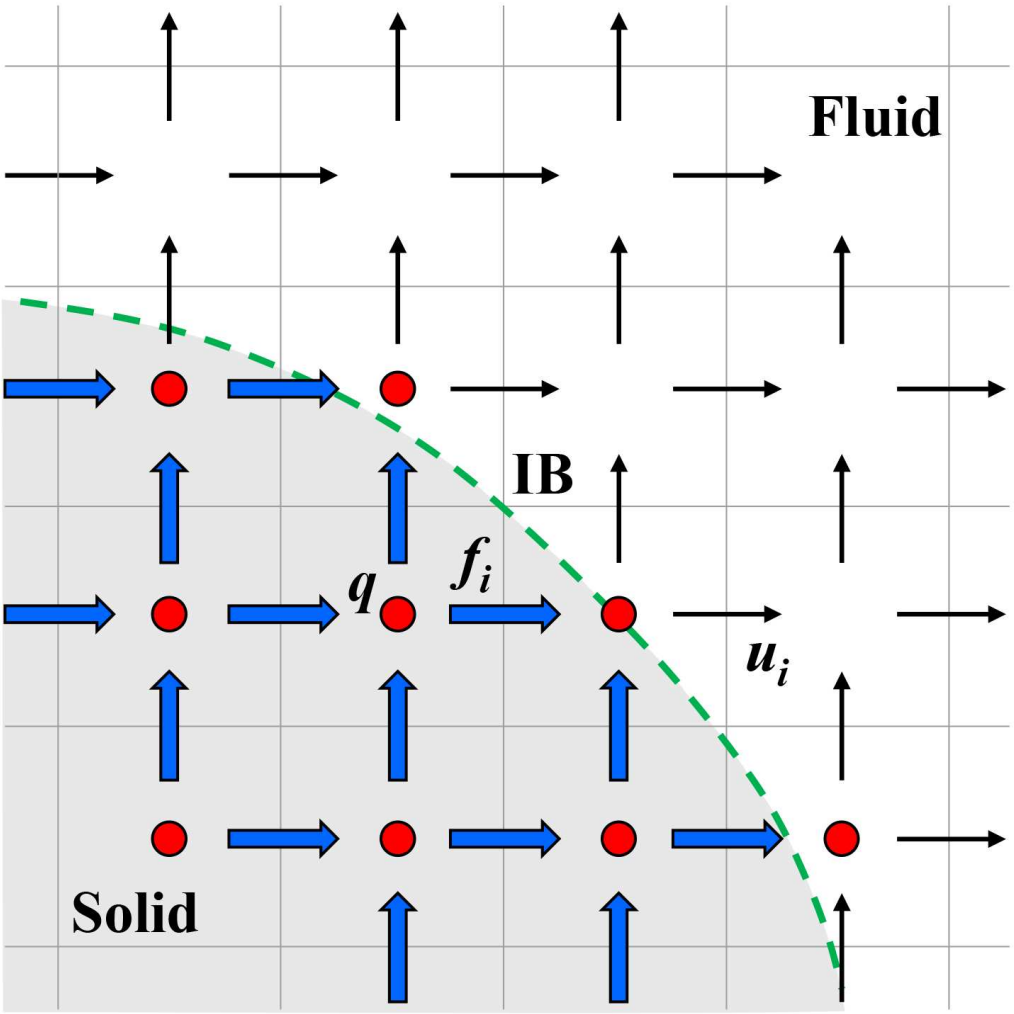

Figure 2.2. Schematic diagram of a discrete-forcing IB method (Kim *et al.*, 2001).

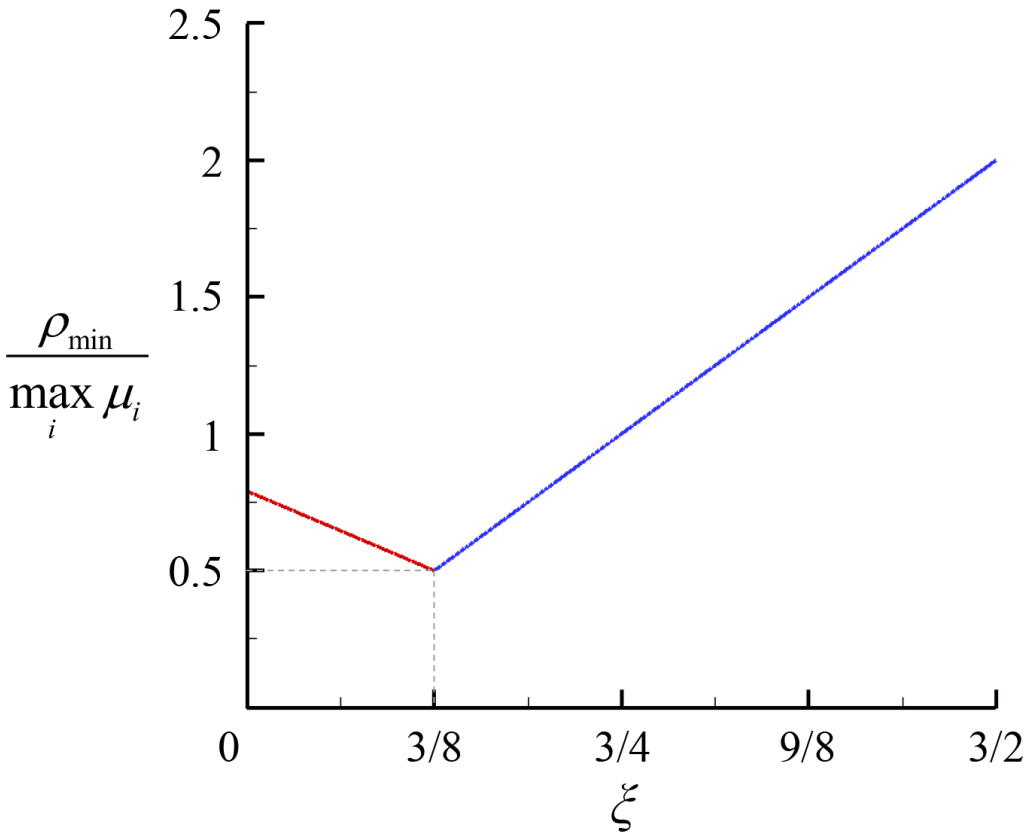

Figure 2.3. Lowest density ratio from the present stability analysis for weak coupling with $\chi = 0$: ——, $\rho_{min}/\max_i \mu_i = \left(-3\xi + \sqrt{9\xi^2 - 40\xi + 40}\right)/8$ for $\xi \leq 3/8$; ——, $4\xi/3$ for $\xi > 3/8$.

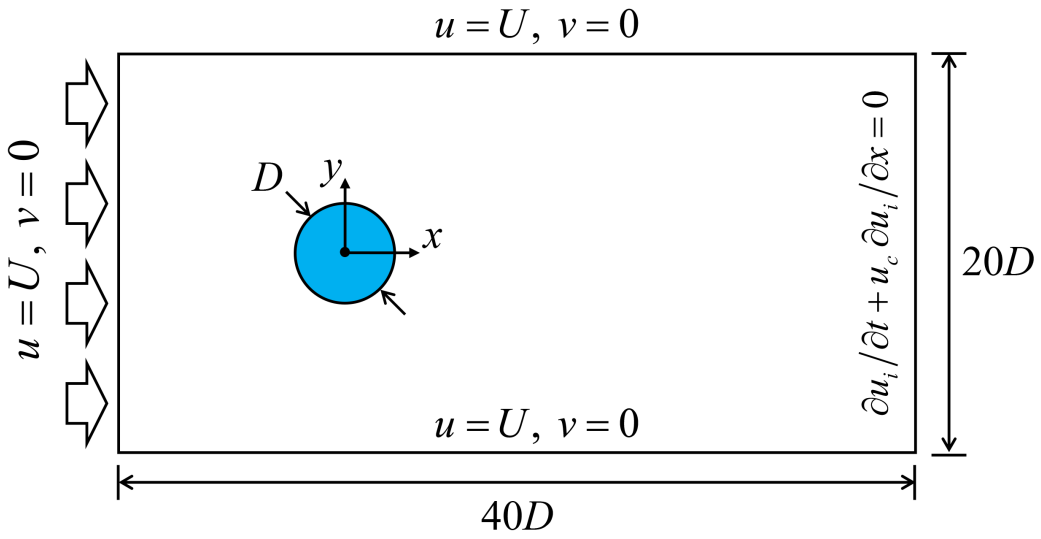

Figure 2.4. Schematic diagram of the computational domain and boundary conditions for the simulation of flow around an elastically mounted rigid circular cylinder.

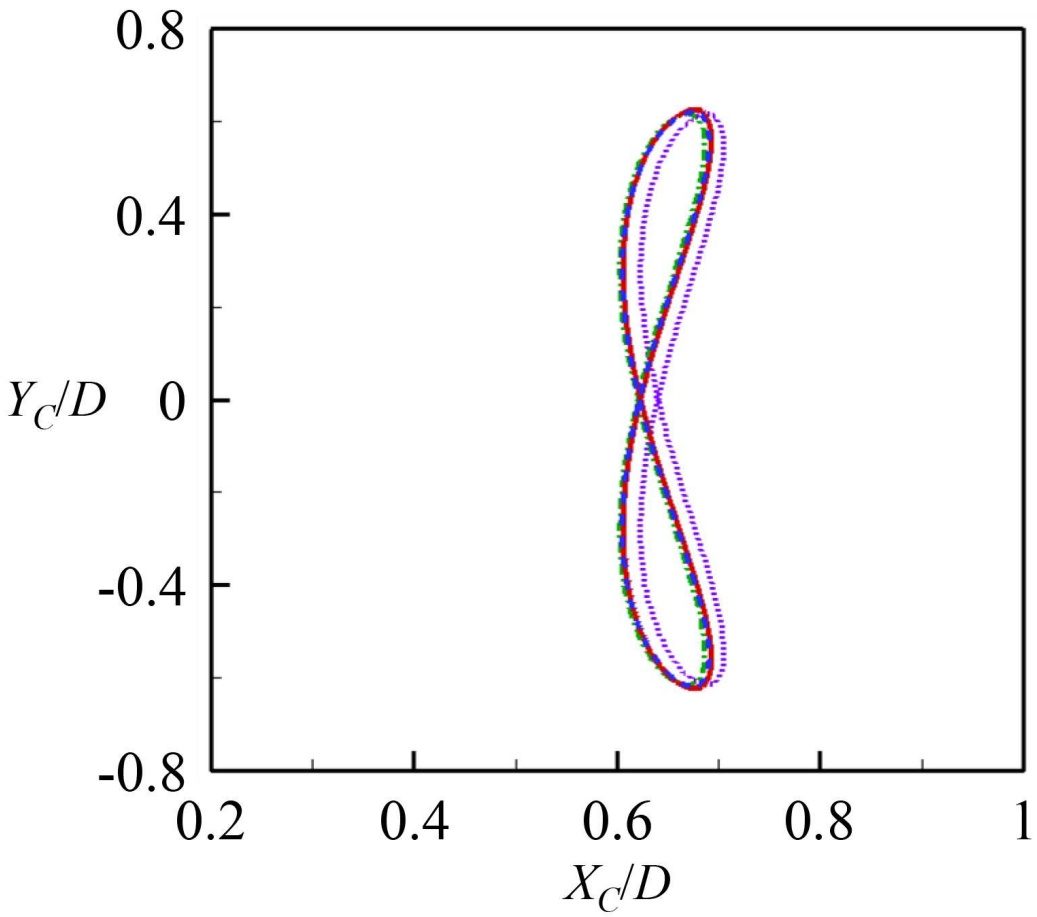

Figure 2.5. Trajectory of the center of an elastically mounted rigid circular cylinder with $\rho = 4/\pi$: ——, present simulation (weak coupling with $\xi = 1$ and $\chi = 0.5$); – – –, present simulation (strong coupling with $\chi = 0.5$); - - -, Blackburn & Karniadakis (1993); - - - - -, Yang *et al.* (2008).

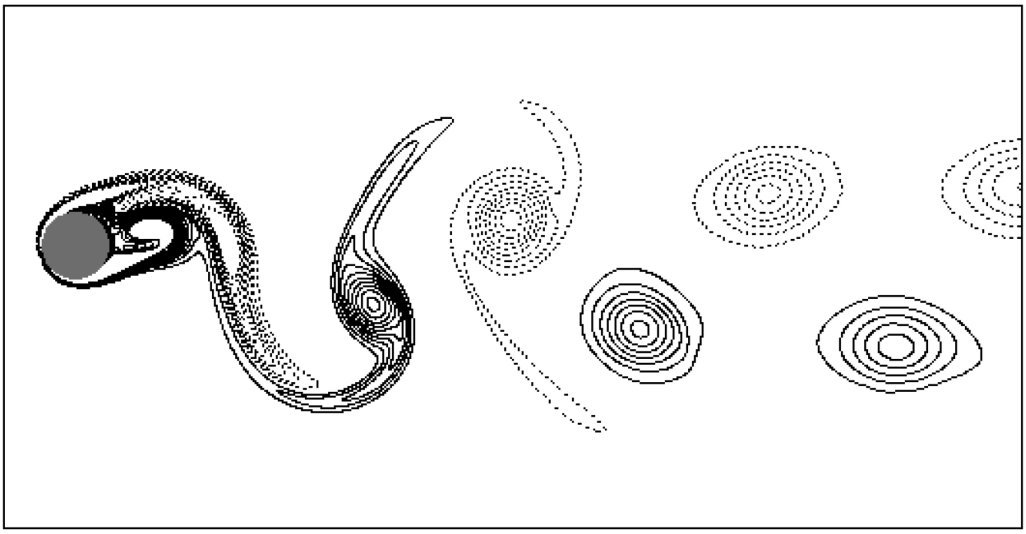

Figure 2.6. Contours of the instantaneous vorticity around an elastically mounted rigid circular cylinder, obtained from weak coupling with $\xi = 1$ and $\chi = 0.5$.

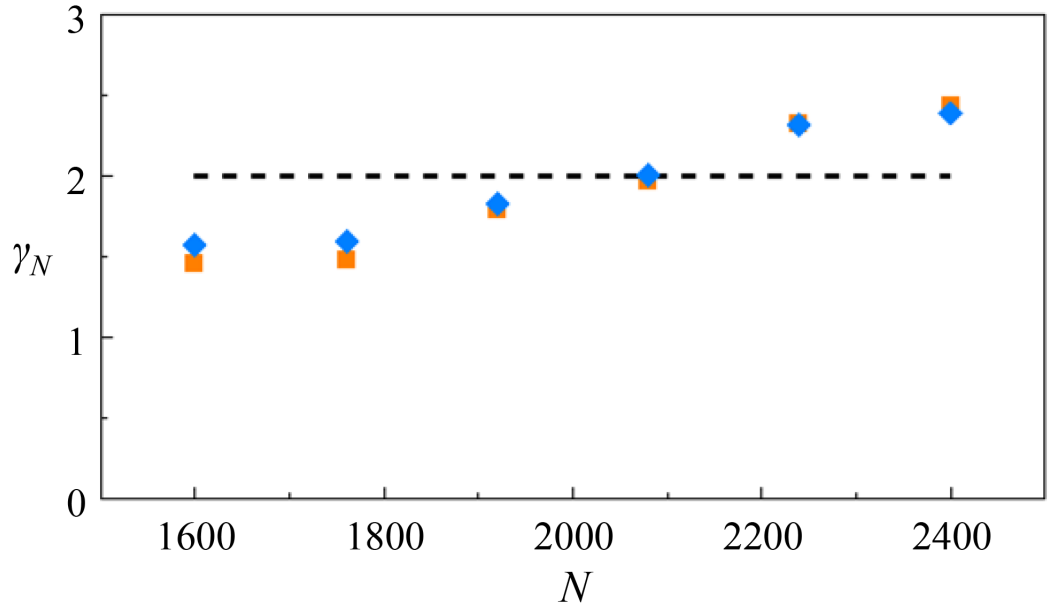

Figure 2.7. Numerical accuracy of the present method (weak coupling with $\xi = 3/4$ and $\chi = 0$) for flow around an elastically mounted rigid circular cylinder: ■, maximum transverse displacement; ♦, maximum transverse velocity. The dashed line indicates $\gamma_N = 2$.

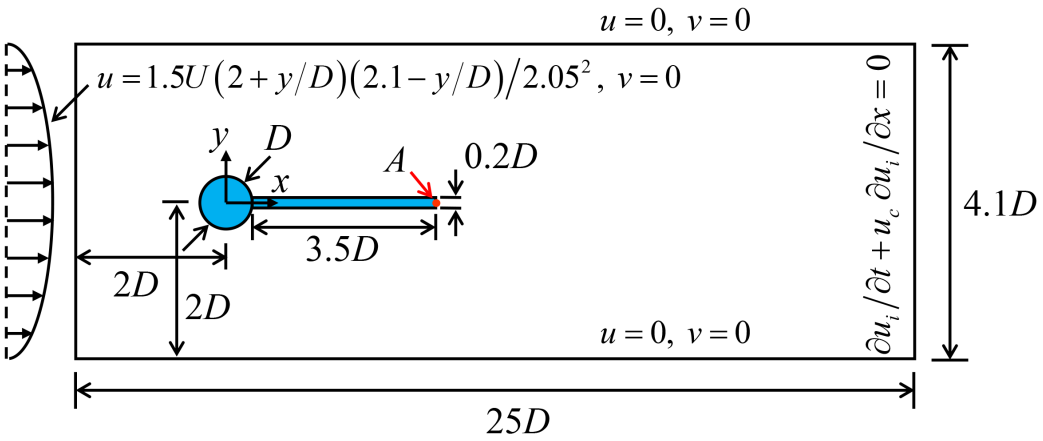

Figure 2.8. Schematic diagram of the computational domain and boundary conditions for the simulation of flow around an elastic beam attached to base of a stationary circular cylinder in a channel.

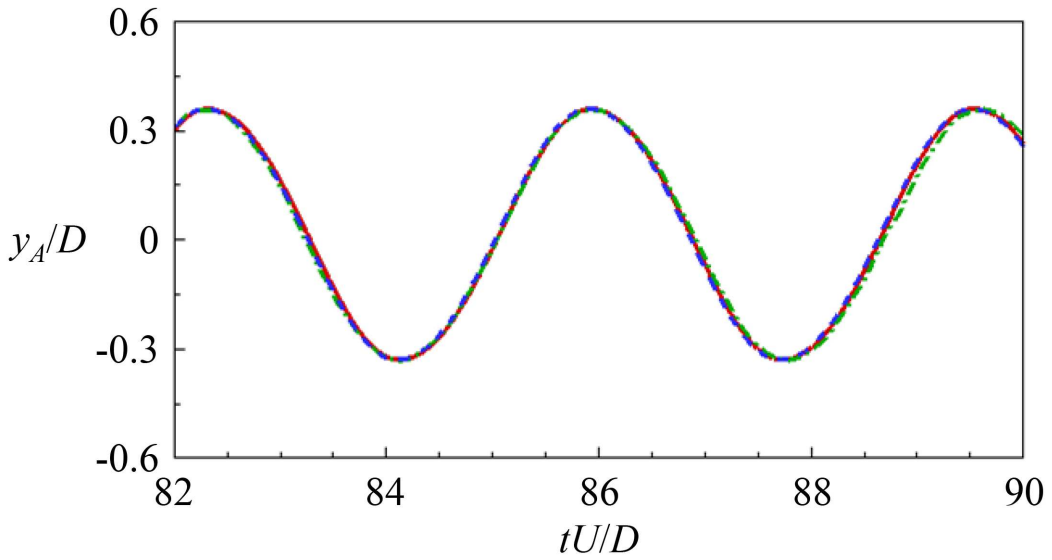

Figure 2.9. Time traces of the point A (in figure 2.8) of an elastic beam for $\rho_s^0 = \rho_f = 1000\,\mathrm{kg}\,/\,\mathrm{m}^3$: ——, present study (weak coupling with $\xi = 1$ and $\chi = 0.5$); – – –, present study (strong coupling with $\chi = 0.5$); – - –, Turek & Hron (2006).

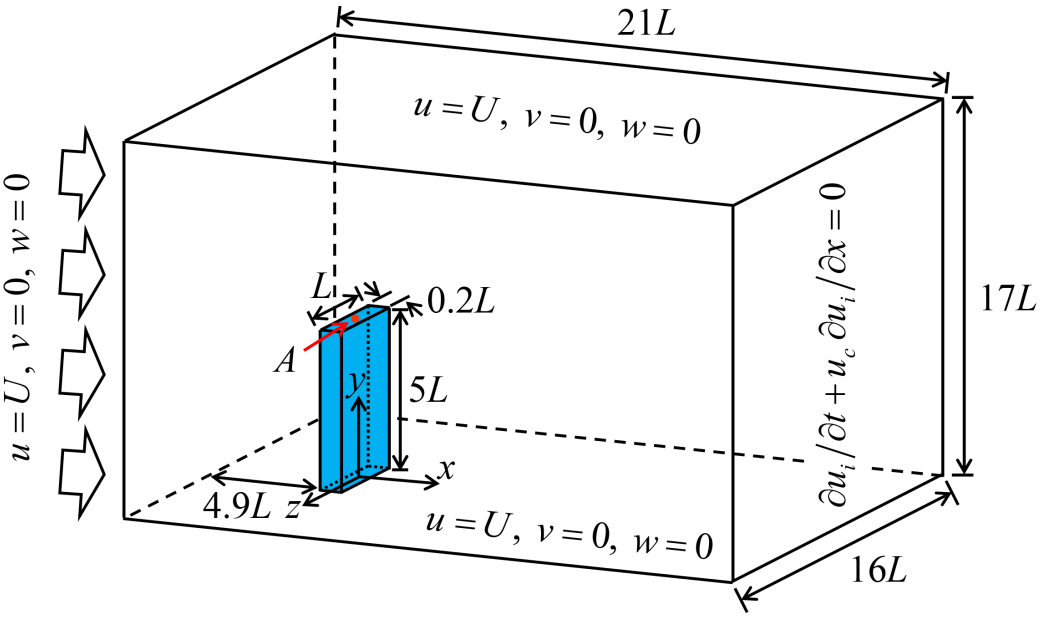

Figure 2.10. Schematic diagram of the computational domain and boundary conditions for the simulation of flow around a flexible plate.

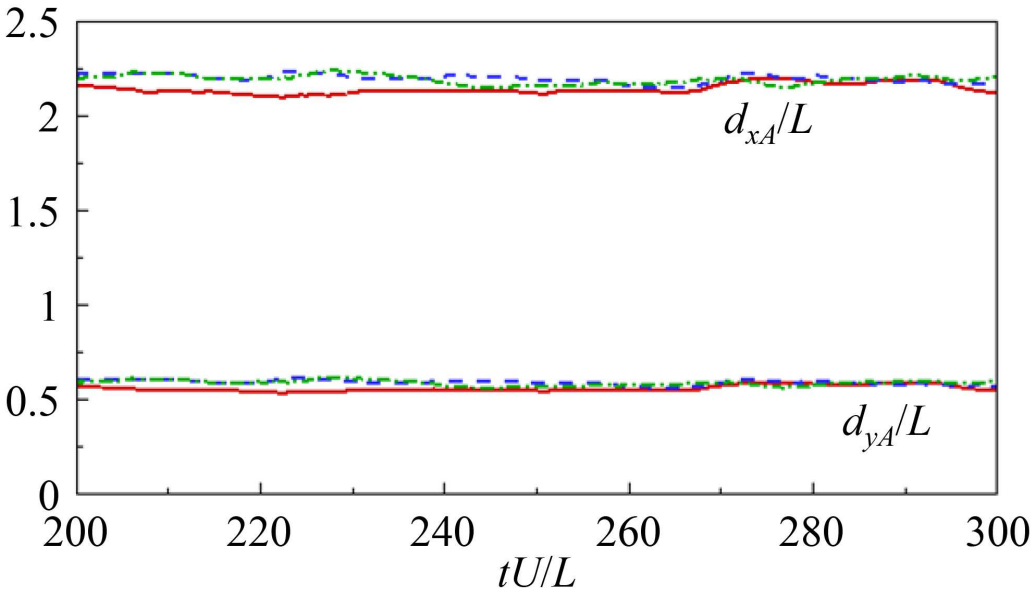

Figure 2.11. Time traces of the streamwise and transverse displacements of the point A in figure 2.10: ——, weak coupling with $\xi = 1$ and $\chi = 0$; – – –, weak coupling with $\xi = 1$ and $\chi = 0.5$; – - –, weak coupling with $\xi = 3/4$ and $\chi = 0$.

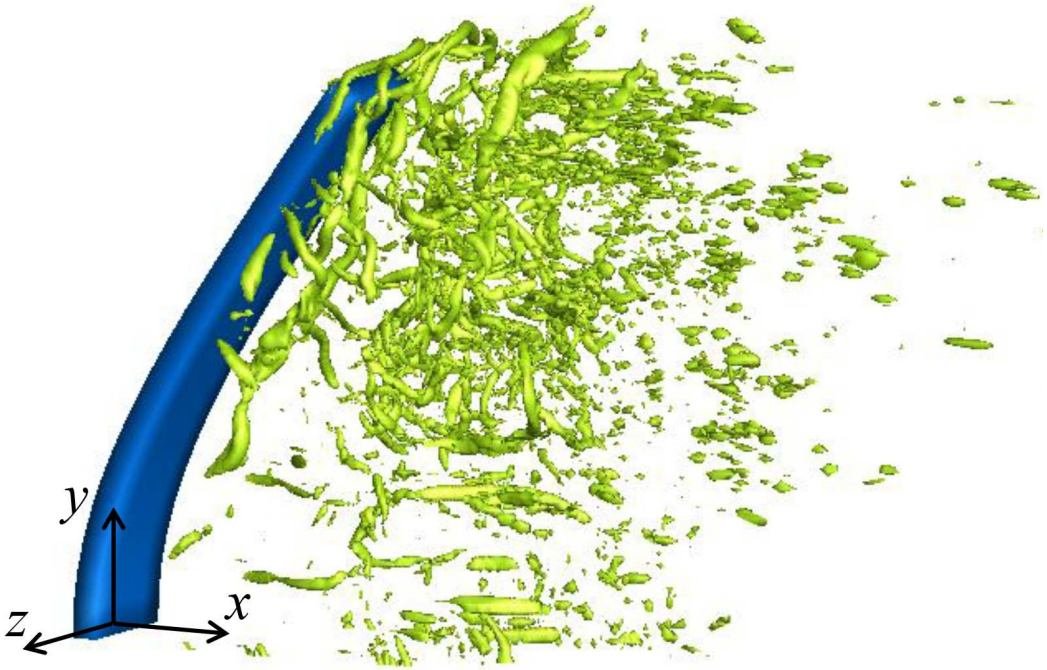

Figure 2.12. Instantaneous vortical structures around a flexible plate, obtained from weak coupling with $\xi = 1$ and $\chi = 0.5$.

Chapter 3

Vortex-induced vibrations of an elastically mounted rigid circular cylinder and flexible circular cylinder, and controls for them

3.1 An elastically mounted rigid cylinder in a uniform current

3.1.1 Motivations and objectives

It is important to understand vortex-induced vibration of a long flexible circular cylinder to lower fatigue damage. However, there are many challenges in understanding and predicting for the response of a long flexible circular cylinder (Bearman, 2011): a large facility and relatively complicated instrumentation for experiments (Wu *et al.*, 2012) and a high performance computing resource for numerical simulations. Instead, the fundamental research on vortex-induced vibration has been extensively performed for an elastically mounted rigid circular cylinder although there is a need for an appreciation of the similarities and differences in the responses between a long flexible circular cylinder and an elastically mounted rigid circular cylinder (Bearman, 2011). There are comprehensive reviews of vortex-induced vibration of an elastically mounted rigid circular cylinder (Bearman, 1984; Sarpkaya, 2004; Williamson & Govardhan, 2004; Gabbai & Benaroya, 2005; Williamson & Govardhan, 2008; Bearman, 2011).

An elastically mounted rigid cylinder is modeled as a mass-damper-spring system, and its motion in a flow is driven by hydrodynamic force. Many previous studies investigated vortex-induced vibration of an elastically mounted rigid circular cylinder allowed to move only in the transverse direction and found that the amplitude of vibration is affected by the reduced velocity (U^*), mass ratio (m^*), and damping ratio (ζ) (Feng, 1968; Williamson & Roshko, 1988; Khalak & Williamson, 1999; Govardhan & Williamson, 2000). Typically, the peak amplitude of vibration is observed near $U^* = 5 \sim 7$ due to the lock-in. The regime of vortex induced vibration with one degree of freedom in the transverse direction is classified into initial and lower branches for high mass-damping systems (Feng, 1968). On the other hand, for low mass-damping systems, upper branch with large amplitude ($\approx 0.9D$) of vibration appears between the initial and lower branches (Khalak & Williamson, 1999). Two single vortices shed per cycle (2S mode) in the initial branch and two pairs of vortices shed per cycle (2P mode) in the upper and lower branches (Khalak & Williamson, 1999; Govardhan & Williamson, 2000).

The vibration of an elastically mounted rigid circular cylinder is affected by the degrees of freedom when the mass ratio is low. Jauvtis & Williamson (2004) found the super-upper branch with very large amplitude ($\approx 1.5D$ at $U^* = 7$) when an elastically mounted rigid circular cylinder with the mass ratio of 2.6 and damping ratio of 0.0036 is allowed to move in the streamwise and transverse directions. The super-upper branch was also observed through experiments (Dahl *et al.*, 2007; Blevins & Coughran, 2009) and numerical simulations (Zhao *et al.*, 2012; Gsell *et al.*, 2016; Kang *et al.*, 2017). Two triplets of vortices per cycle (2T mode) were observed in the super-upper branch (Jauvtis & Williamson, 2004; Dahl *et al.*, 2007; Zhao *et al.*, 2012; Kang *et al.*, 2017), and the massive amplitude of vibration for the 2T mode is principally attributed to the energy

transfer from the 'third' vortex of each triplet (Jauvtis & Williamson, 2004). However, Gsell *et al.* (2016) observed the 2S mode instead of the 2T mode in the super-upper branch with the maximum amplitude of $1.2D$ at $U^* = 6.5$, which indicates that there would be other factors causing very large amplitude vibration in the super-upper branch. Therefore, it is necessary to reveal the cause of very large amplitude vibration in the super-upper branch.

Many control methods have been developed to suppress vortex-induced vibration of an elastically mounted rigid circular cylinder regardless of flow incidence angle. Helical strakes have been most widely used to suppress vortex-induced vibration of an elastically mounted rigid circular cylinder (Zdravkovich, 1981; Bearman & Brankovic, 2004; Ding *et al.*, 2004; Zhou *et al.*, 2011; Quen *et al.*, 2014; Sui *et al.*, 2016). However, the mean drag coefficient of an elastically mounted rigid circular cylinder with helical strakes is higher than that of a stationary circular cylinder although helical strakes successfully suppress vortex-induced vibration of an elastically mounted rigid circular cylinder (Zdravkovich, 1981; Ding *et al.*, 2004; Quen *et al.*, 2014). The mean drag coefficient of a stationary circular cylinder with hemispherical bumps is maximally reduced up to 25% compared with a stationary circular cylinder but vortex-induced vibration is not significantly reduced by hemispherical bumps (Owen *et al.*, 2001; Bearman & Brankovic, 2004). To avoid the increase in drag owing to protrusions on the surface, Huang (2011) suggested helical grooves on the surface of a circular cylinder, and achieved the mean drag reduction up to 25% for a stationary circular cylinder with helical grooves at the subcritical Reynolds number range and the peak amplitude reduction by 64% for an elastically mounted rigid circular cylinder. However, the above mentioned control methods have not been applied to vortex-induced vibration with very large amplitude (i.e. the super-upper branch). Therefore, it is necessary to investigate the influence of control

methods on the vortex-induced vibration and mean drag in the super-upper branch.

Parametric studies were conducted for the stationary wavy cylinder with sinusoidally varying diameter along the spanwise direction (Lam & Lin, 2009) and helically twisted elliptic (HTE) cylinder with an elliptic cross section rotating along the spanwise direction (Kim *et al.*, 2016) to investigate the effects of parameters on the flow structures at the Reynolds number of 100. For the stationary HTE cylinder, the optimal wavelength and aspect ratio of the elliptic cross section are $3.5D$ and 1.3, respectively, for the Reynolds number of 100 and the optimal wavelength for the aspect ratio of 1.3 is $4D$ for the Reynolds number of 3900. At the Reynolds number of 100 and 3900, the optimal parameter for the stationary HTE cylinder results in suppression of vortex shedding and low lift fluctuations. However, it is not investigated for the effects of the wavelength and aspect ratio of the HTE cylinder on the flow around an elastically mounted rigid cylinder. Therefore, the present study will investigate the effects of the wavelength and aspect ratio of the HTE cylinder on the flow structures around and vortex-induced vibration of an elastically mounted rigid cylinder in the super-upper branch.

In this paper, computational details for flow around an elastically mounted rigid cylinder are given in section 3.1.2. The results of flows around elastically mounted rigid circular and HTE cylinders in the super-upper branch are presented in section 3.1.3 and section 3.1.4, respectively.

3.1.2 Computational details

Weak coupling presented in the section 2.2 is used to couple the governing equations of fluid flow (equations (2.3)–(2.6)) and rigid body motion (equations

(2.14), (2.16) and (2.17)) together with velocity and displacement predictors (equations (2.18) and (2.19)). Large eddy simulation with a dynamic global subgrid-scale mode is performed (Park *et al.*, 2006; Lee *et al.*, 2010). In the equation (2.14), gravitational force is not considered, and L^3 and V_s are corresponding to $L_z D^2$ and $L_z \pi D^2/4$ for a circular cylinder, where D is the diameter of a circular cylinder and L_z is the spanwise domain size. Then, the motion of an elastically mounted rigid circular cylinder is expressed as

$$\ddot{X}_C + 2\zeta \left(\frac{2\pi}{U^*}\right) \dot{X}_C + \left(\frac{2\pi}{U^*}\right)^2 X_C = \frac{2}{\pi m^*} C_D, \tag{3.1}$$

$$\ddot{Y}_C + 2\zeta \left(\frac{2\pi}{U^*}\right) \dot{Y}_C + \left(\frac{2\pi}{U^*}\right)^2 Y_C = \frac{2}{\pi m^*} C_L, \tag{3.2}$$

where (X_C, Y_C), $\left(\dot{X}_C, \dot{Y}_C\right)$, $\left(\ddot{Y}_C, \ddot{Y}_C\right)$ are the displacement, velocity and acceleration of the center, respectively, $\zeta \left(= c_s/2\sqrt{k_s m_s}\right)$ is the damping ratio, c_s is the damping coefficient, k_s is the spring constant, m_s is the structural mass, $U^* \left(= U/f_N D\right)$ is the reduced velocity, $f_N \left(= (1/2\pi)\sqrt{k_s/m_s}\right)$ is the natural vibration frequency, m^* is the mass ratio (the ratio of structural mass to displaced fluid mass), $C_D = 2F_D/\left(\rho_f U^2 D L_z\right)$ is the drag coefficient, $C_L = 2F_L/\left(\rho_f U^2 D L_z\right)$ is the lift coefficient, and F_D and F_L are the drag and lift forces, respectively. For very large amplitude vibration, the mass ratio is 2, the damping ratio is zero, the reduced velocity is 6 (super-upper branch), and the Reynolds number is 4200 (turbulent wake).

Figure 3.1 shows the schematic diagram of computational domain and boundary conditions. The computational domain size is [-15D,20D] × [-25D,25D] × [0,3D], where the center of a circular cylinder is initially located at $(x, y) = (0, 0)$. Gsell *et al.* (2016) showed that there is little difference between the re-

sults of the spanwise domain size of $3D$ and $10D$. The number of grid points is $689 \times 897 \times 60$ in the streamwise (x), transverse (y), and spanwise (z) directions. The smallest grid spacing near the cylinder surface is $\Delta x = 0.01$ and $\Delta y = 0.00667$, and the uniform grid spacing is used in the spanwise direction ($\Delta z = 0.05$). The Dirichlet boundary condition ($u = U, v = w = 0$) is applied at the inlet. At the lateral sides, the Dirichlet ($v = 0$) and Neumann ($\partial u/\partial y = \partial w/\partial y = 0$) boundary conditions are imposed. A convective boundary condition ($\partial u_i/\partial t + u_c \partial u_i/\partial x = 0$) is used at the outlet boundary, where u_c is the streamwise velocity averaged over the outflow boundary. The computations are conducted at the maximum CFL number of 1 for weak coupling with $\xi = 1$ (equation (2.18)) and $\chi = 0$ (equations (2.14), (2.16) and (2.17)).

3.1.3 Vortex-induced vibration of an elastically mounted rigid circular cylinder at the super-upper branch

Figure 3.2 shows the time histories of the transverse and streamwise displacements of the center and lift and drag coefficients. The dominant frequency of the transverse displacement matches well with that of the lift coefficient but frequencies higher than the dominant frequency are observed in the lift coefficient. The phase difference between the transverse displacement and lift coefficient is almost zero. On the other hand, the phase difference between the streamwise displacement and drag coefficient is almost 180° although the dominant frequency of the streamwise displacement matches well with that of the drag coefficient. The transverse displacement amplitude of the present simulation ($A_Y = 1.19D$) agrees well with that of previous studies (Jauvtis & Williamson, 2004; Blevins & Coughran, 2009; Gsell *et al.*, 2016; Kang *et al.*, 2017) but is larger than that of Zhao *et al.* (2012) (figure 3.3 (a)). The streamwise displace-

ment amplitude of the present simulation is larger than that of previous studies (Jauvtis & Williamson, 2004; Zhao *et al.*, 2012; Gsell *et al.*, 2016) (figure 3.3 (b)). The dominant frequency of the transverse displacement of the present simulation ($f_Y D/U = 0.74$) agrees well with that of Gsell *et al.* (2016) but is lower than that of previous studies (Jauvtis & Williamson, 2004; Zhao *et al.*, 2012; Kang *et al.*, 2017) (figure 3.4 (a)). These differences may be originated from the differences of m^* and ζ ($(m^*, \zeta) = (2, 0)$ (present study), $(2.6, 0.0036)$ (Jauvtis & Williamson, 2004), $(1.5, 0)$ (Zhao *et al.*, 2012), (2.55, 0) (Gsell *et al.*, 2016), (2.6, 0.005) (Kang *et al.*, 2017)). However, the super-upper branch is observed in the present and previous studies (Jauvtis & Williamson, 2004; Blevins & Coughran, 2009; Zhao *et al.*, 2012; Gsell *et al.*, 2016; Kang *et al.*, 2017) due to the low mass ratio, low damping ratio, and two degrees of freedom. On the other hand, in the present simulation, the dominant frequency of the streamwise displacement ($f_X D/U = 1.48$) is two times that of the transverse displacement. The phase difference between the streamwise and transverse displacements is defined as $\theta_{dis} = \phi_X - 2\phi_Y$, where ϕ_X and ϕ_Y are the instantaneous phases of the streamwise and transverse displacements (Gsell *et al.*, 2016). The time-averaged value of θ_{dis} for the present simulation ($\bar{\theta}_{dis} = 287°$) is slightly higher than that of previous studies (Jauvtis & Williamson, 2004; Gsell *et al.*, 2016) (figure 3.4 (b)).

Figure 3.5 (a) shows the trajectory of the center of an elastically mounted rigid circular cylinder. The trajectory is similar to a crescent shape because the ratio of the frequency of the streamwise displacement to that of the transverse displacement is 2 and the time averaged value of the phase difference between the streamwise and transverse displacements is 287°. The contours of the instantaneous spanwise vorticity and pressure and instantaneous velocity vector fields at $z = 0$ are shown in figure 3.5 (c) during the half cycle from the maxi-

mum to minimum transverse displacement. Arrows at the center of the circular cylinder indicate the velocity of the circular cylinder and arrows with the magnitude of U are given at the bottom left of each contour. At $tU/D = 56.73$ (①), the transverse and streamwise displacements are near the maximum (figure 3.5 (b)), and two counter-rotating starting vortices generated from the front and rear sides are located on the lower side (see pink arrows in figure 3.5 (c) ①) due to the movement of the circular cylinder in the downstream and upward directions. These counter rotating vortices induce strong impingement on the lower side of the circular cylinder. This impingement increases the pressure there but the pressure on the upper side is low due to the flow acceleration and separation delay (see a red arrow in figure 3.5 (c) ①), which causes a very high lift coefficient. At $tU/D = 57.38$ (②), there is no further generation of starting vortices on the lower side due to the movement of the circular cylinder in the upstream and downward directions and the generated two strong counter-rotating vortices are weakened and drift downstream due to the free-stream (see pink arrows in figure 3.5 (c) ②), which decreases the lift coefficient. Instead, a shear layer starts to evolve from the upper side and wake develops in the rear side (see an orange arrow in figure 3.5 (c) ②), which increases the drag coefficient. At $tU/D = 58.31$ (③), the circular cylinder moves faster in the upstream and downward directions than that at $tU/D = 57.38$ due to the low lift force and high spring force, which generates shear layer vortices from the upper side but not from the lower side (see an orange arrow in figure 3.5 (c) ③). Instead, flow is accelerated on the lower side and flow separation occurs only on the upper side (see a red arrow in figure 3.5 (c) ③), which decreases the lift coefficient and increases the drag coefficient. At $tU/D = 59.15$ (④), a strong starting vortex is generated from the rear side and located on the upper surface of the circular cylinder (see an orange arrow in figure 3.5 (c) ④) because the circular

cylinder moves downstream and downward, which increases the lift coefficient. At $tU/D = 60.31$ (⑤), two starting vortices generated from the front and rear sides are located on the upper side and induce strong impingement on the upper side of the circular cylinder (see pink arrows in figure 3.5 (c) ⑤). This impingement increases the pressure there but the pressure on the lower side is low due to the flow acceleration (see a red arrow in figure 3.5 (c) ⑤), which decreases the lift coefficient. At $tU/D = 60.77$ (⑥), the starting vortex generated from the rear side moves downstream and away from the surface (see a pink arrow in figure 3.5 (c) ⑥), which decreases the lift coefficient.

3.1.4 Flow over the elastically mounted rigid helically twisted elliptic cylinder

The helically twisted elliptic (HTE) cylinder has an elliptic cross section which rotates clockwise along the spanwise direction (figure 3.6). The shape of the HTE cylinder is given as

$$\frac{(x\cos\theta_H + y\sin\theta_H)^2}{a_H^2} + \frac{(-x\sin\theta_H + y\cos\theta_H)^2}{b_H^2} = \frac{1}{4}, \tag{3.3}$$

$$\theta_H = \frac{\pi z}{\lambda_H}, \tag{3.4}$$

where a_H and b_H are the major and minor axes, respectively, and λ_H is the wavelength (half twisted length). The aspect ratio of elliptic cylinder is $AR_H (= a_H/b_H)$ and the characteristic length is taken to be $D = \sqrt{a_H b_H}$. Therefore, two parameters, AR_H and λ_H, determine the shape of the HTE cylinder. The parameter ranges considered are $\lambda_H/D = 2, 4$, and 8 for $AR_H = 1.3$, $\lambda_H/D = 2, 4, 8, 10$, and 12 for $AR_H = 2.0$, and $\lambda_H/D = 2, 4, 6, 8, 10, 12, 16$, and 20 for

AR_H = 2.6. The computational domain size is [-15D,20D] × [-25D,25D] × [0,λ_H]. The number of grid points in the streamwise (x) and transverse (y) is 689 × 897 for λ_H/D = 2 (AR_H = 1.3, 2.0, 2.6), 4 (AR_H = 1.3, 2.0, 2.6), 8 (AR_H = 1.3, 2.0, 2.6), and 593 × 637 for the other cases. The number of grid point in the spanwise (z) is 20λ_H for all considered cases. The smallest grid spacing near the cylinder surface is $\Delta x = 0.01$ and $\Delta y = 0.00667$, and the uniform grid spacing is used in the spanwise direction (Δz = 0.05). The reduced velocity (U^* = 6), mass ratio (m^* = 2) Reynolds number(Re = 4200), and boundary conditions for the elastically mounted HTE cylinder are the same as those for an elastically mounted rigid circular cylinder. The computations are conducted at the maximum CFL number of 1 for weak coupling with ξ = 1 (equation (2.18)) and $\chi = 0$ (equations (2.14), (2.16) and (2.17)).

Figure 3.7 shows the root mean square (rms) of the transverse displacement and lift coefficient. For AR_H = 1.3, the rms of the transverse displacement and lift coefficient is not much lower for λ_H/D = 2, 4, and 8 than for an elastically mounted rigid circular cylinder. Here, the rms of the lift coefficient is almost zero for the stationary HTE cylinder with AR_H = 1.3 and λ_H/D = 4 at Re = 3900 (Kim *et al.*, 2016). For λ_H/D = 2, 4 and 8, the rms of the transverse displacement and lift coefficient decreases as the aspect ratio increases from 1.3 to 2.6. For AR_H = 2.6 and λ_H/D = 10, the rms of the transverse displacement and lift coefficient is almost zero. Figure 3.8 shows the mean streamwise displacements and drag coefficients. For the elastically mounted rigid HTE cylinder with AR_H = 2.6 and λ_H/D = 10, the mean streamwise displacement and drag coefficient are minimum in the considered range. The mean drag coefficient of the elastically mounted rigid HTE cylinder with AR_H = 2.6 and λ_H/D = 10 is slightly higher than that of a stationary circular cylinder.

Figures 3.9 and 3.10 show the instantaneous vortical structures from the side and top views, respectively. The instantaneous vortical structures are developed much earlier and more widely for an elastically mounted rigid circular cylinder than for a stationary circular cylinder (figure 3.9 (a) and (c) and figure 3.10 (a) and (c)), which results in the increase of the mean drag and lift fluctuations. For the HTE cylinder with $AR_H = 1.3$ and $\lambda_H/D = 4$, the instantaneous vortical structures are developed closer to the cylinder and more asymmetrically in the wake for the elastically mounted rigid cylinder than for the stationary cylinder (figure 3.9 (b) and (d)). Shear layer vortices are generated much earlier for the elastically mounted rigid HTE cylinder than those for the stationary HTE cylinder (figure 3.10 (b) and (d)). These induce much higher mean drag and lift fluctuations for the elastically mounted rigid HTE cylinder than those for the stationary HTE cylinder. Instantaneous vortical structures are developed more symmetrically for the elastically mounted rigid HTE cylinder with $AR_H = 2.6$ and $\lambda_H/D = 10$ than those of the elastically mounted rigid circular and HTE cylinders with $AR_H = 1.3$ and $\lambda_H/D = 4$ (figure 3.9 (c), (d), and (e)). For the elastically mounted rigid HTE cylinder with $AR_H = 2.6$ and $\lambda_H/D = 10$, the development of the shear layer vortices is more delayed at $z = 0$ and λ_H than the other region and three-dimensional vortical structures are developed in the wake (figure 3.10 (e)). These result in lower mean drag and lift fluctuations for the elastically mounted rigid HTE cylinder with $AR_H = 2.6$ and $\lambda_H/D = 10$ than those for the elastically mounted rigid circular and HTE cylinders with $AR_H = 1.3$ and $\lambda_H/D = 4$.

Figure 3.11 shows the power spectra density. For the elastically mounted rigid circular and HTE cylinders with $AR_H = 1.3$ and $\lambda_H/D = 4$, the first harmonic component of the frequencies of the lift coefficients, transverse displacements, and transverse fluid velocities at $z = 0$ and $L_z/2$ (the circular

cylinder) or $\lambda_H/2$ (the HTE cylinder) ($x = 5D$ and $y = 0$) is matched well with each other (lock-in) and almost half of the first harmonic component of the frequencies of the drag coefficients and streamwise displacements (figure 3.11 (a) and (b)). Also, the power spectra density of the third harmonic component of the frequencies of the lift coefficients is much higher than that of the third harmonic component of the frequencies of the transverse displacements and fluid velocities. The third harmonic component of the frequencies of the lift coefficients is related with the procedure of the development of strong starting vortices from the shear layers near the cylinder (see figure 3.5). For the elastically mounted rigid HTE cylinder with $AR_H = 2.6$ and $\lambda_H/D = 10$, no strong peak is observed in the power spectra density of the lift and drag coefficients, streamwise and transverse displacements, and transverse fluid velocities at $z = 0$ and $\lambda_H/2$ ($x = 5D$ and $y = 0$), which indicates the suppression of vortex shedding and vortex-induced vibration.

Figure 3.12 shows the root mean square (rms) of the sectional lift and drag coefficients along the spanwise direction. For the elastically mounted rigid HTE cylinder with $AR_H = 2.6$ and $\lambda_H/D = 10$, the rms of the sectional lift and drag coefficients is almost zero along the spanwise direction. For an elastically mounted rigid circular cylinder, the rms of the sectional lift and drag coefficients is almost constant along the spanwise direction and much higher than for the HTE cylinder with $AR_H = 2.6$ and $\lambda_H/D = 10$. For the elastically mounted rigid HTE cylinder with $AR_H = 1.3$ and $\lambda_H/D = 4$, the rms of the sectional lift coefficient is higher at $z = 0$ and λ_H than at $z = \lambda_H/2$ due to a larger planform area but the rms of the sectional drag coefficient is higher at $z = \lambda_H/2$ than at $z = 0$ and λ_H due to a larger frontal area. Figure 3.13 shows the mean sectional lift and drag coefficients along the spanwise direction. For the elastically mounted rigid HTE cylinders with $AR_H = 2.6$ and $\lambda_H/D = 10$

and $AR_H = 1.3$ and $\lambda_H/D = 4$, the mean sectional lift coefficient is maximum near $z/\lambda_H = 0.75$ and minimum near $z/\lambda_H = 0.25$ because the angles of attack of the major axis at $z/\lambda_H = 0.75$ and 0.25 are 45° and -45°, respectively. For an elastically mounted rigid circular cylinder, the mean sectional lift coefficient is almost zero along the spanwise direction. On the other hand, for the elastically mounted rigid HTE cylinders with $AR_H = 2.6$ and $\lambda_H/D = 10$ and $AR_H = 1.3$ and $\lambda_H/D = 4$, the mean sectional drag coefficient is maximum near $z/\lambda_H = 0.5$ and minimum near $z/\lambda_H = 0$ and 1 due to a large and small frontal area, respectively. For an elastically mounted rigid circular cylinder, the mean sectional drag coefficient is almost constant along the spanwise direction. For the elastically mounted rigid HTE cylinders with $AR_H = 2.6$ and $\lambda_H/D = 10$ and $AR_H = 1.3$ and $\lambda_H/D = 4$, the variations of the mean sectional lift and drag coefficients along the spanwise direction could affect the motion of a flexible HTE cylinder.

3.2 A flexible cylinder in a linearly sheared current

3.2.1 Motivations and objectives

A long flexible circular cylinder is widely used as a catenary riser, marine cable, mooring line, etc. in ocean and offshore engineering. In the ocean, there are various types of currents such as stepped, uniform, and linearly sheared currents, and the vibration of a flexible circular cylinder is affected by an inflow condition as well as its physical and geometrical properties (Vandiver, 1993). Vandiver *et al.* (1996) classified the vibration of a flexible circular cylinder as two types in a linearly sheared flow according to the ratio of the change of velocity to average velocity ($\Delta U/U_{avg}$) and the number of potentially responding modes within the vortex-shedding frequency bandwidth resulting from a sheared

flow (N_s) (figure 3.14), where $\Delta U = U_{max} - U_{min}$, $U_{avg} = (U_{max} + U_{min})/2$, U_{max} is the maximum velocity, U_{min} is the minimum velocity, $N_s = \Delta f / f_1$, $\Delta f = \Delta U / (DU_R)$, $U_R = 5.9$, D is the diameter of a circular cylinder, and f_1 is the first mode natural frequency of a flexible circular cylinder: a single-mode response for a uniform flow, a strongly sheared flow, and a mildly sheared flow with $N_s < 3$ and a multi-mode response for a mildly sheared flow with $N_s \geq 3$, where a mildly sheared flow roughly corresponds to the region of $0.2 < \Delta U/U_{avg} < 1.4$. The root mean square response in single-mode dominated cases is usually considerably greater than the total root mean square response in the multiple-mode cases (Vandiver *et al.*, 1996; Gao *et al.*, 2017). Vibration with the maximum transverse displacement amplitude greater than $1D$ is observed for a flexible circular cylinder in a uniform flow (Newman & Karniadakis, 1997; Trim *et al.*, 2005; Song *et al.*, 2011; Wang & Xiao, 2016; Gao *et al.*, 2017; Gedikli & Dahl, 2017) and a stepped flow (Chaplin *et al.*, 2005; Huera-Huarte *et al.*, 2014). However, for a flexible circular cylinder in a sheared flow, vibration with the maximum transverse displacement amplitude greater than $1D$ is not investigated.

The transverse displacement amplitude of vibration for a flexible circular cylinder is also affected by the Reynolds number and mass ratio (the ratio of structural mass to displaced fluid mass). When the Reynolds number is increased from 100 (laminar wake) to 200 (transitional wake) in a uniform flow, the maximum transverse displacement amplitude increases from $0.67D$ to $1.05D$ (Newman & Karniadakis, 1997). On the other hand, when the mass ratio is decreased from 2.7 to 1.1 at very low damping in a stepped flow, the maximum transverse displacement amplitude increases from $1D$ to $3D$ (Huera-Huarte *et al.*, 2014). Therefore, the transverse displacement amplitude may increase as the Reynolds number increases and the mass ratio decreases.

Helical strakes successfully suppress vortex-induced vibration of a flexible circular cylinder with the moderate transverse displacement amplitude ($A_Y \leq 1D$) in laboratory experiments (Frank *et al.*, 2004; Trim *et al.*, 2005; Gao *et al.*, 2017), and reduce the root mean square of the transverse displacement for a flexible circular cylinder in field experiments (Vandiver *et al.*, 2006). However, suppression of vortex-induced vibration with very large amplitude ($A_Y > 1D$) has not been conducted for a flexible circular cylinder. Therefore, the present study will investigate the cause of very large amplitude vibration for a flexible circular cylinder and apply the optimal parameter of the HTE cylinder to a flexible cylinder for two cases of single-mode and multi-mode responses.

In this paper, computational details for flow around a flexible cylinder is given in section 3.2.2. The results of flow around a flexible circular cylinder with a multi-mode response and the flexible HTE cylinder are presented in section 3.2.3. The results of flow around a flexible circular cylinder with a single-mode response and the flexible HTE cylinder are presented in section 3.2.4.

3.2.2 Computational details

The governing equation for the motion of a flexible cylinder is given as

$$\frac{\partial^2 \zeta_i}{\partial t^2} - \omega_c^2 \frac{\partial^2 \zeta_i}{\partial z^2} + \omega_b^2 \frac{\partial^4 \zeta_i}{\partial z^4} = \frac{2C_{is}}{\pi m^*}, \tag{3.5}$$

where $\zeta_i = (\zeta_x, \zeta_y)$, $C_{is} = (C_{Ds}, C_{Ls})$, $\omega_c = \sqrt{T_c/m_{cs}U_{max}^2}$, $\omega_b = \sqrt{E_s I_c/m_{cs}U_{max}^2 D^2}$, and $m^* = 4m_{cs}/\pi\rho_f D^2$. Here, $\zeta_x = \zeta_x(z,t)$ and $\zeta_y = \zeta_y(z,t)$ are the streamwise and transverse displacements of the center, respectively, $C_{Ds} = C_{Ds}(z,t)$ is the sectional drag coefficient, $C_{Ls} = C_{Ls}(z,t)$ is the sectional lift coefficient, T_c is the tension, E_s is the Young's modulus, I_c is the area moment of inertia, m_{cs} is the cylinder mass per unit length, and ρ_f is the fluid den-

sity. For a circular cylinder, $I_c = \pi D^4/64$. However, for the HTE cylinder, $I_c = I_{cx}$ in the streamwise direction, $I_c = I_{cy}$ in the transverse direction, $I_{cx} = I_{cxx}\cos^2\theta_H + I_{cyy}\sin^2\theta_H$, $I_{cy} = I_{cxx}\sin^2\theta_H + I_{cyy}\cos^2\theta_H$, $\theta_H = \pi z/\lambda_H$, $I_{cxx} = \pi D^4/64AR_H$, and $I_{cyy} = \pi D^4 AR_H/64$.

Figure 3.15 shows the schematic diagram of computational domain and boundary conditions. The ends of a flexible cylinder are pinned. On the inlet, a linearly sheared flow is imposed from $z = 0$ ($u = U_{max}$) to $0.92L_z$ ($u = U_{min}$) and the third order polynomial is given from $z = 0.92L_z$ ($u = U_{min}$) to L_z ($u = U_{max}$) (buffer region) to apply periodic boundary condition on the top and bottom sides (Bourguet *et al.*, 2011). On the lateral sides, the Dirichlet ($v = 0$) and Neumann ($\partial u/\partial y = \partial w/\partial y = 0$) boundary conditions are imposed. On the exit, a convective boundary condition ($\partial u_i/\partial t + u_c \partial u_i/\partial x = 0$) is used, where u_c is the streamwise velocity averaged over the outflow boundary.

A second-order implicit generalized-α method (Chung & Hulbert, 1993) is applied to equation (3.5):

$$\begin{aligned}
&(1-\alpha_m)\frac{\partial^2 \zeta_i^n}{\partial t^2} + \alpha_m \frac{\partial^2 \zeta_i^{n-1}}{\partial t^2} \\
&= (1-\alpha_f)\left(\omega_c^2 \frac{\partial^2 \zeta_i^n}{\partial z^2} - \omega_b^2 \frac{\partial^4 \zeta_i^n}{\partial z^4} + \frac{2C_{is}^n}{\pi m^*}\right) + \alpha_f \left(\omega_c^2 \frac{\partial^2 \zeta_i^{n-1}}{\partial z^2} - \omega_b^2 \frac{\partial^4 \zeta_i^{n-1}}{\partial z^4} + \frac{2C_{is}^{n-1}}{\pi m^*}\right),
\end{aligned} \tag{3.6}$$

$$\zeta_i^n = \zeta_i^{n-1} + \Delta t \frac{\partial \zeta_i^{n-1}}{\partial t} + \Delta t^2 \left[(0.5-\beta)\frac{\partial^2 \zeta_i{}^{n-1}}{\partial t^2} + \beta \frac{\partial^2 \zeta_i{}^n}{\partial t^2}\right], \tag{3.7}$$

$$\frac{\partial \zeta_i^n}{\partial t} = \frac{\partial \zeta_i^{n-1}}{\partial t} + \Delta t \left[(1-\gamma)\frac{\partial^2 \zeta_i{}^{n-1}}{\partial t^2} + \gamma \frac{\partial^2 \zeta_i{}^n}{\partial t^2}\right], \tag{3.8}$$

where $\alpha_m = (2\chi - 1)/(\chi + 1)$, $\alpha_f = \chi/(\chi + 1)$, $\beta = 0.25(1 - \alpha_m + \alpha_f)^2$, $\gamma = 0.5 - \alpha_m + \alpha_f$, and $\chi \in [0, 1]$ is the user-specified value. Weak coupling presented

in the section 2.2.2 is used to couple the governing equations of fluid (equations (2.3)–(2.6)) and a flexible cylinder (equations (3.6)–(3.8)) together with velocity and displacement predictors (equations (2.18)–(2.19)). The computations are conducted at the maximum CFL number of 1 for weak coupling with $\xi = 1$ (equation (2.18)) and $\chi = 0$ (equations (3.6), (3.7) and (3.8)).

3.2.3 Multi-mode response of a flexible circular cylinder and its control

Flow around a flexible circular cylinder is simulated to compare the results of the present study with those of Bourguet *et al.* (2011). The ratio of a length (L_c) to a diameter (D) is 200, the Reynolds number based on the maximum velocity is 330, the ratio of the maximum to minimum velocity is 3.67, $m^* = 7.64$, $\omega_c = 4.55$, and $\omega_b = 9.09$. Also, the results of the present study with the buffer region are compared with those of the present study without the buffer region to investigate the effects of the buffer region on vortex-induced vibration. For the present study without the buffer region, the Dirichlet boundary condition is imposed on the top ($u = U_{max}$, $v = w = 0$) and bottom sides ($u = 0.768U_{min}$, $v = w = 0$). Figure 3.16 shows the mean streamwise displacement and root mean square of transverse displacement along the spanwise direction for a flexible circular cylinder. The results of the present study with the buffer region agree well with those of Bourguet *et al.* (2011) and the present study without the buffer region.

Figure 3.17 shows the time histories of the transverse displacement along the spanwise direction for flexible cylinders. For the circular and HTE cylinders with $AR_H = 1.3$ and $\lambda_H/D = 4$, standing and traveling waves are both observed, and the traveling waves mainly propagate from the high velocity re-

gion to the low velocity region. However, the transverse displacement is almost zero for the HTE cylinder with $AR_H = 2.6$ and $\lambda_H/D = 10$. Figure 3.18 shows the time histories of the streamwise displacement along the spanwise direction. The maximum streanwise displacement is smaller for the flexible HTE cylinder with $AR_H = 2.6$ and $\lambda_H/D = 10$ than for the flexible circular and HTE cylinders with $AR_H = 1.3$ and $\lambda_H/D = 4$. Figure 3.19 shows the time histories of the streamwise displacement fluctuation along the spanwise direction for flexible cylinders. For the circular cylinder, the streamwise displacement fluctuates severely at low frequencies but rarely at high frequencies. For the HTE cylinders with $AR_H = 1.3$ and $\lambda_H/D = 4$ and $AR_H = 2.6$ and $\lambda_H/D = 10$, the streamwise displacement fluctuates more weakly than that for the circular cylinder.

Figure 3.20 shows the mean streamwise displacement and sectional drag coefficient along the spanwise direction for flexible cylinders. The maximum streamwise displacement for the HTE cylinder with $AR_H = 2.6$ and $\lambda_H/D = 10$ is lower about 17.3% than that for the circular cylinder. However, the maximum streamwise displacement for the HTE cylinder with $AR_H = 1.3$ and $\lambda_H/D = 4$ is lower about 3.6% than that for the circular cylinder. The mean sectional drag coefficient decreases from the high velocity region to the low velocity region for the circular cylinder. For the HTE cylinder with $AR_H = 1.3$ and $\lambda_H/D = 4$, the mean sectional drag coefficient varies periodically along the spanwise direction due to the rotation of the elliptic cross section along the spanwise direction. Periodic variations of the mean sectional drag coefficient along the spanwise direction are more severe for the HTE cylinder with $AR_H = 2.6$ and $\lambda_H/D = 10$ than for the HTE cylinder with $AR_H = 1.3$ and $\lambda_H/D = 4$ due to the large aspect ratio. Figure 3.21 shows the root mean square (rms) of the transverse displacement and sectional lift coefficient along the spanwise

direction for flexible cylinders. The rms of the transverse displacement and sectional lift coefficient is much smaller for the HTE cylinder with $AR_H = 2.6$ and $\lambda_H/D = 10$ than for the circular cylinder. On the other hand, the rms of the transverse displacement and sectional lift coefficient for the HTE cylinder with $AR_H = 1.3$ and $\lambda_H/D = 4$ is similar to that for the circular cylinder. For the circular and HTE cylinders with $AR_H = 1.3$ and $\lambda_H/D = 4$, the rms of the transverse displacement varies periodically along the spanwise direction due to the standing waves. On the other hand, the traveling waves increase the rms of the transverse displacement.

Figure 3.22 shows the instantaneous vortical structures around flexible cylinders from the side and top views. For the circular cylinder, vortex rollers are distorted along the spanwise direction and three-dimensional vortical structures are more dominant in the high velocity region than in the low velocity region. Cells of vortex shedding are formed along the spanwise direction due to the deflection of the circular cylinder and linearly sheared inflow. For the HTE cylinder with $AR_H = 1.3$ and $\lambda_H/D = 4$, vortical structures are three-dimensional but not weakened compared to those for the circular cylinder. For the HTE cylinder with $AR_H = 2.6$ and $\lambda_H/D = 10$, three-dimensional vortical structures are observed behind the cross section with the major axis perpendicular to the free-stream but not observed behind the cross section with the major axis parallel with the free-stream, which results in low mean streamwise displacement and rms of the transverse displacement.

Figure 3.23 shows the contours of the instantaneous spanwise vorticity around a flexible circular cylinder. Two single vortices shed per cycle (2S mode) near the circular cylinder at $z/D = 7$, 50, and 149 but a distinct pair of co-ratating vortices of the same sign (2C mode) is observed in the further downstream at $z/D = 149$ (Jauvtis & Williamson, 2004; Bourguet *et al.*, 2011), which induce

the vibration of a flexible circular cylinder. Figure 3.24 shows the contours of the instantaneous spanwise vorticity around the flexible HTE cylinder with $AR_H = 1.3$ and $\lambda_H/D = 4$. Two single vortices shed per cycle (2S mode) near the HTE cylinder at $z/D = 6$, 8, 50, 52, 150, and 152, which induces the vibration of the HTE cylinder. Figure 3.25 shows the contours of the instantaneous spanwise vorticity around the flexible HTE cylinder with $AR_H = 2.6$ and $\lambda_H/D = 10$. At the cross section with the major axis perpendicular to the free-stream ($z/D = 5$, 45, and 145), the development of vortex shedding is greatly delayed. At the cross section with the major axis parallel with the free-stream ($z/D = 10$, 50, and 150), vortex shedding is not developed and the width of wake region is much narrower than that at the cross section with the major axis perpendicular to the free-stream.

Figure 3.26 shows the power spectra density of the transverse displacement, sectional lift coefficient, and transverse fluid velocity at $x/D = 20$ and $y/D = 0$ for flexible cylinders. For the circular cylinder, the frequencies of 0.148, 0.162 and 0.174 are dominant over the entire span for the transverse displacement and sectional lift coefficient. For the transverse fluid velocity at $x/D = 20$ and $y/D = 0$, the frequencies of 0.148, 0.162 and 0.174 are dominant over $z/D = 0 \sim 75$ but dominant frequencies in the range of $z/D = 75 \sim 200$ decrease along the spanwise direction due to the linearly sheared inflow. Lock-in occurs in the range of $z/D = 0 \sim 75$ for the circular cylinder, which induces traveling waves from the high velocity region to the low velocity region. For the HTE cylinder with $AR_H = 1.3$ and $\lambda_H/D = 4$, the frequencies of 0.122, 0.135 and 0.147 are dominant over the entire span for the transverse displacement and sectional lift coefficient. For the transverse fluid velocity at $x/D = 20$ and $y/D = 0$, the frequencies of 0.122, 0.135 and 0.147 are dominant over $z/D = 0 \sim 80$ but dominant frequencies in the range of $z/D = 80 \sim 200$

decrease along the spanwise direction due to the linearly sheared inflow. Lock-in occurs in the range of $z/D = 0 \sim 80$ for the HTE cylinder. The lock-in region is slightly larger for the HTE cylinder than for the circular cylinder because the dominant frequencies in the lock-region are lower for the HTE cylinder than for the circular cylinder. On the other hand, dominant frequencies are not observed for the HTE cylinder with $AR_H = 2.6$ and $\lambda_H/D = 10$ because vortex-induced vibration is completely suppressed.

Figure 3.27 shows the spanwise evolution of selected temporal mode phase angles for flexible cylinders. Phase angles are obtained by using Fourier series (Lucor *et al.*, 2006; Bourguet *et al.*, 2011):

$$\zeta_y(z,t) \approx \sum_{q=-N/2}^{N/2} a_q^y(z) \exp\left[2\pi i f_q t\right] = \sum_{q=-N/2}^{N/2} \left|a_q^y\right|(z) \exp\left[i\left(2\pi f_q t + \psi_q^y(z)\right)\right], \tag{3.9}$$

where $f_q = q/T_s$ is the frequency associated with the qth mode, T_s is the sampling period, a_q^y is the complex modal coefficient, and ψ_q^y is the spatial phase angle. For the circular cylinder, spatial phase angles for the three dominant frequencies decrease along the spanwise direction, which indicates that traveling waves propagate from the high velocity region to the low velocity region. On the other hand, for the HTE cylinder with $AR_H = 1.3$ and $\lambda_H/D = 4$, the spatial phase angles corresponding to the dominant frequencies of 0.137 and 0.147 decrease along the spanwise direction. However, the spatial phase angle corresponding to the dominant frequency of 0.123 increases from $z/D = 0$ to 60 and decrease from $z/D = 80$ to 180 because lock-in occurs in the relatively lower velocity region for the frequency of 0.123 than for the frequencies of 0.137 and 0.147.

Figure 3.28 (a) shows the schematic diagram of a partial HTE cylinder with $AR_H = 2.6$ and $\lambda_H/D = 10$. A partial HTE cylinder is composed of the HTE cylinder from $z/D = 0$ to 80 and a circular circular from $z/D = 90$ to 190. In the transition region ($z/D = 80 \sim 90$ and $190 \sim 200$), the major and minor axes linearly change from the HTE cylinder to a circular cylinder and vice versa. For the region of the flexible HTE cylinder, three dimensional vortical structures are developed behind the cross section with the major axis perpendicular to the free-stream but significantly weakened behind the cross-section with the major axis parallel with the free-stream (figure 3.28 (b) and (c)). However, two-dimensional vortex rollers are distorted along the spanwise direction in the region of a flexible circular cylinder (figure 3.28 (b)).

Figure 3.29 shows the time histories of the streamwise displacement, streamwise displacement fluctuation, and transverse displacement along the spanwise direction for the flexible partial HTE cylinder with $AR_H = 2.6$ and $\lambda_H/D = 10$. The streamwise displacement is maximum near $z/D = 80$ and fluctuates with small amplitude at low frequencies. In the transverse displacement, standing waves alternatively occur between the high and low velocity regions but the frequencies and amplitudes of standing waves are slightly lower than those for a flexible circular cylinder.

Figure 3.30 shows the mean streamwise displacement and sectional drag coefficient and root mean square of the transverse displacement and sectional lift coefficient for flexible cylinders. The maximum streamwise displacement for the partial HTE cylinder with $AR_H = 2.6$ and $\lambda_H/D = 10$ is lower by 6.5% than that for the circular cylinder but larger by 13.1% than that for the HTE cylinder with $AR_H = 2.6$ and $\lambda_H/D = 10$. For the partial HTE cylinder, the mean sectional drag coefficient periodically varies along the spanwise direction in the region of the HTE cylinder but linearly decreases along the spanwise direction in the

region of a circular cylinder. The rms of the transverse displacement is lower for the partial HTE cylinder than for the circular cylinder because traveling waves are weakened. The differences between local minima and maxima of the rms of the transverse displacement are not much reduced for the partial HTE cylinder compared to the circular cylinder because standing waves are intermittently generated. The rms of the sectional lift coefficient is much reduced for the partial HTE cylinder compared to the circular cylinder.

Figure 3.31 $(a) - (c)$ shows the power spectra density of the transverse displacement, sectional lift coefficient and transverse fluid velocity at $x/D = 20$ and $y/D = 0$ for the flexible partial HTE cylinder with $AR_H = 2.6$ and $\lambda_H/D = 10$. For the transverse displacement and sectional lift coefficient, the frequencies of 0.110, 0.100, and 0.095 are dominant over the entire span. However, for the transverse fluid velocities, the power spectra density is negligible from $z/D = 0$ to 80, the frequencies of 0.110, 0.100, and 0.095 are dominant in the narrow region of the span near $z/D = 100$, and dominant frequencies decrease from $z/D = 120$ to 200. The traveling wave with the frequency of 0.110 propagates from the low velocity region to high velocity region and the traveling waves with the frequencies of 0.100 and 0.095 propagate in both span directions (figure 3.31 (d)) because the lock-in occurs near $z/D = 100$.

3.2.4 Single-mode response of a flexible circular cylinder and its control

Large amplitude vibration is often observed in the single-mode response (Vandiver *et al.*, 1996), so parameters are selected based on the regime classified by Vandiver *et al.* (1996) to induce single-mode response. The ratio of a length (L_c) to a diameter (D) is 50, the Reynolds number based on the maximum

velocity is 4000, the ratio of the maximum to minimum velocity is 9, $m^* = 2.55$, $\omega_c = 5$, and $\omega_b = 10$. Large eddy simulation with a dynamic global subgrid-scale mode is performed (Park *et al.*, 2006; Lee *et al.*, 2010).

Figure 3.32 shows the time traces of the transverse and streamwise displacements along the spanwise direction for flexible cylinders. For the circular cylinder, single-mode response occurs together with large amplitude vibration ($A_Y/D > 2$). Also, the streamwise displacement severely fluctuates. The dominant frequency of the streamwise displacement fluctuation are about two times that of the transverse displacement fluctuation. On the other hand, the transverse and streamwise displacements rarely fluctuate for the HTE cylinder with $AR_H = 2.6$ and $\lambda_H/D = 10$. Also, the streamwise deflection of the HTE cylinder is much smaller than that of the circular cylinder.

Figure 3.33 shows the instantaneous vortical structures around flexible cylinders from the top and side views. For the circular cylinder, large amplitude vibration in the transverse direction induces wide width of the wake and complex vortical structures near the cylinder. On the other hand, the width of the wake is narrower for the HTE cylinder with $AR_H = 2.6$ and $\lambda_H/D = 10$ than for the circular cylinder due to the suppression of vortex-induced vibration. For the HTE cylinder, complex vortical structures are sustained further downstream behind the cross section with the major axis perpendicular to the free-stream but rapidly disappear behind the cross section with the major axis parallel with the free-stream.

Figure 3.34 shows the contours of the instantaneous spanwise vorticity for flexible cylinders. For the circular cylinder, flow structures at five instants are shown while the cross section at $z/D = 25$ moves from the maximum to minimum transverse displacement (figure 3.34 (a)-(e)). At $tU_{max}/D = 13.6$, shear layers are not completely evolved from the front and rear sides. At $tU_{max}/D =$

15.9, a shear layer vortex is formed from the front side and located on the upper side. At $tU_{max}/D = 18.5$, shear layer vortices are formed from front and rear sides in the upper side. At $tU_{max}/D = 21.1$, shear layer vortices generated from the front and rear sides move downstream due to the low velocity of the cross section and free-stream. At $tU_{max}/D = 23.6$, wake region moves from the upper side to rear side. Flow structures around the flexible circular cylinder with large amplitude vibration are similar to those around the elastically mounted rigid circular cylinder with the large amplitude vibration. On the other hand, for the HTE cylinder with $AR_H = 2.6$ and $\lambda_H/D = 10$, the width of wake is much narrower at the cross section with the major axis parallel with the free-steam than at the cross section with the major axis perpendicular to the free-stream. Shear layer vortices are developed from the upper and lower sides of the cross section with the major axis perpendicular to the free-stream, the lower side of the cross section with the angle of -45° between the major axis and free-stream, the upper side of the cross section with the angle of 45° but vortex shedding is observed in the wake of the cross section with the major axis parallel with the free-stream.

3.3 Summary

In the present study, we investigated the cause of large amplitude vibration of an elastically mounted rigid circular cylinder in the super-upper branch. During the downward movement of an elastically mounted rigid circular cylinder, shear layers were evolved from the front and rear sides and starting vortices were generated from the shear layers, which induced flow toward the upper side. The induced flow caused high pressure on the upper side but low pressure was induced by flow acceleration and separation delay on the lower side

due to the downward movement. During the upward movement of an elastically mounted rigid circular cylinder, high and low pressures are induced on the lower and upper sides, respectively. The significant difference between pressures on the upper and lower sides caused large amplitude vibration of an elastically mounted rigid circular cylinder.

We conducted a parametric study for an elastically mounted rigid helically twisted elliptic (HTE) cylinder to suppress vortex-induced vibration in the super-upper branch. Vortex-induced vibration was significantly suppressed at the aspect ratio of 2.6 and the wavelength of $10D$. However, the elastically mounted rigid HTE cylinder with the aspect ratio of 1.3 and the wavelength of $4D$ induced large amplitude vibration even though the stationary HTE cylinder with the aspect ratio of 1.3 and the wavelength of $4D$ completely suppressed vortex shedding (Kim *et al.*, 2016). On the other hand, the mean drag coefficient is slightly higher for the elastically mounted rigid HTE cylinder with the aspect ratio of 2.6 and the wavelength of $10D$ than for a stationary circular cylinder.

We applied the optimal parameters of stationary and elastically mounted rigid HTE cylinders to the case showing the multi-mode response of a flexible circular cylinder in a linearly sheared inflow. The flexible HTE cylinder with the aspect ratio of 2.6 and the wavelength of $10D$ successfully suppressed vortex-induced vibration but the flexible HTE cylinder with the aspect ratio of 1.3 and the wavelength of $4D$ did not suppress vortex-induced vibration. We partially replaced a flexible circular cylinder showing lock-in with the flexible HTE cylinder with the aspect ratio of 2.6 and the wavelength of $10D$ but vortex-induced vibration was not completely suppressed because lock-in moved to the region of a flexible circular cylinder and traveling waves propagated to the region of the flexible HTE cylinder.

A flexible circular cylinder showing single-mode response was vibrated with the amplitude greater than $2D$ in a strongly sheared inflow. The very large amplitude vibration of a flexible circular cylinder was induced by starting vortices in the shear layers evolved from the front and rear sides, which is similar to the process for large amplitude vibration of an elastically mounted rigid circular cylinder with . The flexible HTE cylinder with the aspect ratio of 2.6 and the wavelength of $10D$ successfully suppressed very large amplitude vortex-induced vibration and significantly reduced streamwise deflection.

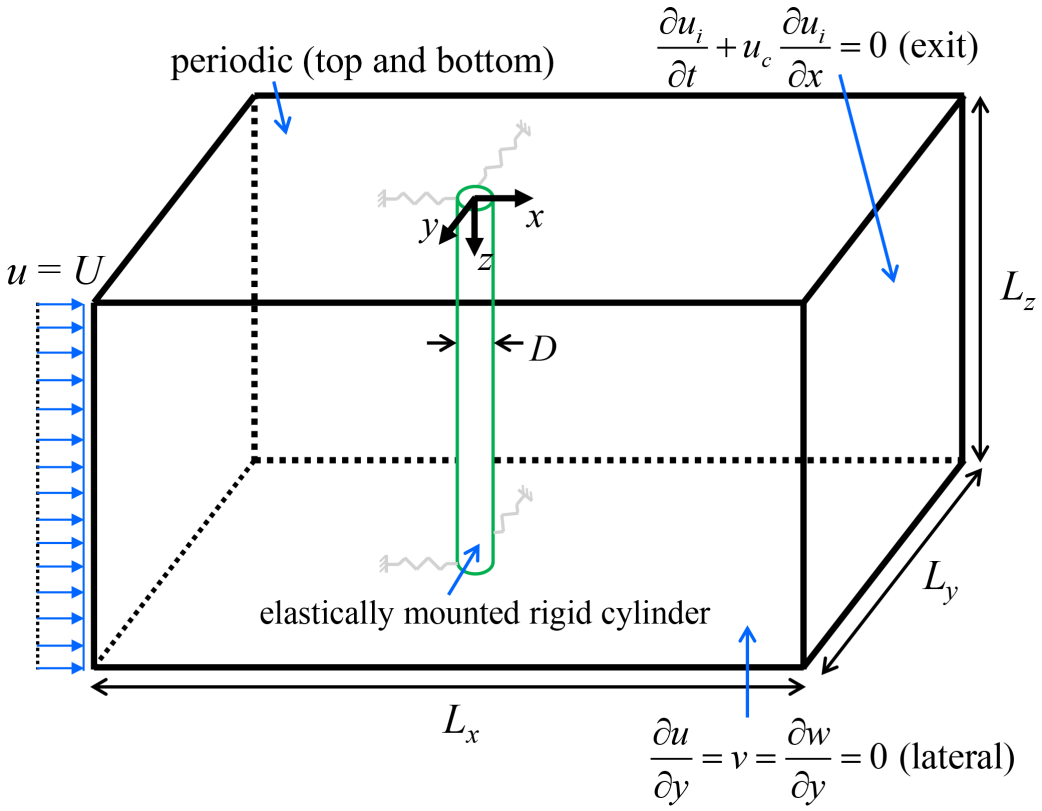

Figure 3.1. Schematic diagram of computational domain and boundary conditions for the simulation of flow around an elastically mounted rigid cylinder.

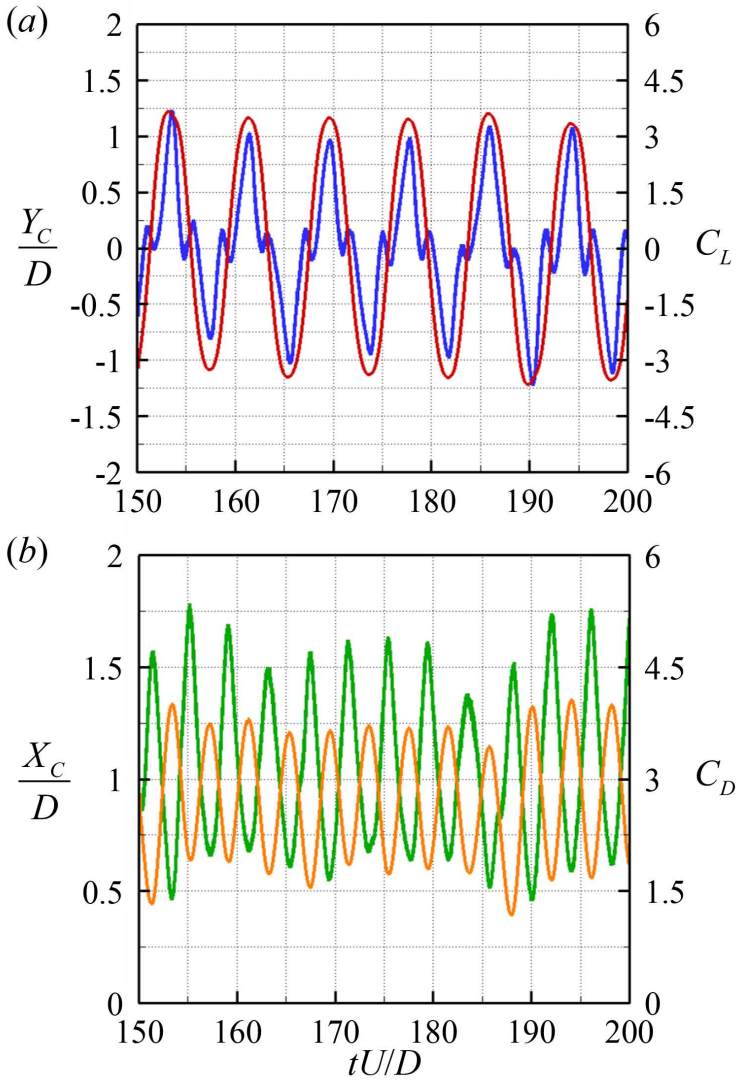

Figure 3.2. Time histories of the transverse and streamwise displacements of the center and lift and drag coefficients for an elastically mounted rigid circular cylinder at $U^* = 6$: (a) Y_C/D and C_L; (b) X_C/D and C_D. Red line, Y_C/D; blue line, C_L; orange line, X_C/D; green line, C_D.

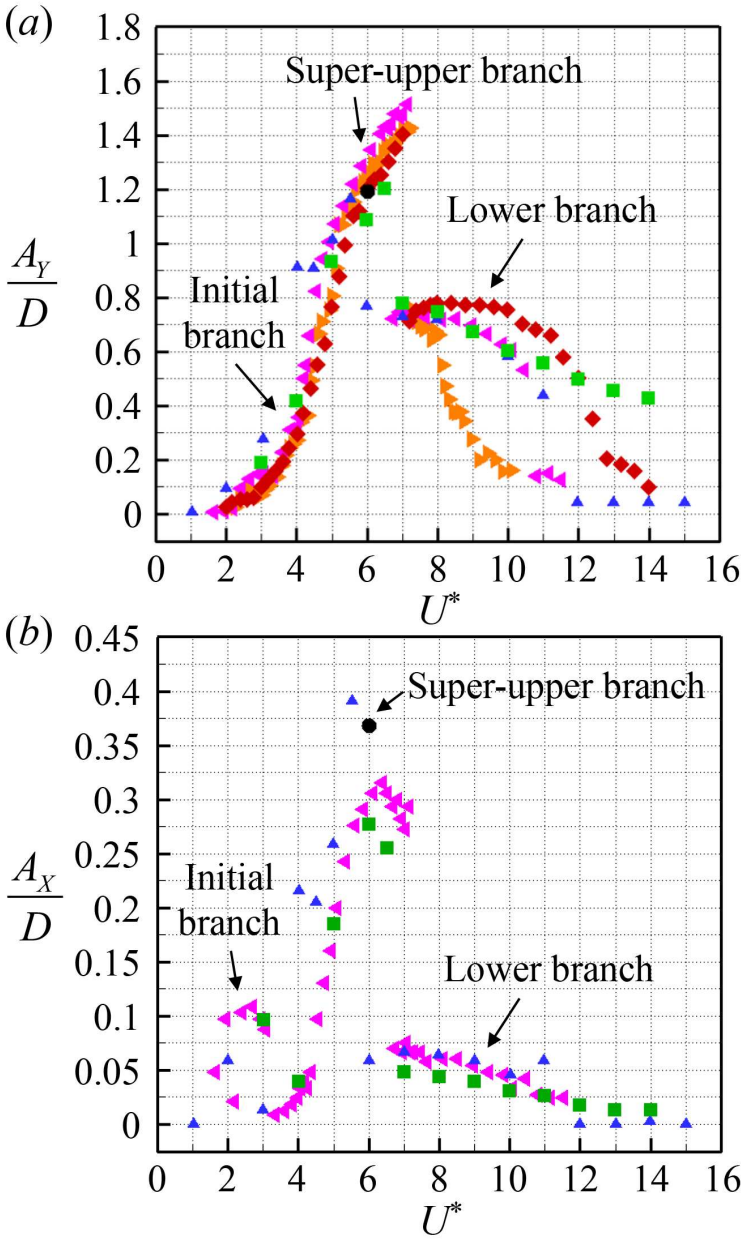

Figure 3.3. Transverse and streamwise displacement amplitudes with the reduced velocity: (*a*) A_X/D; (*b*) A_Y/D. Black circle, present simulation; pink left triangle, Jauvtis & Williamson (2004); orange right triangle, Blevins & Coughran (2009); blue delta, Zhao *et al.* (2012); green square, Gsell *et al.* (2016); red diamond, Kang *et al.* (2017).

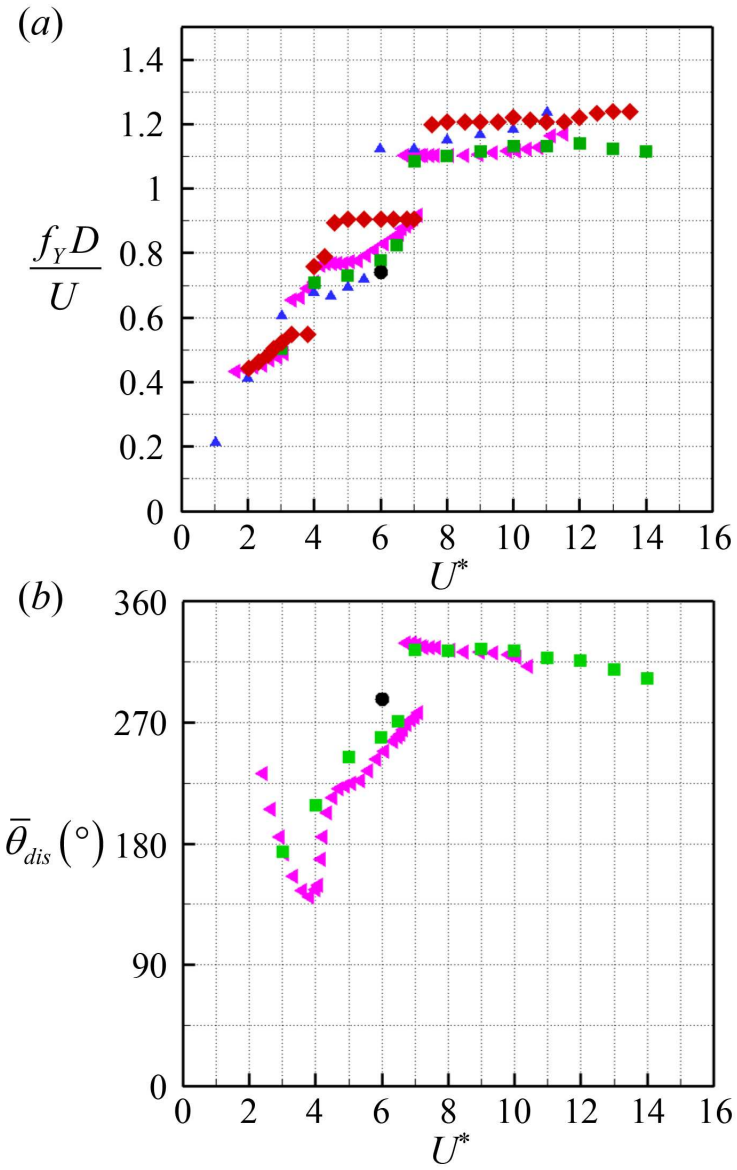

Figure 3.4. Transverse displacement frequency and time averaged phase value of the phase difference between the streamwise and transverse displacements with the reduced velocity: (a) $f_Y D/U$; (b) $\bar{\theta}_{dis}$. Black circle, present simulation; pink left triangle, Jauvtis & Williamson (2004); blue delta, Zhao *et al.* (2012); green square, Gsell *et al.* (2016); red diamond, Kang *et al.* (2017).

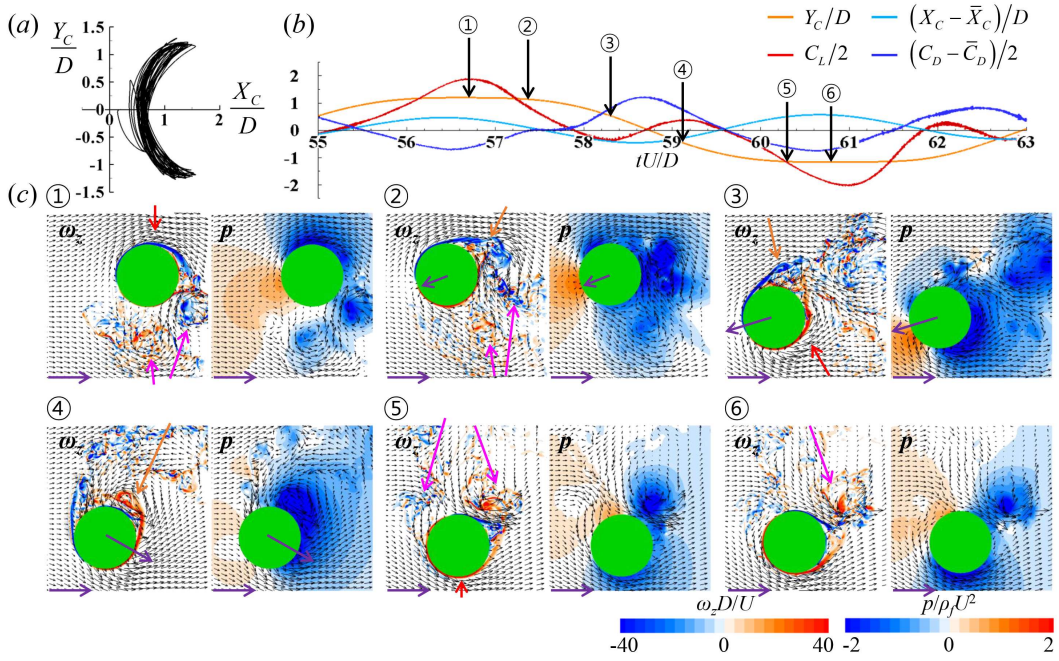

Figure 3.5. Elastically mounted rigid circular cylinder: (a) Trajectory of the center; (b) time traces of the transverse and streamwise displacements of the center and half of the lift and drag coefficients; (c) contours of the instantaneous spanwise vorticity and pressure and velocity vector fields. ① $tU/D = 56.73$; ② 57.38; ③ 58.31; ④ 59.15; ⑤ 60.31; ⑥ 60.77. Arrows at the center of the circular cylinder indicate the velocity of the circular cylinder and arrows with the magnitude of U are given at the bottom left of each contour.

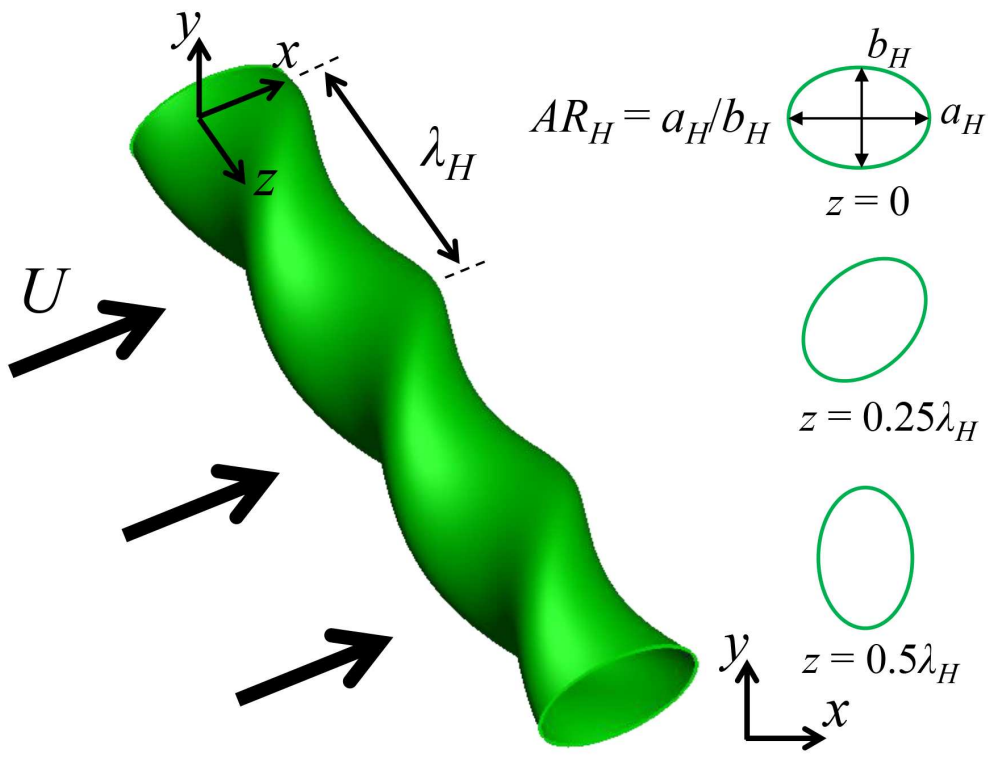

Figure 3.6. Schematic diagram of the helically twisted elliptic (HTE) cylinder.

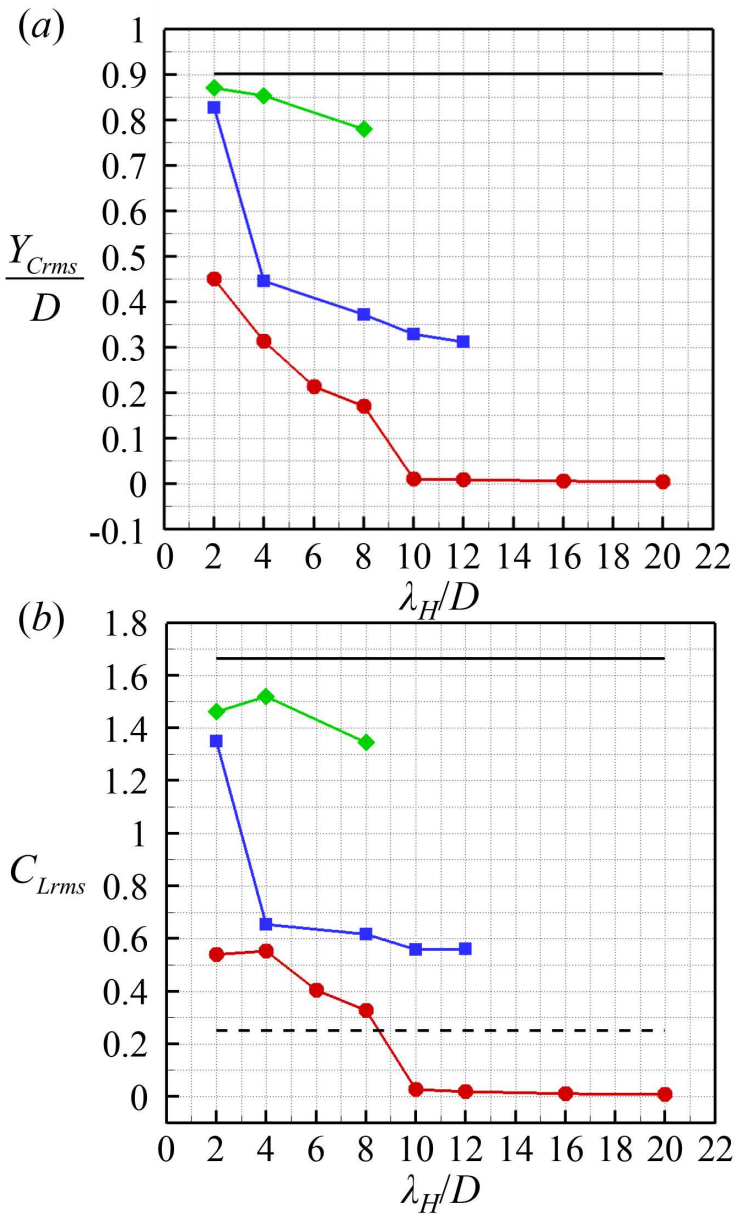

Figure 3.7. Root mean square of the transverse displacement of the center and the lift coefficient of elastically mounted rigid circular and HTE cylinders with the wavelength and aspect ratio: (a) Y_{Crms}/D; (b) C_{Lrms}. Green diamond, the HTE cylinder with the aspect ratio $(AR_H) = 1.3$; blue square, $AR_H = 2.0$; red circle, $AR_H = 2.6$; black solid line, the circular cylinder; black dashed line, a stationary circular cylinder.

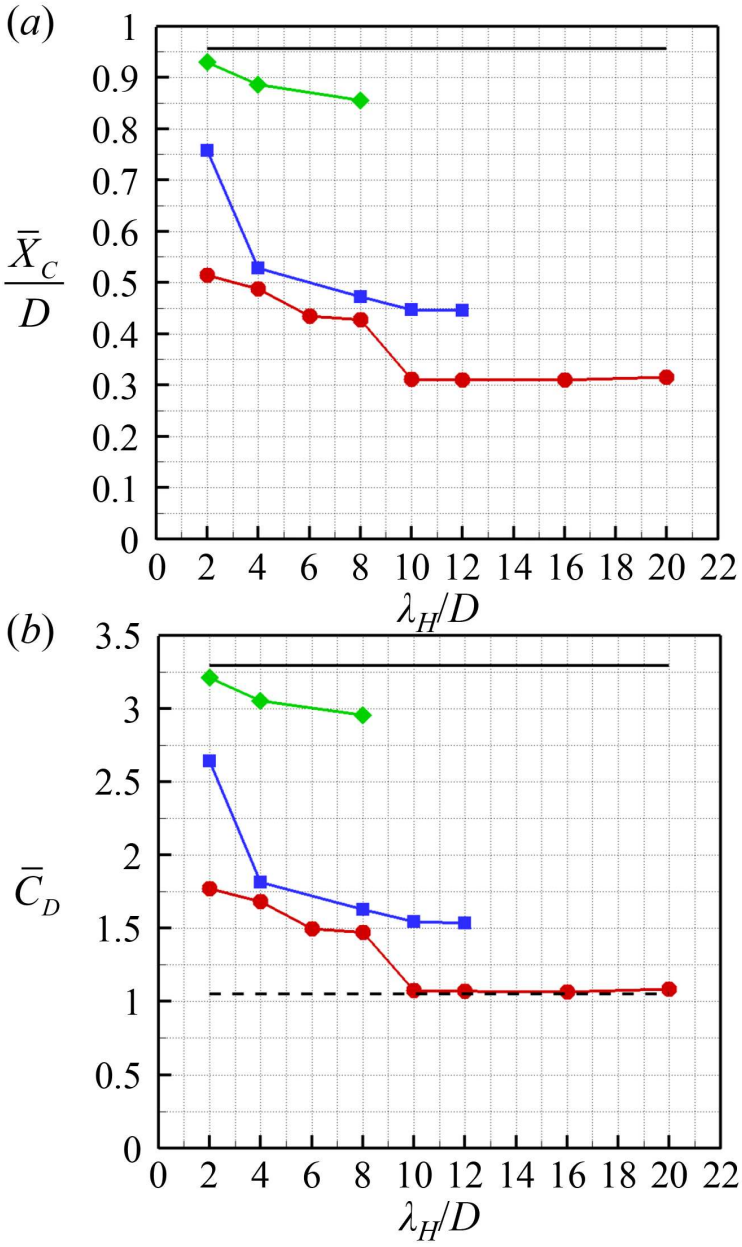

Figure 3.8. Mean streamwise displacements of the center and drag coefficients of elastically mounted rigid circular and HTE cylinders with the wavelength: (*a*) $\bar{X}_C/D$; (*b*) $\bar{C}_D$. Green diamond, the HTE cylinder with $AR_H = 1.3$; blue square, $AR_H = 2.0$; red circle, $AR_H = 2.6$; black solid line, the circular cylinder; black dashed line, a stationary circular cylinder.

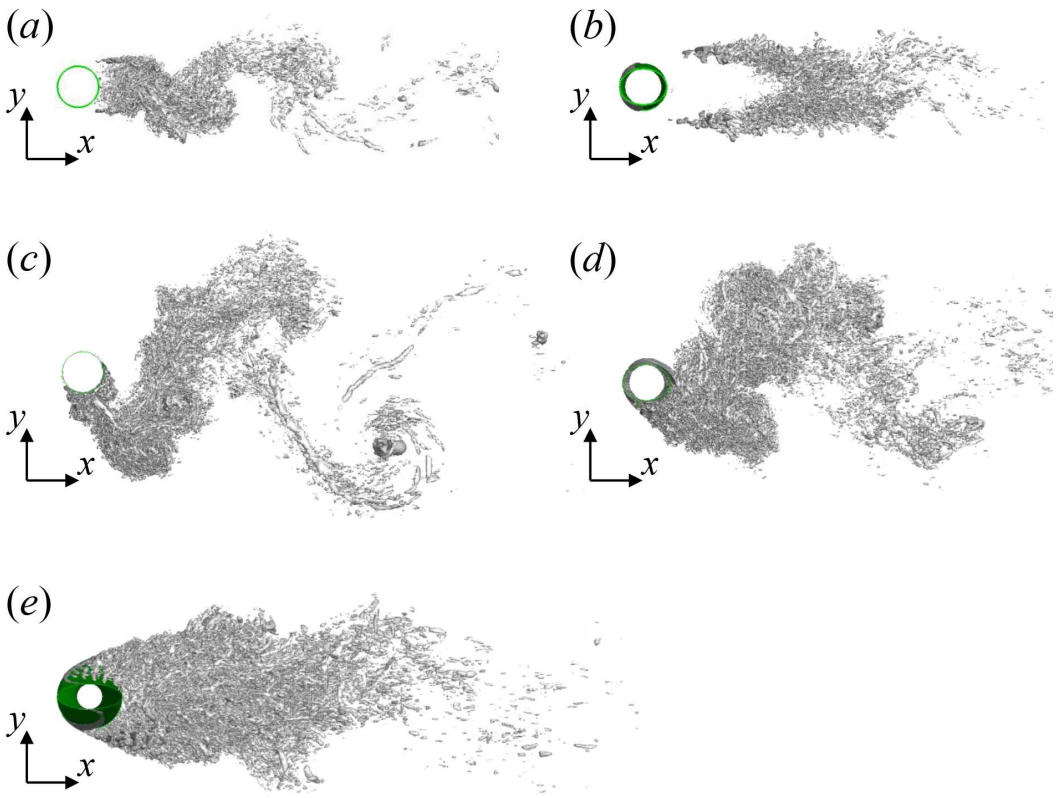

Figure 3.9. Instantaneous vortical structures around stationary cylinders ((*a*) and (*b*)) and elastically mounted rigid cylinders ((*c*)–(*e*)) from the side view: (*a*) circular cylinder; (*b*) HTE cylinder with $AR_H = 1.3$ and $\lambda_H/D = 4$; (*c*) circular cylinder; (*d*) HTE cylinder with $AR_H = 1.3$ and $\lambda_H/D = 4$; (*e*) HTE cylinder with $AR_H = 2.6$ and $\lambda_H/D = 10$.

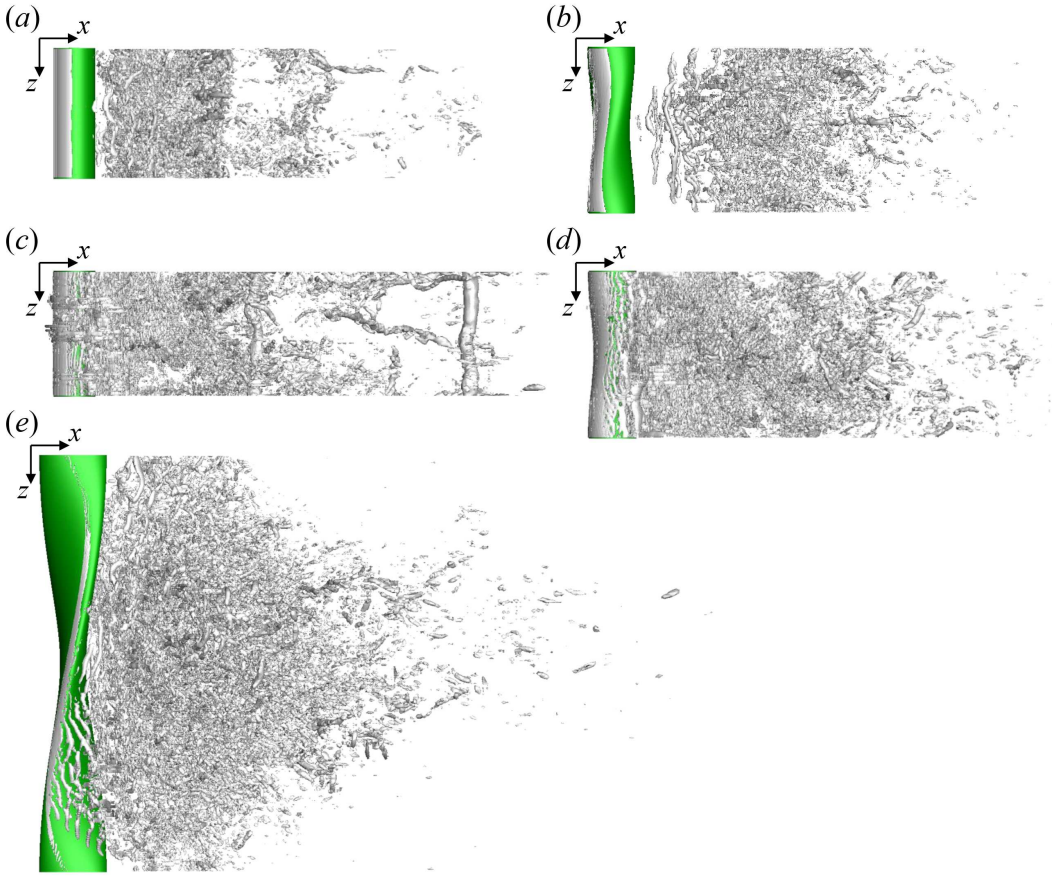

Figure 3.10. Instantaneous vortical structures around stationary cylinders ((*a*) and (*b*)) and elastically mounted rigid cylinders ((*c*)–(*e*)) from the top view: (*a*) circular cylinder; (*b*) HTE cylinder with $AR_H = 1.3$ and $\lambda_H/D = 4$; (*c*) circular cylinder; (*d*) HTE cylinder with $AR_H = 1.3$ and $\lambda_H/D = 4$; (*e*) HTE cylinder with $AR_H = 2.6$ and $\lambda_H/D = 10$.

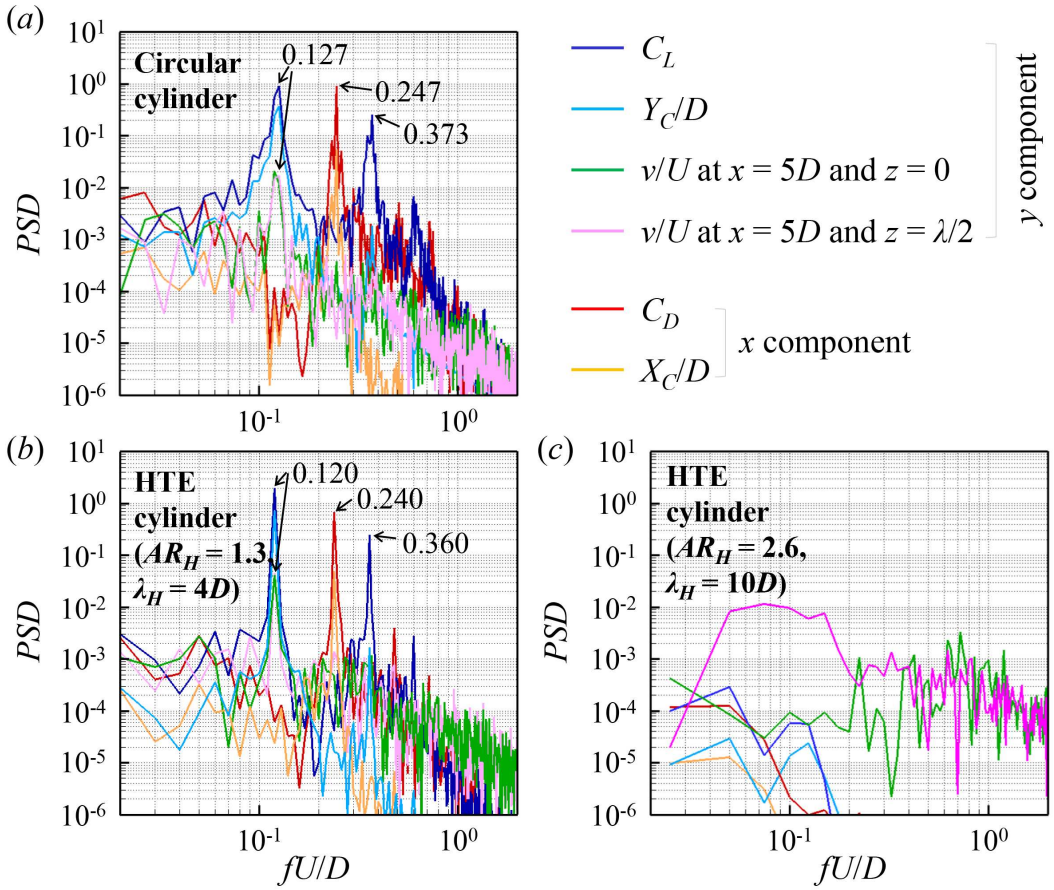

Figure 3.11. Power spectra density for an elastically mounted rigid cylinder: (a) circular cyilnder; (b) HTE cylinder with $AR_H = 1.3$ and $\lambda_H/D = 4$; (c) HTE cylinder with $AR_H = 2.6$ and $\lambda_H/D = 10$. blue line, C_L; azure line, Y_C/D; green line, v/U at $(x, y, z) = (5D, 0, 0)$; pink line, v/U at $(x, y, z) = (5D, 0, L_z/2)$ (circular) or $(5D, 0, \lambda_H/2)$ (HTE); red line, C_D; orange line, X_C/D.

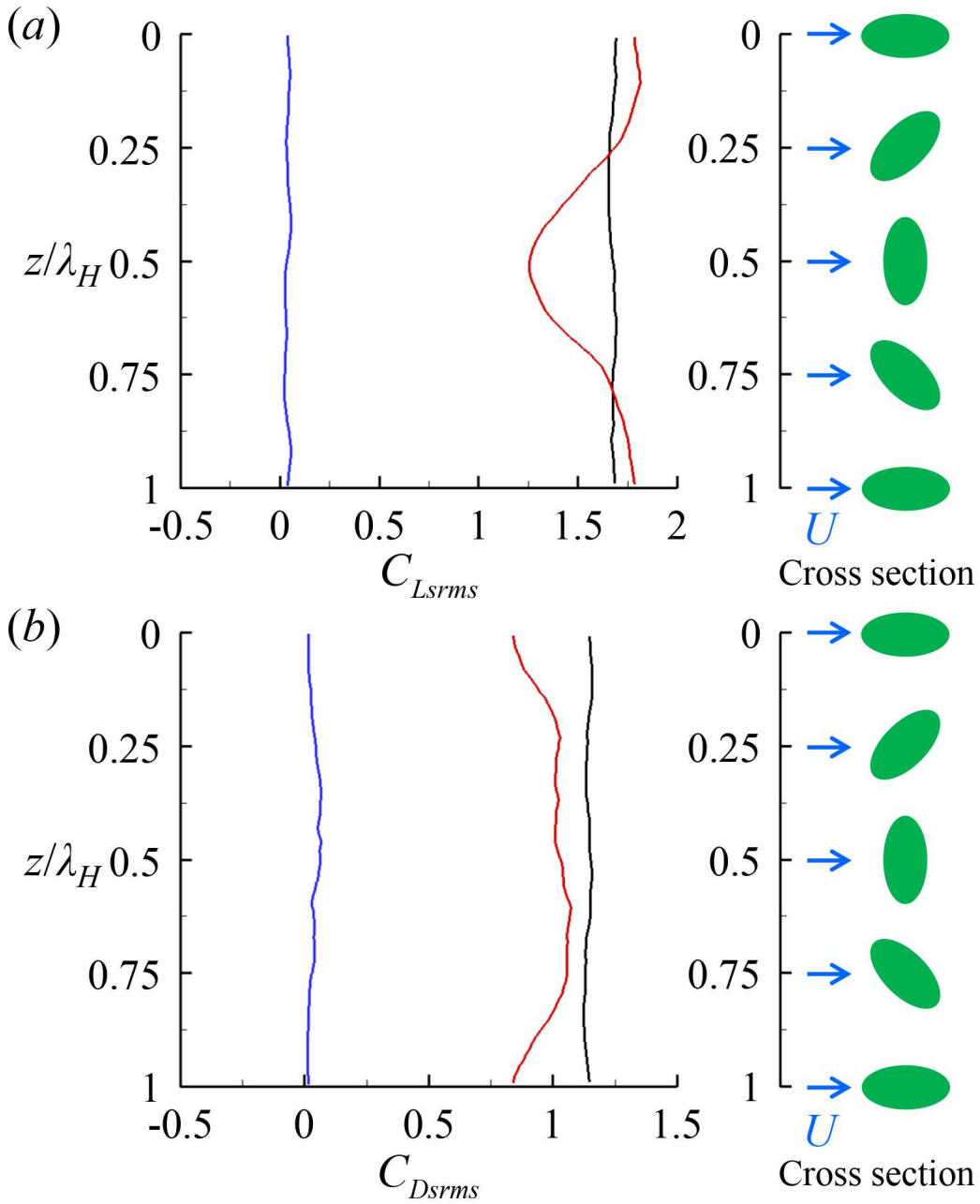

Figure 3.12. Root mean square of (a) the sectional lift and (b) drag coefficients for elastically mounted rigid cylinders. Black line, circular cylinder; red line, HTE cylinder with $AR_H = 1.3$ and $\lambda_H/D = 4$; blue line, HTE cylinder with $AR_H = 2.6$ and $\lambda_H/D = 10$.

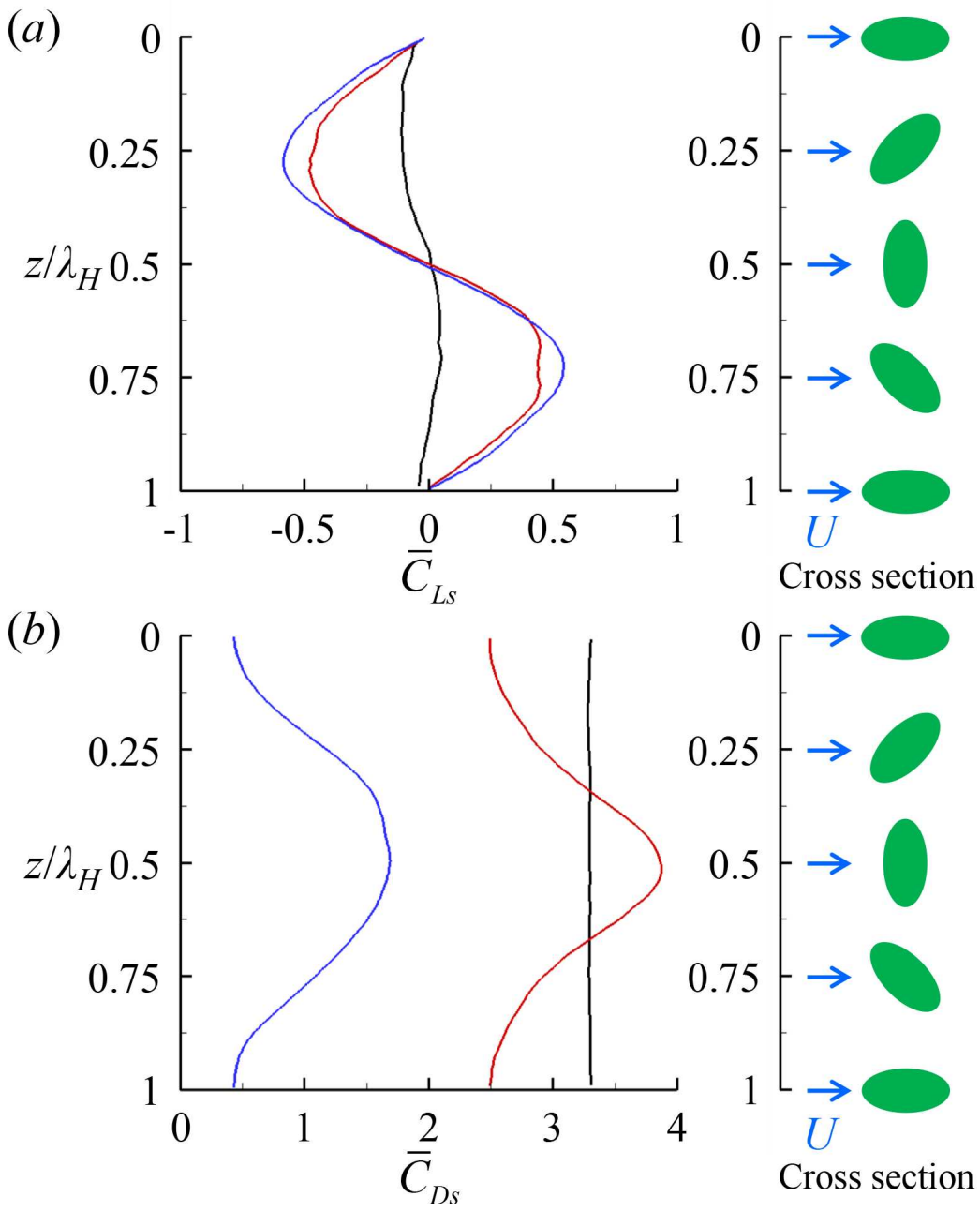

Figure 3.13. (a) Mean sectional lift and (b) drag coefficients for elastically mounted rigid cylinders. Black line, circular cylinder; red line, HTE cylinder with $AR_H = 1.3$ and $\lambda_H/D = 4$; blue line, HTE cylinder with $AR_H = 2.6$ and $\lambda_H/D = 10$.

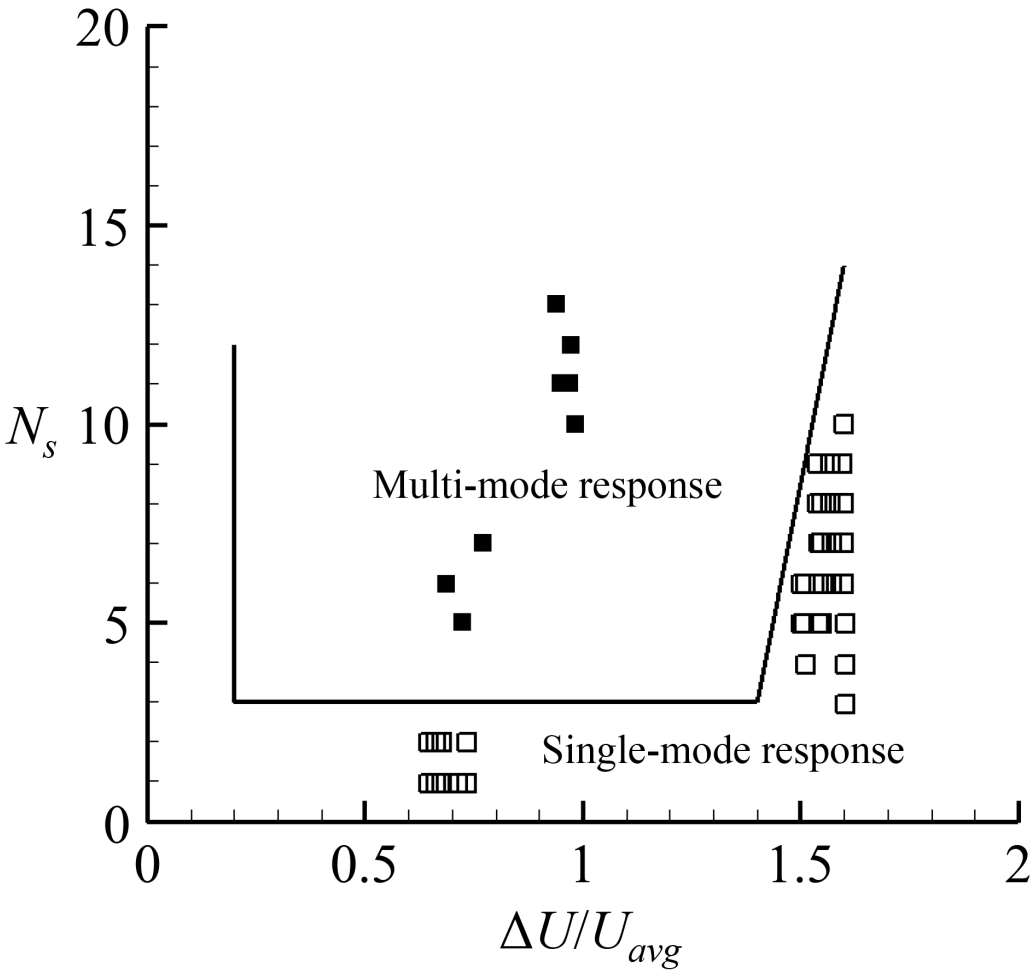

Figure 3.14. Single-mode and multi-mode response regions with the ratio of the change of velocity to average velocity ($\triangle U/U_{avg}$) and number of modes in excitation frequency band (N_s) (Vandiver *et al.*, 1996).

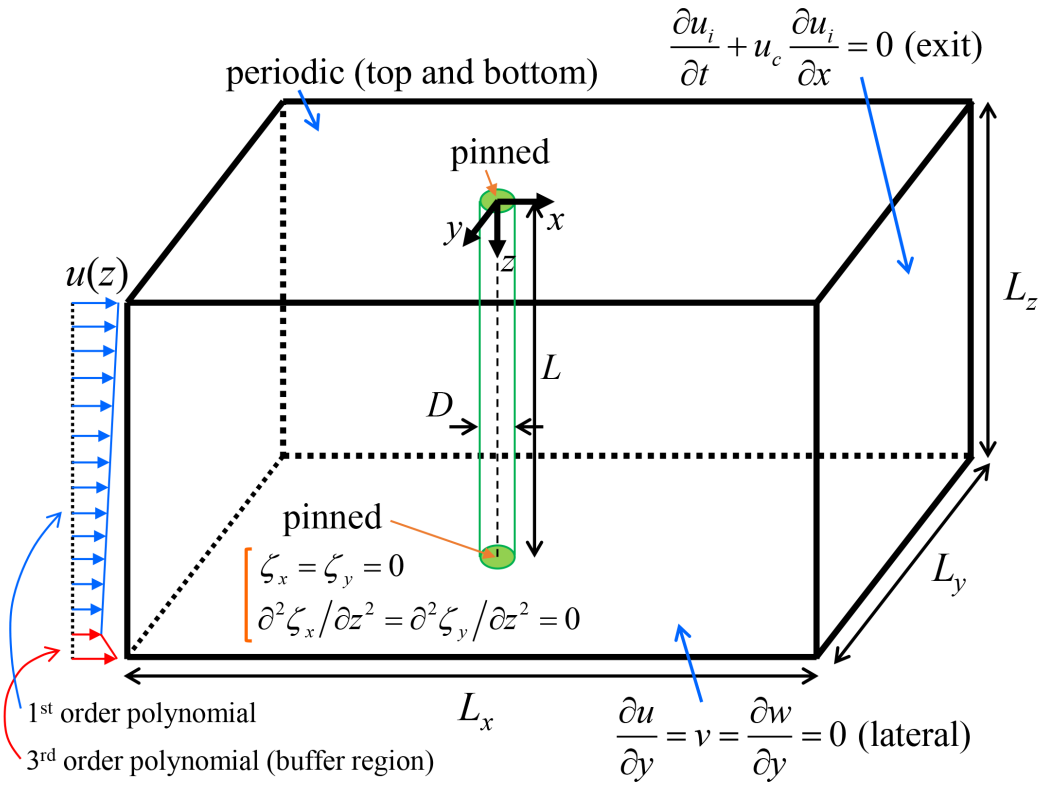

Figure 3.15. Schematic diagram of computational domain and boundary conditions for the simulation of flow around a flexible cylinder.

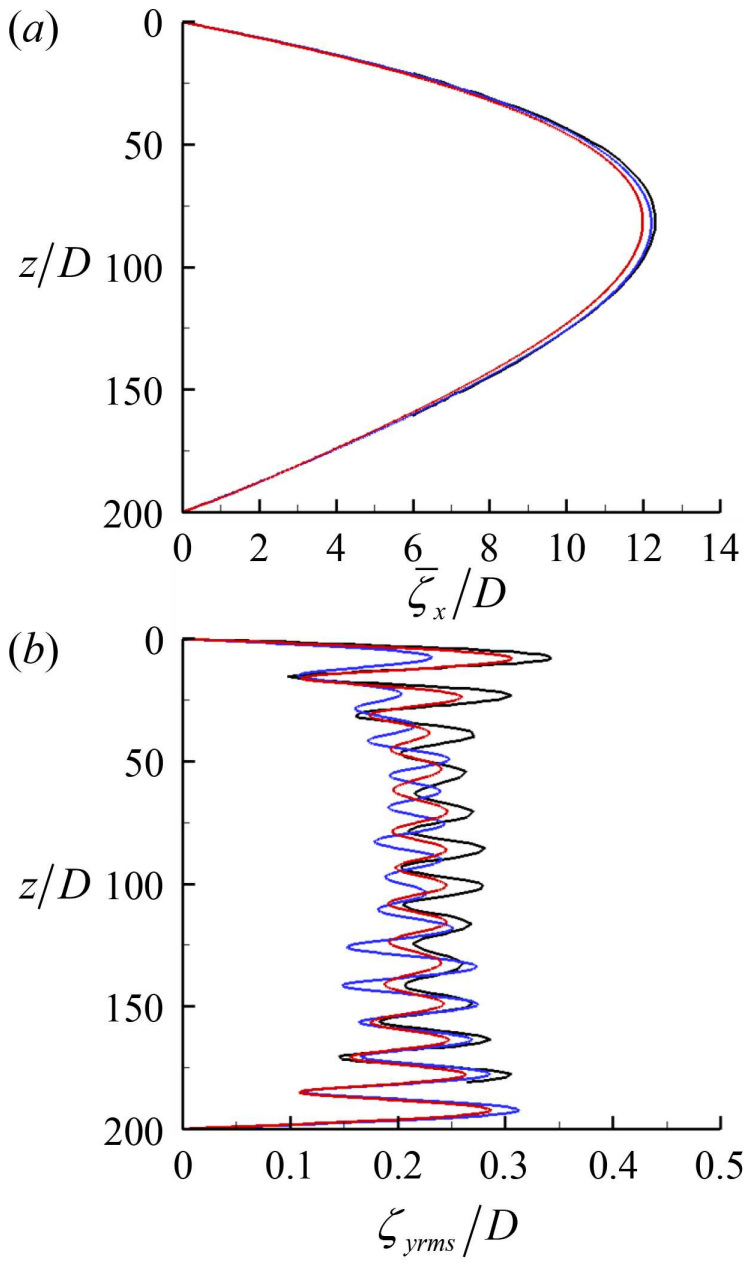

Figure 3.16. Mean streamwise displacement and root mean square of transverse displacement along the spanwise direction for a flexible circular cylinder: (a) $\bar{\zeta}_x/D$; (b) ζ_{yrms}/D. Red line, present simulation with the buffer region; blue line, present simulation without the buffer region; black line, Bourguet *et al.* (2011).

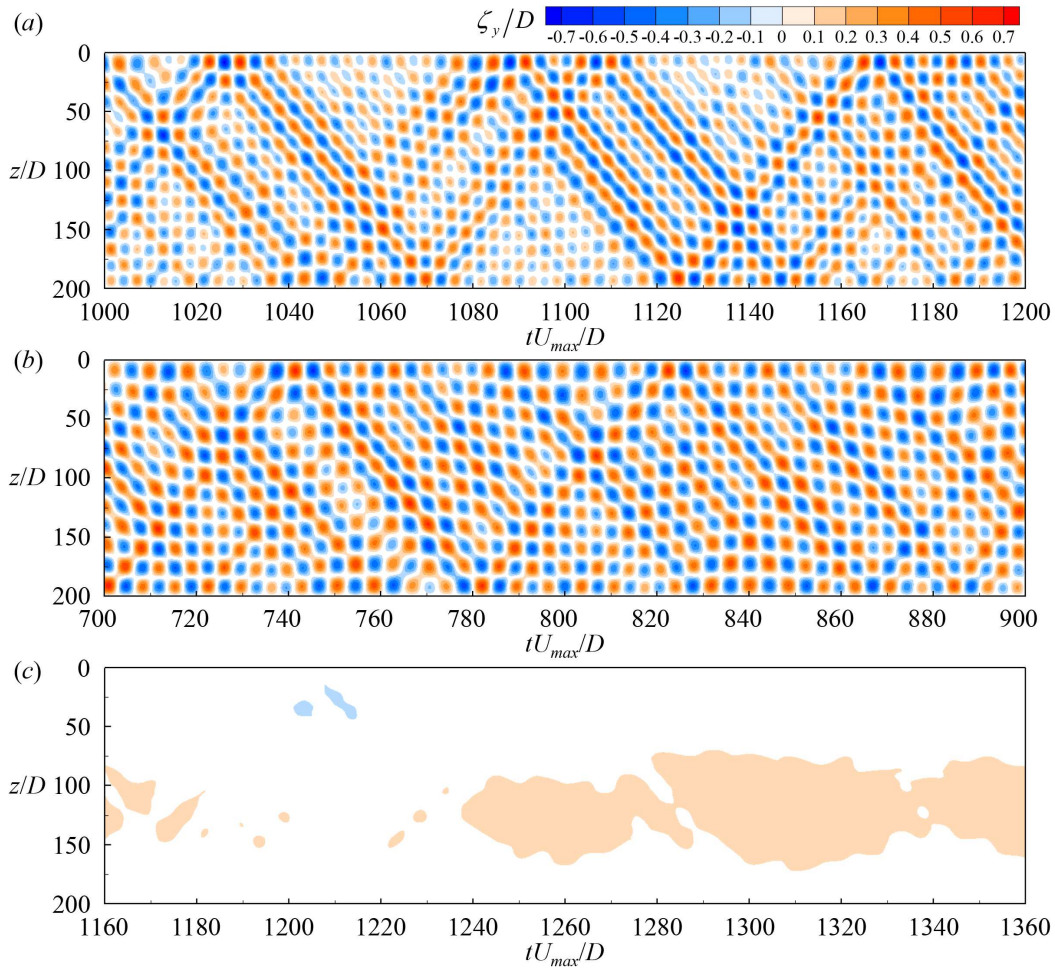

Figure 3.17. Time histories of the transverse displacement along the spanwise direction for flexible cylinders: (a) circular cylinder; (b) HTE cylinder with $AR_H = 1.3$ and $\lambda_H/D = 4$; (c) HTE cylinder with $AR_H = 2.6$ and $\lambda_H/D = 10$.

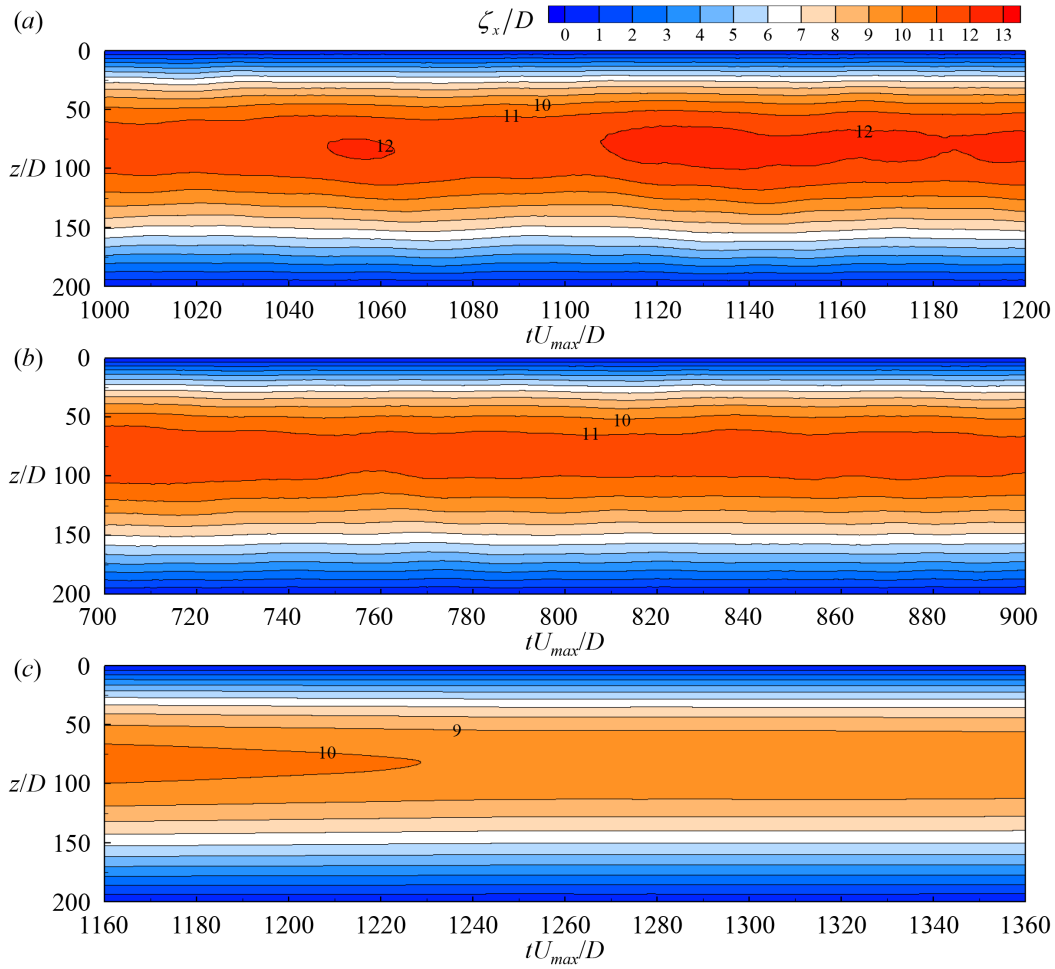

Figure 3.18. Time histories of the streamwise displacement along the spanwise direction for flexible cylinders: (a) circular cylinder; (b) HTE cylinder with $AR_H = 1.3$ and $\lambda_H/D = 4$; (c) HTE cylinder with $AR_H = 2.6$ and $\lambda_H/D = 10$.

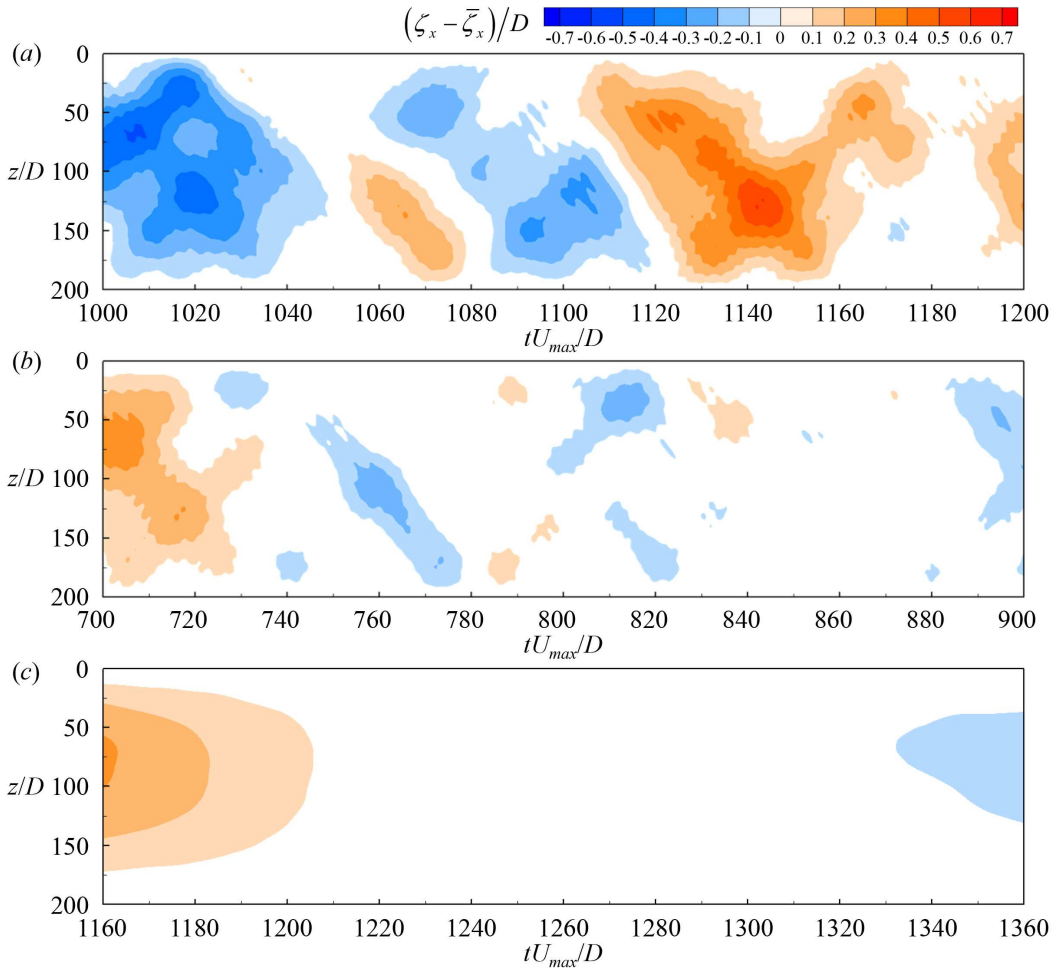

Figure 3.19. Time histories of the streamwise displacement fluctuation along the spanwise direction for flexible cylinders: (a) circular cylinder; (b) HTE cylinder with $AR_H = 1.3$ and $\lambda_H/D = 4$; (c) HTE cylinder with $AR_H = 2.6$ and $\lambda_H/D = 10$.

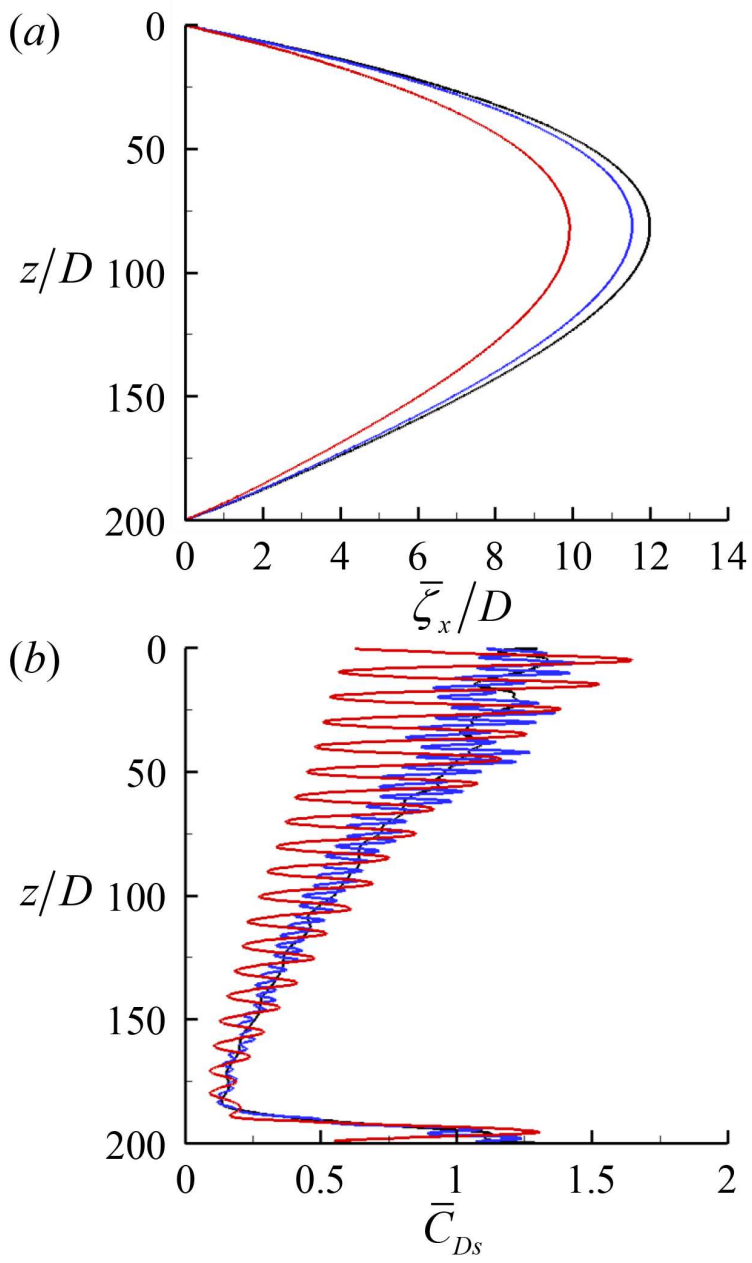

Figure 3.20. Mean streamwise displacement and sectional drag coefficient for flexible cylinders: (*a*) $\bar{\zeta}_x/D$; (*b*) $\bar{C}_{Ds}$. Black line, circular cylinder; blue line, HTE cylinder with $AR_H = 1.3$ and $\lambda_H/D = 4$; red line, HTE cylinder with $AR_H = 2.6$ and $\lambda_H/D = 10$.

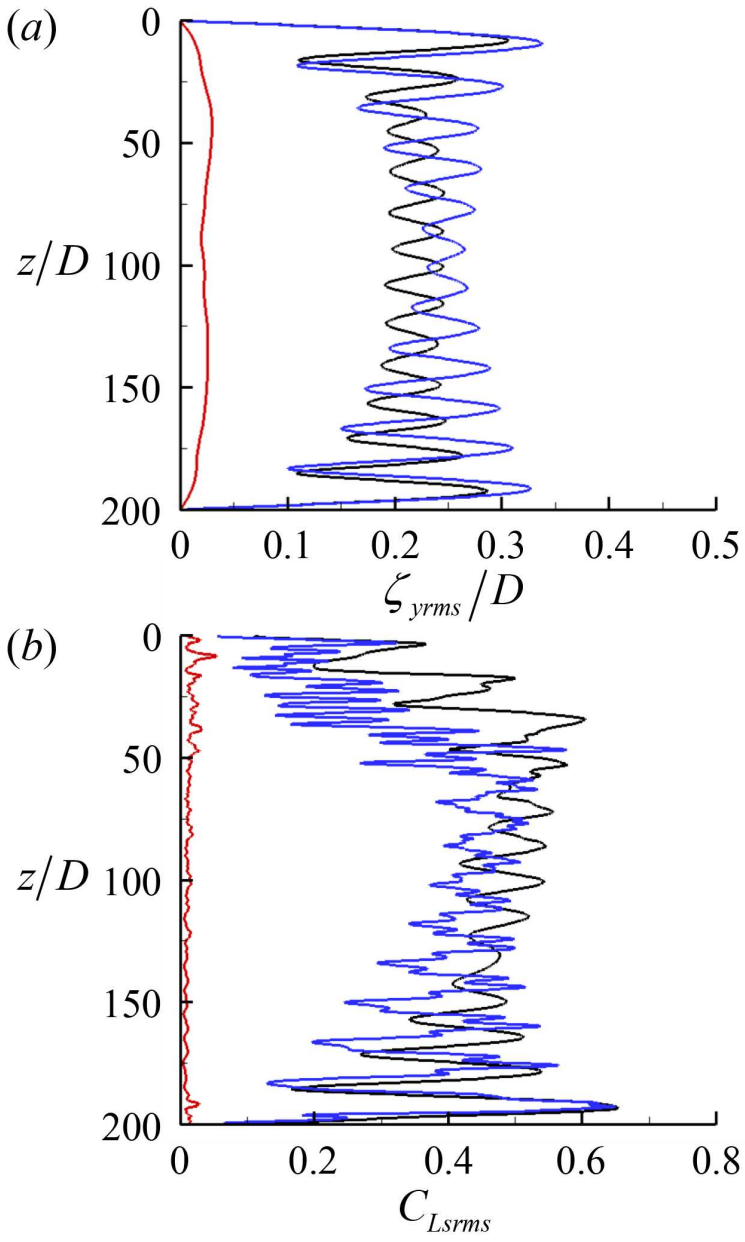

Figure 3.21. Root mean square of the transverse displacement and sectional lift coefficient for flexible cylinders: (a) ζ_{yrms}/D; (b) $\bar{C}_{Lsrms}$. Black line, circular cylinder; blue line, HTE cylinder with $AR_H = 1.3$ and $\lambda_H/D = 4$; red line, HTE cylinder with $AR_H = 2.6$ and $\lambda_H/D = 10$.

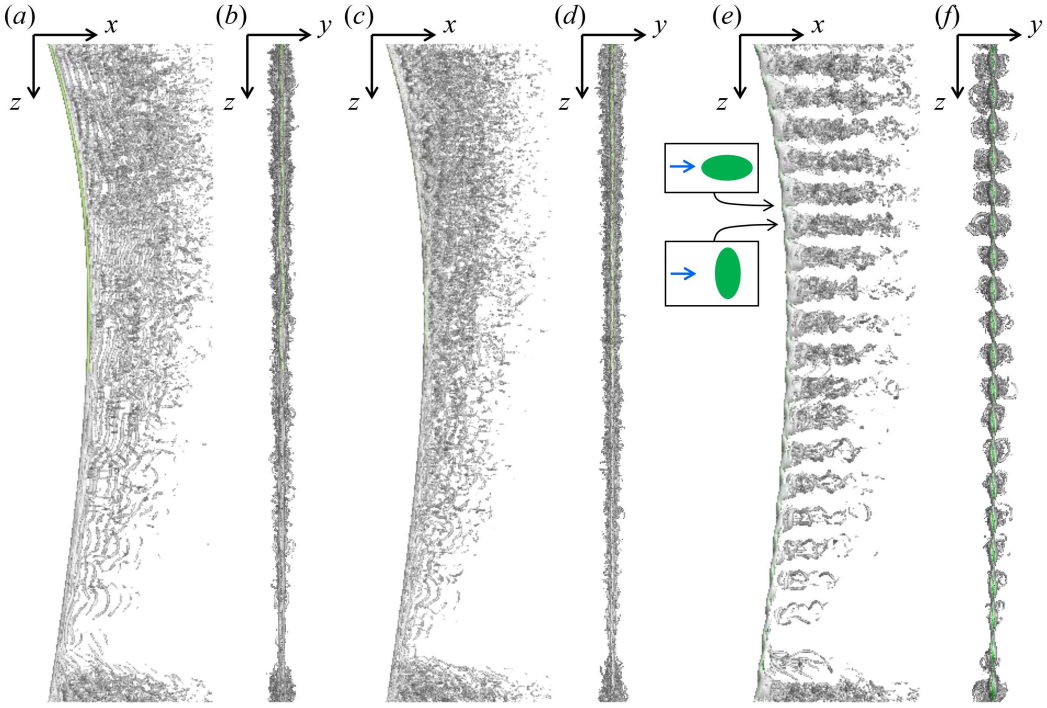

Figure 3.22. Instantaneous vortical structures around a flexible circular cylinder from the (a) side and (b) front views, the flexible HTE cylinder with $AR_H = 1.3$ and $\lambda_H/D = 4$ from the (c) side and (d) front views, and the flexible HTE cylinder with $AR_H = 2.6$ and $\lambda_H/D = 10$ from the (e) side and (f) front views.

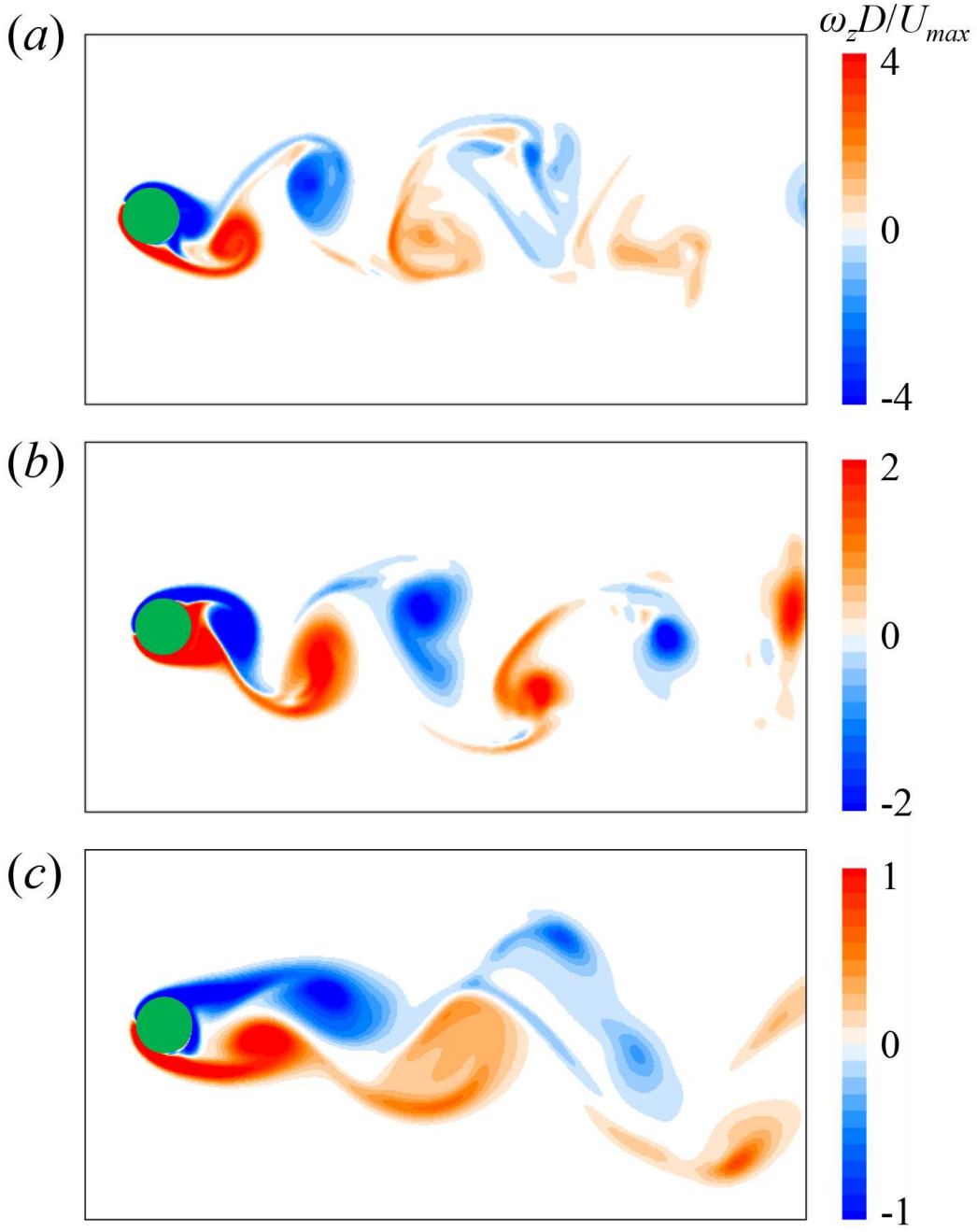

Figure 3.23. Contours of the instantaneous spanwise vorticity around a flexible circular cylinder: (a) $z/D = 7$; (b) 50; (c) 149.

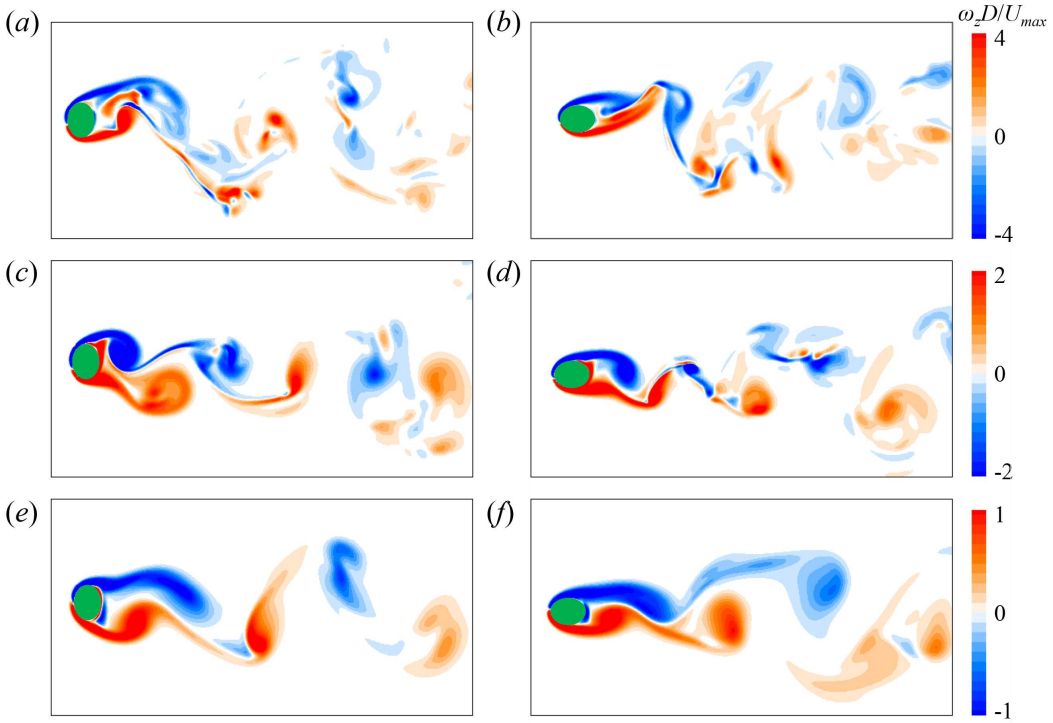

Figure 3.24. Contours of the instantaneous spanwise vorticity around the flexible HTE cylinder with $AR_H = 1.3$ and $\lambda_H/D = 4$: (a) $z/D = 6$; (b) 8; (c) 50; (d) 52; (e) 150; (f) 152.

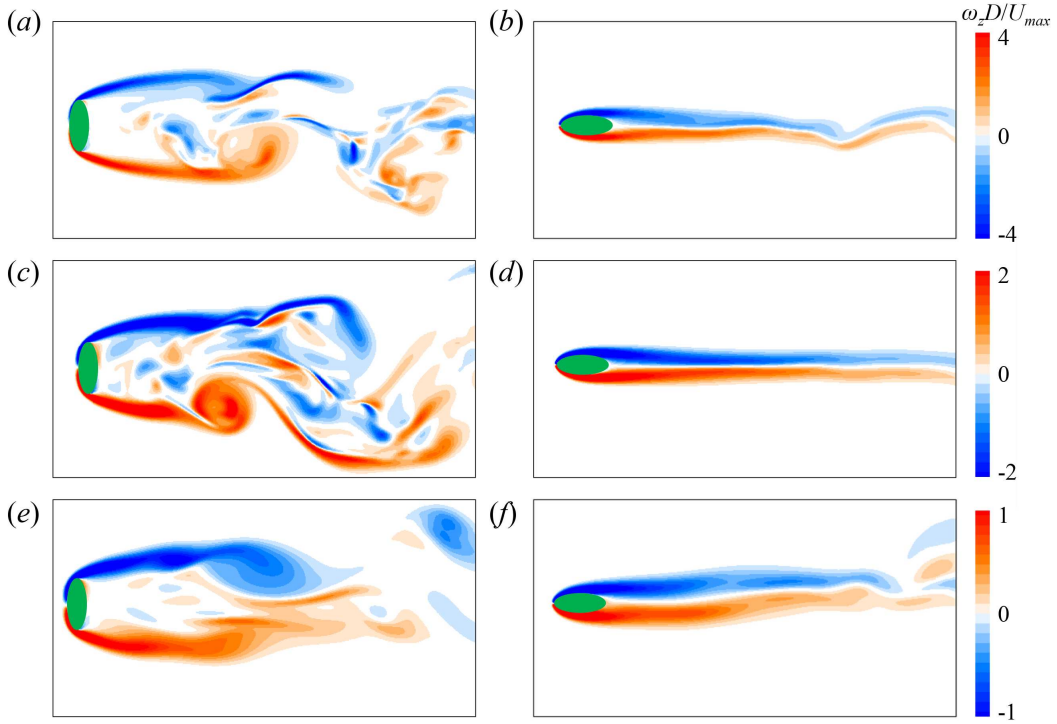

Figure 3.25. Contours of the instantaneous spanwise vorticity around the flexible HTE cylinder with $AR_H = 2.6$ and $\lambda_H/D = 10$: (a) $z/D = 5$; (b) 10; (c) 45; (d) 50; (e) 145; (f) 150.

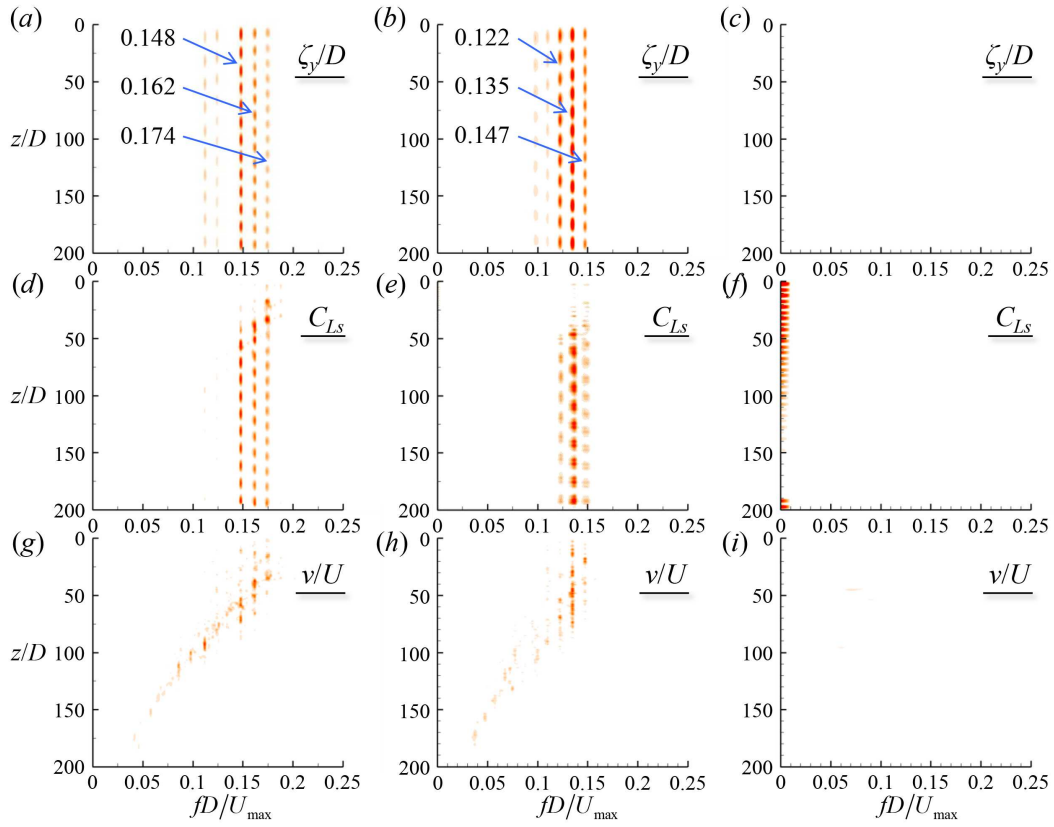

Figure 3.26. Power spectra density of the transverse displacement $(a–c)$, sectional lift coefficient $(d–f)$, and transverse fluid velocity at $x/D = 20$ and $y/D = 0$ $(g–i)$ for flexible cylinders: ζ_y/D for (a) a circular cylinder, (b) the HTE cylinder with $AR_H = 1.3$ and $\lambda_H/D = 4$, (c) the HTE cylinder with $AR_H = 2.6$ and $\lambda_H/D = 10$; C_{Ls} for (d) a circular cylinder, (e) the HTE cylinder with $AR_H = 1.3$ and $\lambda_H/D = 4$, (f) the HTE cylinder with $AR_H = 2.6$ and $\lambda_H/D = 10$; v/U for (g) a circular cylinder, (h) the HTE cylinder with $AR_H = 1.3$ and $\lambda_H/D = 4$, (i) the HTE cylinder with $AR_H = 2.6$ and $\lambda_H/D = 10$.

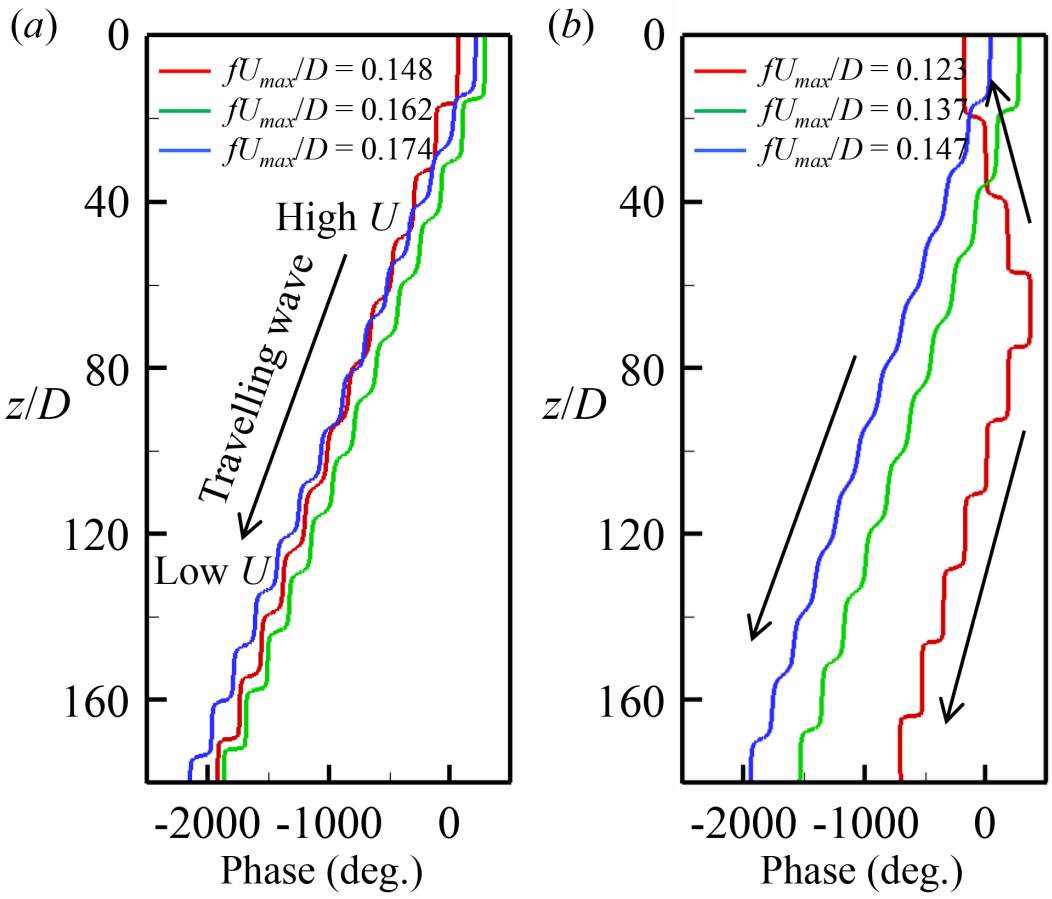

Figure 3.27. Spanwise evolution of selected temporal mode phase angles for flexible cylinders: (a) circular cylinder; (b) HTE cylinder with $AR_H = 1.3$ and $\lambda_H/D = 4$.

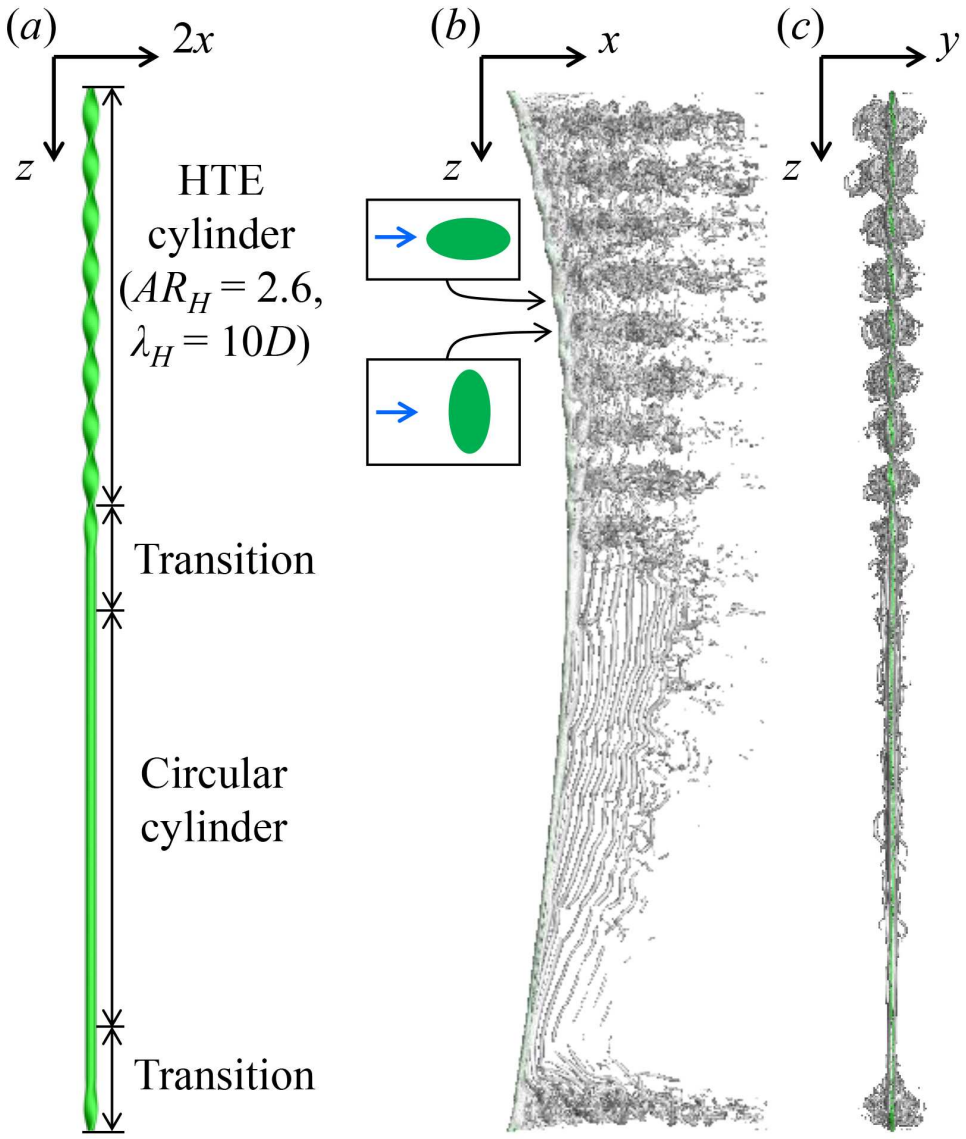

Figure 3.28. Partial HTE cylinder with $AR_H = 2.6$ and $\lambda_H/D = 10$: (a) schematic diagram; instantaneous vortical structures around the flexible partial HTE cylinder from the (b) side and (c) front views. The partial HTE cylinder is composed of the HTE cylinder from $z/D = 0$ to 80, a circular cylinder from $z/D = 90$ to 190, and transition region from $z/D = 80$ to 90 and 190 to 200. In the transition region, the major and minor axes linearly change from the HTE cylinder to a circular cylinder and vice versa.

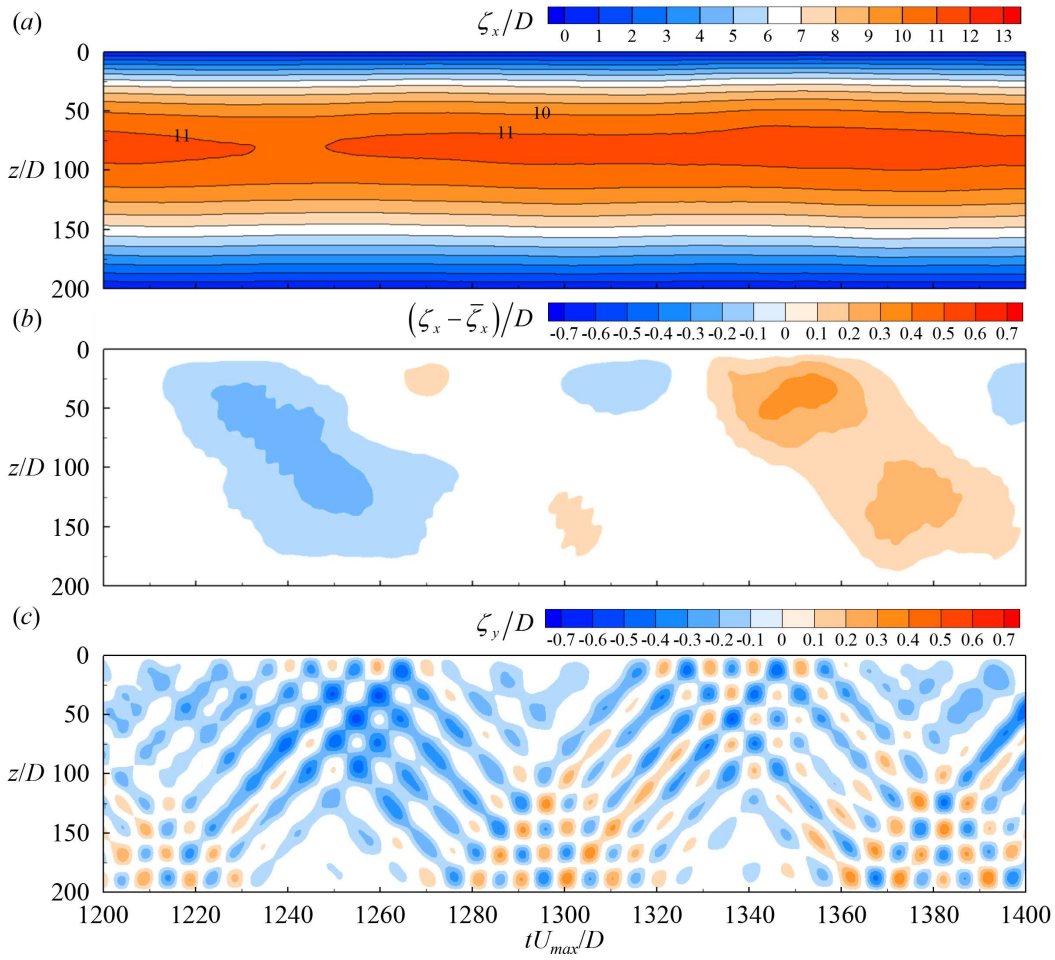

Figure 3.29. Partial HTE cylinder with $AR_H = 2.6$ and $\lambda_H/D = 10$: Time histories of (a) the streamwise displacement (ζ_x), (b) streamwise displacement fluctuation $(\zeta_x - \bar{\zeta_x})$, and (c) transverse displacement (ζ_y) along the spanwise direction.

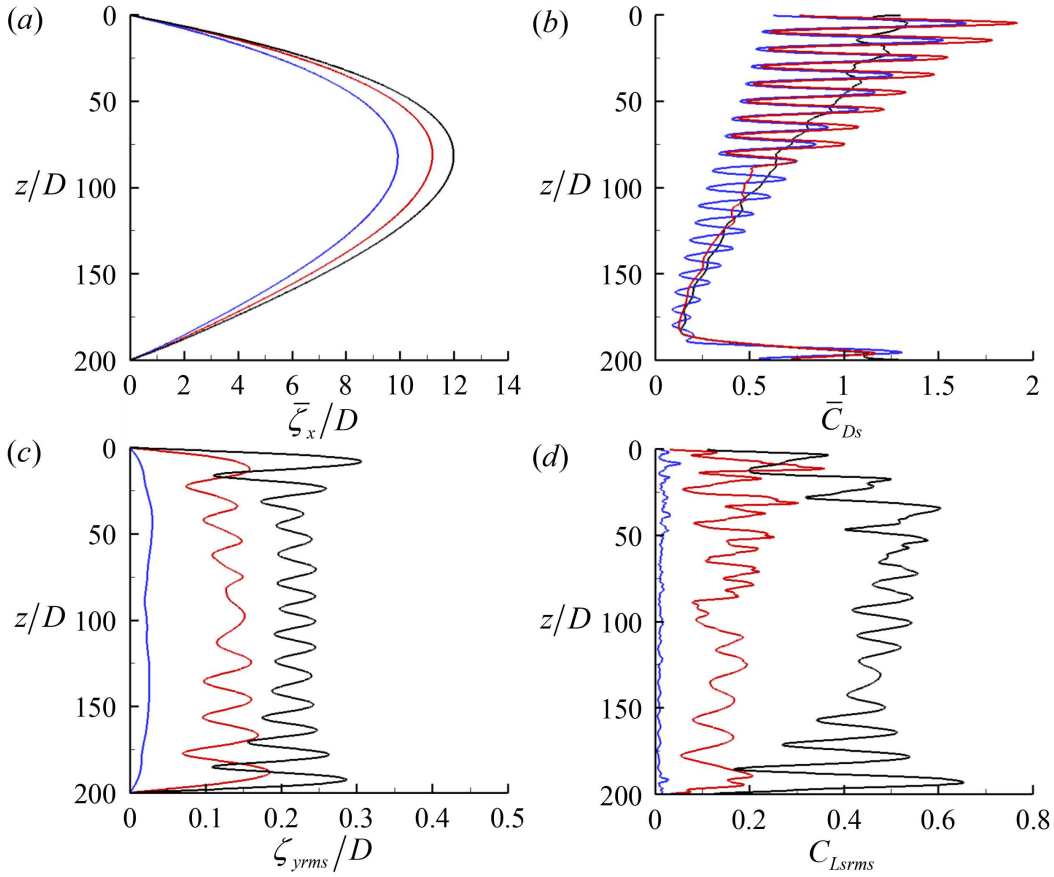

Figure 3.30. Mean streamwise displacement and sectional drag coefficient and root mean square of the transverse displacement and sectional lift coefficient for flexible cylinders: (a) $\bar{\zeta}_x/D$; (b) $\bar{C}_{Ds}$; (c) ζ_{yrms}/D; (d) C_{Lsrms}. Black line, circular cylinder; blue line, HTE cylinder with $AR_H = 2.6$ and $\lambda_H/D = 10$; red line, partial HTE cylinder with $AR_H = 2.6$ and $\lambda_H/D = 10$.

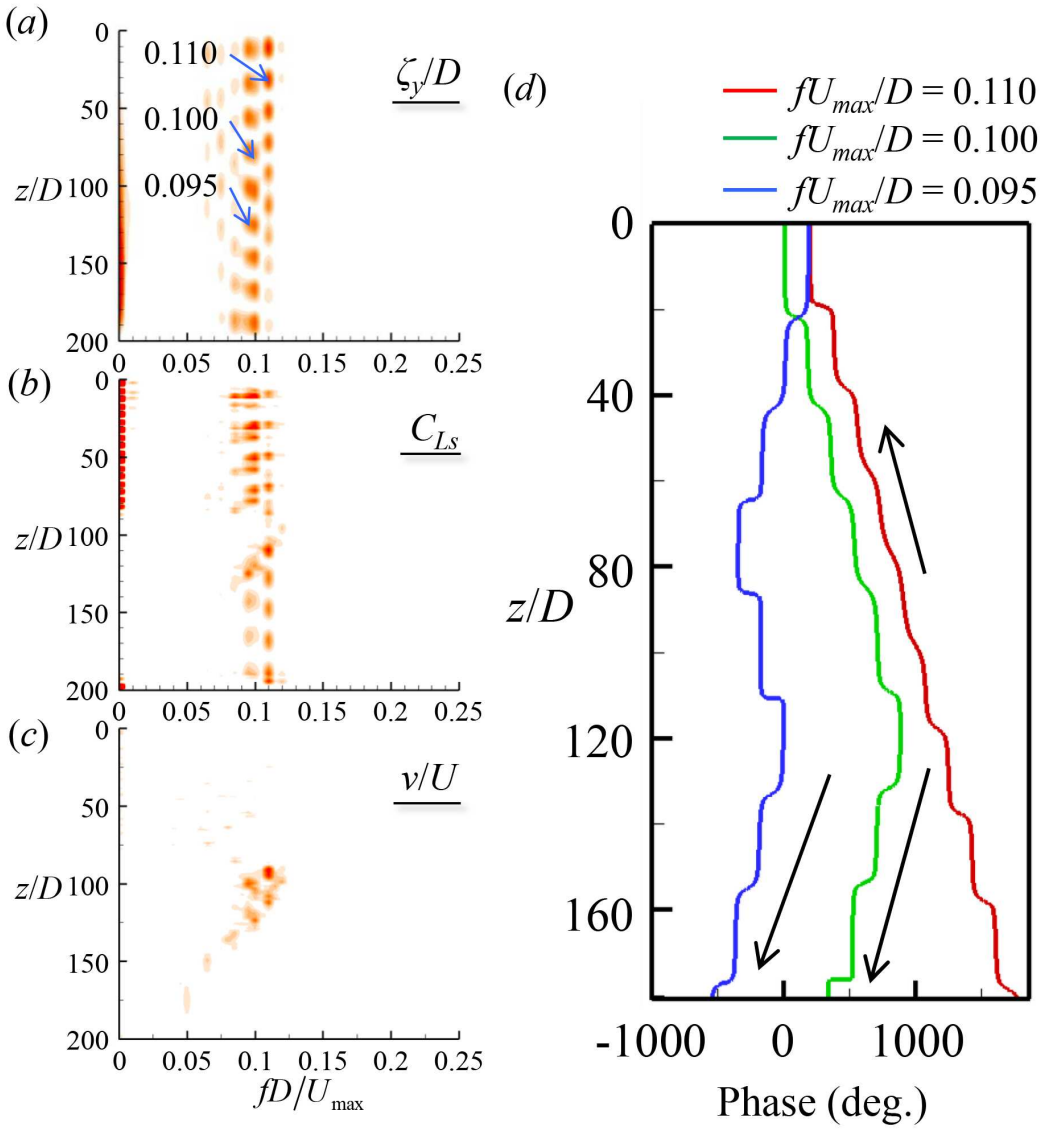

Figure 3.31. Power spectra density of (a) the transverse displacement, (b) sectional lift coefficient and (c) transverse fluid velocity at $x/D = 20$ and $y/D = 0$, and (d) the spanwise evolution of selected temporal mode phase angles for the flexible partial HTE cylinder with $AR_H = 2.6$ and $\lambda_H/D = 10$.

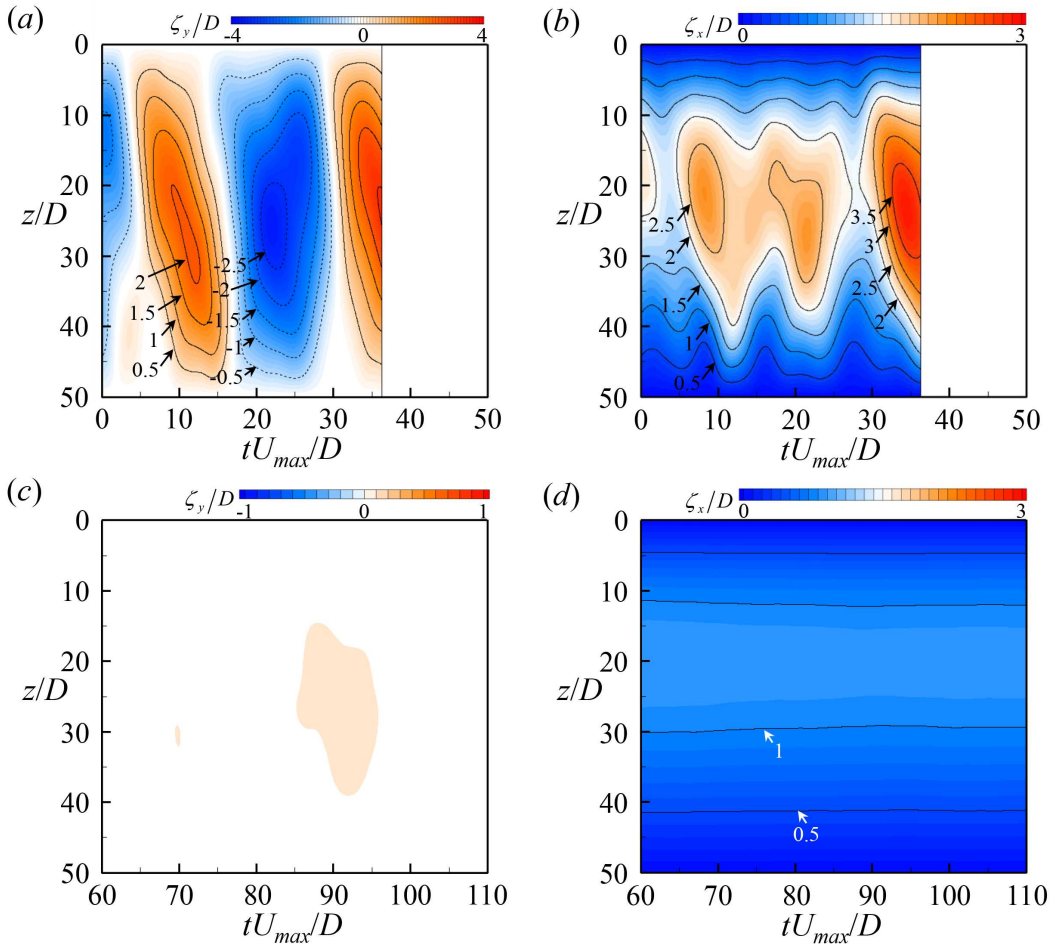

Figure 3.32. Time traces of the transverse and streamwise displacements along the spanwise direction for flexible circular and HTE cylinders with $AR_H = 2.6$ and $\lambda_H/D = 10$: (a) ζ_y and (b) ζ_x of a circular cylinder; (c) ζ_y and (d) ζ_x of the HTE cylinder.

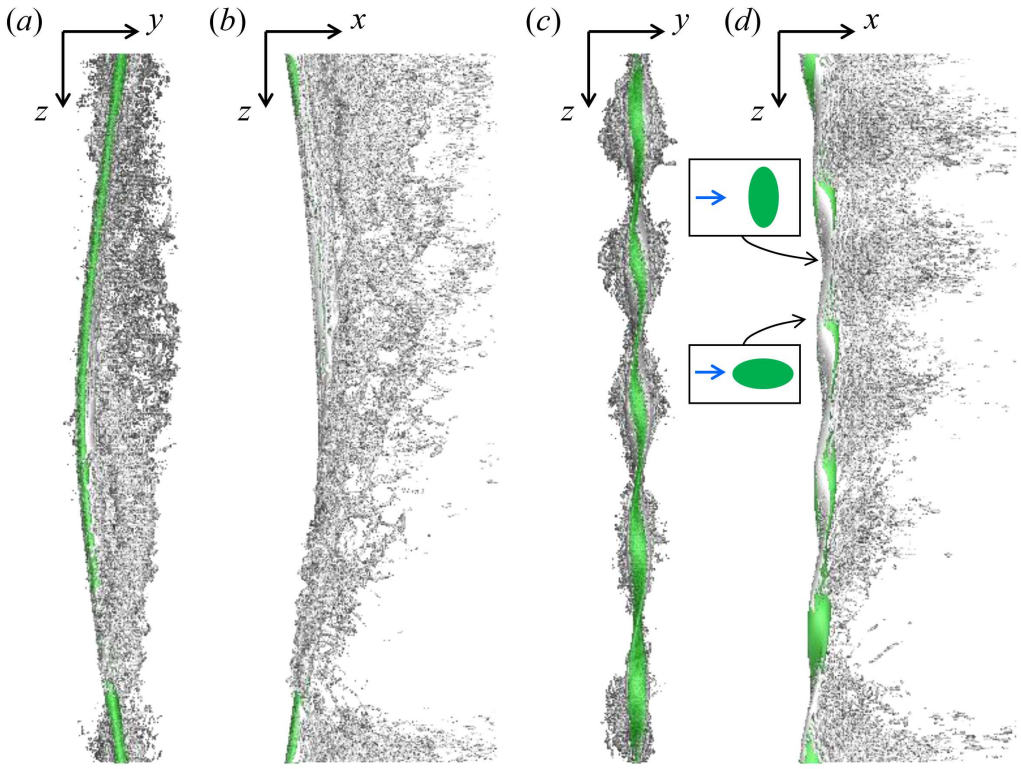

Figure 3.33. Instantaneous vortical structures around a flexible circular cylinder from the (a) front and (b) side views and the flexible HTE cylinder with $AR_H/D = 2.6$ and $\lambda_H/D = 10$ from the (c) front and (d) side views.

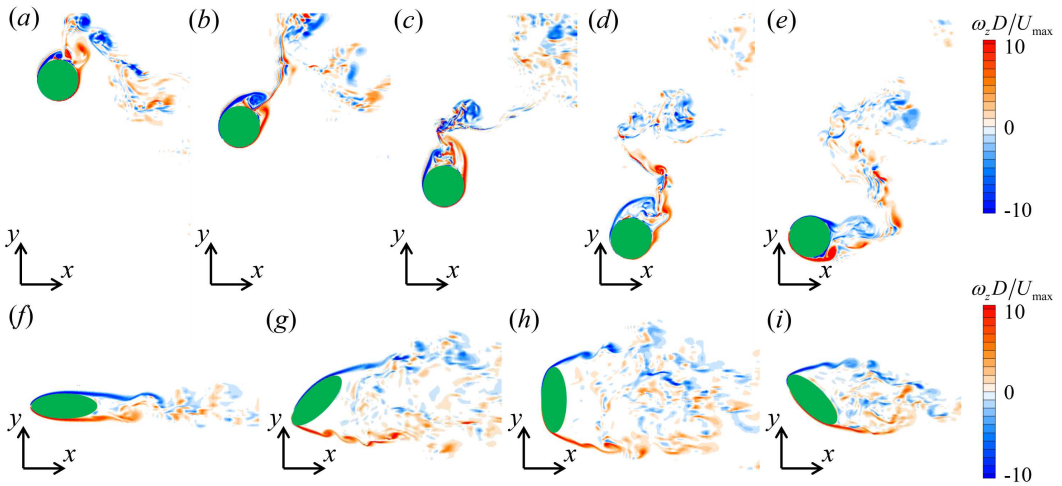

Figure 3.34. Contours of the instantaneous spanwise vorticity for flexible circular and HTE cylinders with $AR_H = 2.6$ and $\lambda_H/D = 10$: ω_z on the xy plane ($z/D = 25$) for the circular cylinder at (a) $tU_{max}/D = 13.6$, (b) 15.9, (c) 18.5, (d) 21.1, and (e) 23.6; ω_z on the (f) $z/D = 20$, (g) 22.5, (h) 25, and (i) 27.5 at $tU_{max}/D = 49.3$ for the HTE cylinder with $AR_H = 2.6$ and $\lambda_H/D = 10$.

Chapter 4

Collapse of the Tacoma Narrows Bridge

4.1 Objectives

The Tacoma Narrows Bridge was opened on July 1, 1940 but collapsed on November 7, 1940. Early on the morning of November 7, the wind velocity was 17.9 to 20.1 m/s and the main span was transversely vibrating in eight or nine segments with a frequency of 36 vibrations/minute (0.6 Hz) and a double amplitude of about 0.91 m, and then the main span abruptly began to vibrate torsionally in two segments with a frequency of 14 vibrations/minute (0.233 Hz) (Fuller *et al.*, 2008). Later, the torsional frequency changed to 12 vibrations/minute (0.2 Hz) with the amplitude of torsional vibration quickly built up to about 35° each direction, and then the main span broke up (Fuller *et al.*, 2008). There are three issues: 1) What is the cause of the transverse vibration in eight or nine segments with a frequency of 0.6 Hz? 2) How does the transverse vibration change to the torsional vibration? 3) What sustains the torsional vibration with a frequency of 0.2 Hz? In the present study, we will investigate the flow around the Tacoma Narrows Bridge torsionally vibrating to answer 3).

4.2 Computational details

A nonlinear model for a suspension bridge suggested by Arioli & Gazzola (2017) is used as the governing equations for the transverse and rotational motions of the center of the deck for the Tacoma Narrows Bridge:

$$
\begin{aligned}
&(M_T + 2m_T\xi_T)\,\frac{\partial^2 Y_C}{\partial t^2} = -E_s I_T \frac{\partial^4 Y_C}{\partial z^4} + \\
&H_{0T}\frac{\partial}{\partial z}\left[\frac{2}{\xi_T^2}\frac{\partial Y_C}{\partial z} + \frac{3}{\xi_T^4}\frac{\partial s_T}{\partial z}\left(\left(\frac{\partial Y_C}{\partial z}\right)^2 + \left(l_T\frac{\partial \theta_C}{\partial z}\right)^2\right)\right] - \\
&\frac{A_T E_s}{L_{cT}}\left[\int_0^{L_T}\frac{1}{\xi_T^3}\left(\left(\frac{\partial Y_C}{\partial z}\right)^2 + \left(l_T\frac{\partial \theta_T}{\partial z}\right)^2\right)dz\right]\frac{1}{\xi_T^3}\frac{\partial^2 s_T}{\partial z^2} - \\
&\frac{2A_T E_s}{L_{cT}}\left[\int_0^{L_T}\frac{1}{\xi^3}\frac{\partial^2 s_T}{\partial z^2}Y_C\,dz\right]\frac{\partial}{\partial z}\left[\frac{1}{\xi_T}\frac{\partial s_T}{\partial z} - \frac{1}{\xi^3}\frac{\partial Y_C}{\partial z}\right] + \\
&\frac{2A_T E_s l_T^2}{L_{cT}}\left[\int_0^{L_T}\frac{1}{\xi^3}\frac{\partial^2 s_T}{\partial z^2}\theta_C\,dz\right]\frac{\partial}{\partial z}\left[\frac{1}{\xi_T^3}\frac{\partial \theta_C}{\partial z}\right] + \rho_f U^2 h_T\frac{C_{Ls}}{2},
\end{aligned}
\tag{4.1}
$$

$$
\begin{aligned}
&\left(\frac{M_T}{3} + 2m_T\xi_T\right)\frac{\partial^2 \theta_C}{\partial t^2} = \frac{G_T K_T}{l_T^2}\frac{\partial^2 \theta_C}{\partial z^2} + \\
&2H_{0T}\frac{\partial}{\partial z}\left[\frac{1}{\xi_T^2}\frac{\partial \theta_C}{\partial z} + 3\frac{1}{\xi_T^4}\frac{\partial s_T}{\partial z}\frac{\partial Y_C}{\partial z}\frac{\partial \theta_C}{\partial z}\right] - \\
&\frac{2A_T E_s}{L_{cT}}\left[\int_0^{L_T}\frac{1}{\xi_T^3}\frac{\partial Y_C}{\partial z}\frac{\partial \theta_C}{\partial z}\,dz\right]\frac{1}{\xi_T^3}\frac{\partial^2 s_T}{\partial z^2} - \\
&\frac{2A_T E_s}{L_{cT}}\left[\int_0^{L_T}\frac{1}{\xi_T^3}\frac{\partial^2 s_T}{\partial z^2}\theta_C\,dz\right]\frac{\partial}{\partial z}\left[\frac{1}{\xi_T}\frac{\partial s_T}{\partial z} - \frac{1}{\xi_T^3}\frac{\partial Y_C}{\partial z}\right] + \\
&\frac{2A_T E_s}{L_{cT}}\left[\int_0^{L_T}\frac{1}{\xi_T^3}\frac{\partial^2 s_T}{\partial z^2}Y_C\,dz\right]\frac{\partial}{\partial z}\left(\frac{1}{\xi_T^3}\frac{\partial \theta_C}{\partial z}\right) + \rho_f U^2 h_T^2\frac{C_{Ms}}{2l_T^2},
\end{aligned}
\tag{4.2}
$$

where z is the spanwise direction, Y_C and θ_C are the transverse displacement and rotational angle of the center of the deck, respectively, M_T is the mass of the deck per unit length, m_T is the mass of the cable per unit length, ξ_T is the local length of the cable at rest, E_s is the Young modulus of the deck and the cables, I_T is the linear density of the moment of inertia of the cross section, H_{0T} is the spanwise component of the tension of the cables, A_T is the area of the section of the cable, L_{cT} is the length of the cable, l_T is the half width of the deck, s_T is the position of the cables, G_T is the shear modulus of the deck, K_T is the torsional constant of the deck, C_{Ls} is the section lift coefficient, C_{Ms} is the sectional moment coefficient, L_T is the length of the deck, h_T is the height of the deck, ρ_f is the fluid density, and U is the wind velocity. The physical and geometrical parameters are obtained from Arioli & Gazzola (2017): $M_T = 7198$ kg/m, $m_T = 981$ kg/m, $E_s = 210$ GPa, $I_T = 0.15$ m^4, $H_{0T} = 58300$ kN, $A_T = 0.1228$ m^2, $L_{cT} = 868.62$ m, $l_T = 6$ m, $G_T = 81$ GPa, $K_T = 6.44 \times 10^{-6}$ m^4, $L_T = 853.44$ m, $h_T = 2.4$ m, $\rho_f = 1.247$ kg/m^3, and $U = 18$ m/s. The thickness of the deck (b_T) is $0.221h_T$ and the thickness of railings (a_T) is $0.05h_T$. At rest, the cables reach the equilibrium state due to the balance of the tension and gravity:

$$H_{0T}\frac{\partial^2 s_T}{\partial z^2} = \left[\frac{M_T}{2} + m\sqrt{1 + \left(\frac{\partial s_T}{\partial z}\right)^2}\right] g, \tag{4.3}$$

where g is the gravity acceleration (9.81 m/s^2). At the lateral sides, $s(0) = s(L_T) = 72$ m.

Figure 4.1 shows the schematic diagram of computational domain and boundary conditions for the simulation of flow around the Tacoma Narrows Bridge. Here, the effects of the cables, hangers, and towers are not considered for the

simulation of flow around the Tacoma Narrows Bridge. The Reynolds number based on the height of the deck is 3.06×10^6 for the air at temperature of 10°C, which requires a huge amount of computational cost. Instead, the Reynolds number of 300 is used in the present simulation because the frequency of vortex shedding for flow around a bluff body is not significantly altered in the wide range of the Reynolds number (i.e., a circular cylinder (Norberg, 2003)). Later, the simulation of flow around the Tacoma Narrows Bridge at the higher Reynolds number will be conducted.

The computational domain size is [-30h_T,25h_T]×[-30h_T,30h_T]×[0,355.6h_T], where the center of the Tacoma Narrows Bridge is initially located at (x,y) = (0,0). The number of grid points is 497×397×2048 in the streamwise (x), transverse (y), and spanwise (z) directions. The smallest grid spacing near the Tacoma Narrows Bridge is $\Delta x = \Delta y = 0.02$, and the uniform grid spacing is used in the spanwise direction ($\Delta z = 0.17363$). The Dirichlet boundary condition ($u = U, v = w = 0$) is applied at the inlet. At the top and bottom sides, the Dirichlet ($v = 0$) and Newumann ($\partial u/\partial y = \partial w/\partial y = 0$) boundary conditions are imposed. A convective boundary condition ($\partial u_i/\partial t + u_c \partial u_i/\partial x = 0$) is used at the outlet boundary, where u_c is the streamwise velocity averaged over the outflow boundary.

The generalized-α method (Chung & Hulbert, 1993) is applied to equations (4.1) and (4.2) with an iterative manner due to the nonlinear terms:

$$
\begin{aligned}
&(M_T + 2m_T\xi_T)\left[(1-\alpha_m)\frac{\partial^2 Y_C^k}{\partial t^2} + \alpha_m \frac{\partial^2 Y_C^{n-1}}{\partial t^2}\right] \\
&= -E_s I_T \left[(1-\alpha_f)\frac{\partial^4 Y_C^k}{\partial z^4} + \alpha_f \frac{\partial^4 Y_C^{n-1}}{\partial z^4}\right] + \\
&H_{0T}\frac{\partial}{\partial z}\left[\frac{2}{\xi_T^2}\left((1-\alpha_f)\frac{\partial Y_C^k}{\partial z} + \alpha_f \frac{\partial Y_C^{n-1}}{\partial z}\right)\right] + \\
&H_{0T}\frac{\partial}{\partial z}\left[\frac{3}{\xi_T^4}\frac{\partial s_T}{\partial z}(1-\alpha_f)\left(\left(\frac{\partial Y_C^{k-1}}{\partial z}\right)^2 + \left(l_T\frac{\partial \theta_C^{k-1}}{\partial z}\right)^2\right)\right] + \\
&H_{0T}\frac{\partial}{\partial z}\left[\frac{3}{\xi_T^4}\frac{\partial s_T}{\partial z}\alpha_f\left(\left(\frac{\partial Y_C^{n-1}}{\partial z}\right)^2 + \left(l_T\frac{\partial \theta_C^{n-1}}{\partial z}\right)^2\right)\right] - \\
&(1-\alpha_f)\frac{A_T E_s}{L_{cT}}\left[\int_0^{L_T}\frac{1}{\xi_T^3}\left(\left(\frac{\partial Y_C^{k-1}}{\partial z}\right)^2 + \left(l_T\frac{\partial \theta_T^{k-1}}{\partial z}\right)^2\right)dz\right]\frac{1}{\xi_T^3}\frac{\partial^2 s_T}{\partial z^2} - \\
&\alpha_f\frac{A_T E_s}{L_{cT}}\left[\int_0^{L_T}\frac{1}{\xi_T^3}\left(\left(\frac{\partial Y_C^{n-1}}{\partial z}\right)^2 + \left(l_T\frac{\partial \theta_T^{n-1}}{\partial z}\right)^2\right)dz\right]\frac{1}{\xi_T^3}\frac{\partial^2 s_T}{\partial z^2} - \\
&(1-\alpha_f)\frac{2A_T E_s}{L_{cT}}\left[\int_0^{L_T}\frac{1}{\xi^3}\frac{\partial^2 s_T}{\partial z^2}Y_C^{k-1}\,dz\right]\frac{\partial}{\partial z}\left[\frac{1}{\xi_T}\frac{\partial s_T}{\partial z} - \frac{1}{\xi^3}\frac{\partial Y_C^{k-1}}{\partial z}\right] - \\
&\alpha_f\frac{2A_T E_s}{L_{cT}}\left[\int_0^{L_T}\frac{1}{\xi^3}\frac{\partial^2 s_T}{\partial z^2}Y_C^{n-1}\,dz\right]\frac{\partial}{\partial z}\left[\frac{1}{\xi_T}\frac{\partial s_T}{\partial z} - \frac{1}{\xi^3}\frac{\partial Y_C^{n-1}}{\partial z}\right] + \\
&(1-\alpha_f)\frac{2A_T E_s l_T^2}{L_{cT}}\left[\int_0^{L_T}\frac{1}{\xi^3}\frac{\partial^2 s_T}{\partial z^2}\theta_C^{k-1}\,dz\right]\frac{\partial}{\partial z}\left[\frac{1}{\xi_T^3}\frac{\partial \theta_C^{k-1}}{\partial z}\right] + \\
&\alpha_f\frac{2A_T E_s l_T^2}{L_{cT}}\left[\int_0^{L_T}\frac{1}{\xi^3}\frac{\partial^2 s_T}{\partial z^2}\theta_C^{n-1}\,dz\right]\frac{\partial}{\partial z}\left[\frac{1}{\xi_T^3}\frac{\partial \theta_C^{n-1}}{\partial z}\right] + \\
&\rho_f U^2 h_T\frac{1}{2}\left[(1-\alpha_f)C_{Ls}^n + \alpha_f C_{Ls}^{n-1}\right],
\end{aligned}
\tag{4.4}
$$

$$
Y_C^k = Y_C^{n-1} + \Delta t\frac{\partial Y_C^{n-1}}{\partial t} + \Delta t^2\left[(0.5-\beta)\frac{\partial^2 Y_C^{n-1}}{\partial t^2} + \beta\frac{\partial^2 Y_C^k}{\partial t^2}\right], \tag{4.5}
$$

$$\frac{\partial Y_C^k}{\partial t} = \frac{\partial Y_C^{n-1}}{\partial t} + \Delta t \left[(1-\gamma) \frac{\partial^2 Y_C^{n-1}}{\partial t^2} + \gamma \frac{\partial^2 Y_C^k}{\partial t^2} \right], \tag{4.6}$$

$$\begin{aligned}
&\left(\frac{M_T}{3} + 2 m_T \xi_T \right) \left[(1-\alpha_m) \frac{\partial^2 \theta_C^k}{\partial t^2} + \alpha_m \frac{\partial^2 \theta_C^{n-1}}{\partial t^2} \right] \\
&= (1-\alpha_f) \frac{G_T K_T}{l_T^2} \frac{\partial^2 \theta_C^k}{\partial z^2} + \alpha_f \frac{G_T K_T}{l_T^2} \frac{\partial^2 \theta_C^{n-1}}{\partial z^2} + \\
&(1-\alpha_f) 2 H_{0T} \frac{\partial}{\partial z} \left[\frac{1}{\xi_T^2} \frac{\partial \theta_C^k}{\partial z} + 3 \frac{1}{\xi_T^4} \frac{\partial s_T}{\partial z} \frac{\partial Y_C^k}{\partial z} \frac{\partial \theta_C^k}{\partial z} \right] + \\
&\alpha_f 2 H_{0T} \frac{\partial}{\partial z} \left[\frac{1}{\xi_T^2} \frac{\partial \theta_C^{n-1}}{\partial z} + 3 \frac{1}{\xi_T^4} \frac{\partial s_T}{\partial z} \frac{\partial Y_C^{n-1}}{\partial z} \frac{\partial \theta_C^{n-1}}{\partial z} \right] - \\
&(1-\alpha_f) \frac{2 A_T E_s}{L_{cT}} \left[\int_0^{L_T} \frac{1}{\xi_T^3} \frac{\partial Y_C^k}{\partial z} \frac{\partial \theta_C^{k-1}}{\partial z} \, dz \right] \frac{1}{\xi_T^3} \frac{\partial^2 s_T}{\partial z^2} - \\
&\alpha_f \frac{2 A_T E_s}{L_{cT}} \left[\int_0^{L_T} \frac{1}{\xi_T^3} \frac{\partial Y_C^{n-1}}{\partial z} \frac{\partial \theta_C^{n-1}}{\partial z} \, dz \right] \frac{1}{\xi_T^3} \frac{\partial^2 s_T}{\partial z^2} - \\
&(1-\alpha_f) \frac{2 A_T E_s}{L_{cT}} \left[\int_0^{L_T} \frac{1}{\xi_T^3} \frac{\partial^2 s_T}{\partial z^2} \theta_C^{k-1} \, dz \right] \frac{\partial}{\partial z} \left[\frac{1}{\xi_T} \frac{\partial s_T}{\partial z} - \frac{1}{\xi_T^3} \frac{\partial Y_C^k}{\partial z} \right] - \\
&\alpha_f \frac{2 A_T E_s}{L_{cT}} \left[\int_0^{L_T} \frac{1}{\xi_T^3} \frac{\partial^2 s_T}{\partial z^2} \theta_C^{n-1} \, dz \right] \frac{\partial}{\partial z} \left[\frac{1}{\xi_T} \frac{\partial s_T}{\partial z} - \frac{1}{\xi_T^3} \frac{\partial Y_C^{n-1}}{\partial z} \right] + \\
&(1-\alpha_f) \frac{2 A_T E_s}{L_{cT}} \left[\int_0^{L_T} \frac{1}{\xi_T^3} \frac{\partial^2 s_T}{\partial z^2} Y_C^k \, dz \right] \frac{\partial}{\partial z} \left(\frac{1}{\xi_T^3} \frac{\partial \theta_C^k}{\partial z} \right) + \\
&\alpha_f \frac{2 A_T E_s}{L_{cT}} \left[\int_0^{L_T} \frac{1}{\xi_T^3} \frac{\partial^2 s_T}{\partial z^2} Y_C^{n-1} \, dz \right] \frac{\partial}{\partial z} \left(\frac{1}{\xi_T^3} \frac{\partial \theta_C^{n-1}}{\partial z} \right) + \\
&\rho_f U^2 h_T^2 \frac{1}{2 l_T^2} \left[(1-\alpha_f) C_{Ms}^n + \alpha_f C_{Ms}^{n-1} \right],
\end{aligned} \tag{4.7}$$

$$\theta_C^k = \theta_C^{n-1} + \Delta t \frac{\partial \theta_C^{n-1}}{\partial t} + \Delta t^2 \left[(0.5-\beta) \frac{\partial^2 \theta_C^{n-1}}{\partial t^2} + \beta \frac{\partial^2 \theta_C^k}{\partial t^2} \right], \tag{4.8}$$

$$\frac{\partial \theta_C^k}{\partial t} = \frac{\partial \theta_C^{n-1}}{\partial t} + \Delta t \left[(1-\gamma) \frac{\partial^2 \theta_C^{n-1}}{\partial t^2} + \gamma \frac{\partial^2 \theta_C^k}{\partial t^2} \right], \tag{4.9}$$

where k is the iteration step and n is the time step. Weak coupling presented in the section 2.2 is used to couple the governing equations of fluid flow (equations (2.3)–(2.6)) and the transverse and rotational motions of the Tacoma Narrows Bridge (equations (4.4) and (4.9)) together with velocity and displacement predictors (equations (2.18) and (2.19)). The computations are conducted at the maximum CFL number of 1 for weak coupling with $\xi = 1$ (equation (2.18)) and $\chi = 0$ (equations (4.4)–(4.9)).

4.3 Flow-induced vibration of the Tacoma Narrows Bridge

Theoretical natural frequencies of the transverse motion induced by the cables and deck are given as

$$f_{trans,cable,n_m} h_T / U = \frac{1}{2} \sqrt{\frac{2H_{0T}}{(M_T + 2m_T) U^2}} \frac{h_T}{L_T} n_m, \tag{4.10}$$

$$f_{trans,deck,n_m} h_T / U = \frac{\pi}{2} \sqrt{\frac{E_s I_T}{(M_T + 2m_T) U^2 L_T^2}} \frac{h_T}{L_T} n_m^2, \tag{4.11}$$

and the mode corresponding to each natural frequency is given in figure 4.2. The theoretical natural frequency with $n_m = 9$ for the transverse motion due to the cables is 0.59 Hz, and agrees well with the frequency of the transverse vibration observed right before the collapse (0.6 Hz). Theoretical natural frequencies of the rotational motion induced by the cables and deck are given as

$$f_{rot,cable,n_m} h_T / U = \frac{1}{2} \sqrt{\frac{2H_{0T}}{(M_T + 2m_T) U^2}} \frac{h_T}{L_T} n_m, \tag{4.12}$$

$$f_{rot,deck,n_m} h_T/U = \frac{1}{2}\sqrt{\frac{G_T K_T}{(M_T/3 + 2m_T)\, U^2 l_T^2}}\frac{h_T}{L_T} n_m, \tag{4.13}$$

and the mode corresponding to each natural frequency is given in figure 4.2. The theoretical natural frequency with $n_m = 2$ for the rotational motion due to the cables is 0.19 Hz, and agrees well with the frequency of the rotational vibration observed right before the collapse (0.2 Hz). The transverse and rotational motions of the Tacoma Narrows Bridge observed right before the collapse may be induced by the cables.

The following sine wave is given as an initial condition for the angular velocity of the deck to investigate what sustains the rotational motion of the deck:

$$\frac{\partial \theta_C}{\partial t} = 0.1 \sin\left(2\pi z/L_T\right). \tag{4.14}$$

The angle, angular acceleration, lift coefficient, and moment are initially given as 0 and the initial field of $(u, v, w) = (U, 0, 0)$ is given for the flow. Figure 4.3 (a) shows the rotational angle of the deck. The deck torsionally vibrates at the frequency of about 0.025 (0.19 Hz) with the maximum angle of about 50°. For the moment on the deck and the transverse fluid velocity at $x/h_T = 5$ and $y = 0$, the dominant frequency of about 0.025 is observed together with higher frequencies (figure 4.3 (b) and (e)), which implies lock-in between the torsional vibration and vortex shedding. On the other hand, the transverse vibration is generated with the mode of 2 and the dominant frequency of the lift coefficient is about 0.025 (figure 4.3 (c) and (d)).

Figure 4.4 shows the instantaneous vortical structures around the Tacoma Narrows bridge. For $tU/h_T = 45.5$–58.8, a vortex roller generated from the upper side is located in the wake of $z/L_T = 0.5 \sim 1$ and travels downstream

(figure 4.4 (a)–(c)). For $tU/h_T = 64.0$–76.7, a vortex roller generated from the upper side is located in the wake of $z/L_T = 0 \sim 0.5$ and travels downstream (figure 4.4 (d)–(f)). At $tU/h_T = 82.6$, a vortex roller is generated from the upper side and located in the wake of $z/L_T = 0.5 \sim 1$ (figure 4.4 (g)). The vortex generation period in the half spanwise domain is similar to the period of the torsional vibration.

Figure 4.5 shows the contours of the instantaneous spanwise vorticity at $z/L_T = 0.25$. For $tU/h_T = 45.5$–52.4, a strong leading edge vortex is generated on the lower side (figure 4.5 (a)–(b)), which induces positive moment on there. However, for $tU/h_T = 58.8$–64.0, the leading edge vortex travels downstream and is weakened (figure 4.5 (c)–(d)). For $tU/h_T = 70.2$–76.7, a strong leading edge vortex is generated on the upper side (figure 4.5 (e)–(f)), which induces negative moment on there. At $tU/h_T = 82.6$, the leading edge vortex travels downstream and located near the trailing edge, which induces positive moment on there (figure 4.5 (g)).

Figure 4.6 shows the contours of the instantaneous spanwise vorticity at $z/L_T = 0.75$. For $tU/h_T = 45.5$–52.4, a strong leading edge vortex is generated on the upper side (figure 4.6 (a)–(b)), which induces negative moment on there. However, for $tU/h_T = 58.8$–64.0, the leading edge vortex travels downstream and is weakened (figure 4.6 (c)–(d)). For $tU/h_T = 70.2$–76.7, a strong leading edge vortex is generated on the lower side (figure 4.6 (e)–(f)), which induces positive moment on there. At $tU/h_T = 82.6$, the leading edge vortex travels downstream and located near the trailing edge, which induces negative moment on there (figure 4.6 (g)).

4.4 Summary

In the present study, we investigated the flow around the Tacoma Narrows Bridge torsionally vibrating with a frequency similar to the frequency observed right before the collapse of the Tacoma Narrows Bridge. A vortex roller was largely deflected in the transverse direction with the wavelength equal to the length of the Tacoma Narrows Bridge due to the torsional vibration. The inclination of the deck made leading edge vortices stronger and held them longer near the leading edge. Strong leading edge vortices were alternatively generated on the upper and lower sides and induced torsional vibration of the deck. This positive feedback process was possible due to the matching the natural torsional vibration frequency corresponding to the mode of 2 with the vortex shedding frequency.

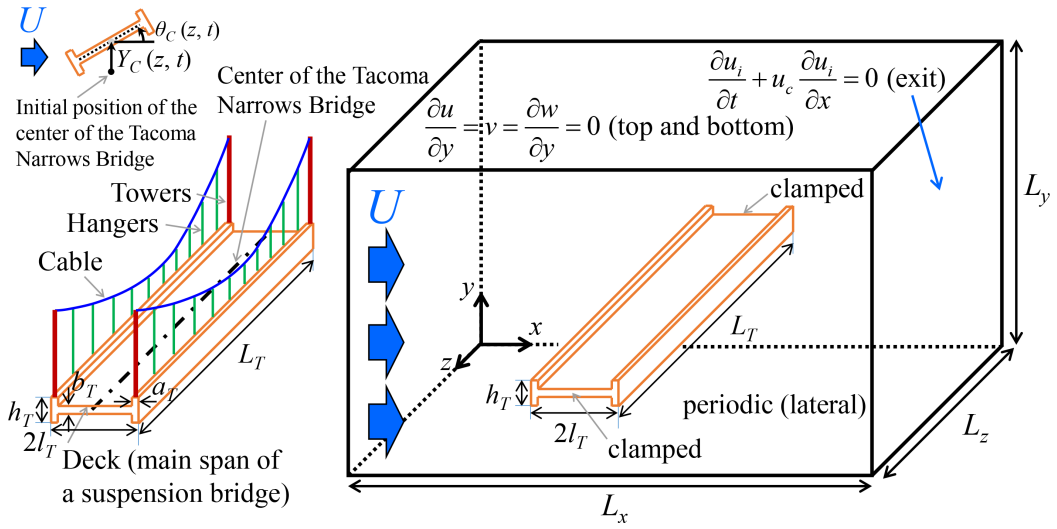

Figure 4.1. Schematic diagram of computational domain and boundary conditions for the simulation of flow around the Tacoma Narrows Bridge. Here, the effects of the cables, hangers, and towers are not considered for the simulation of flow around the Tacoma Narrows Bridge.

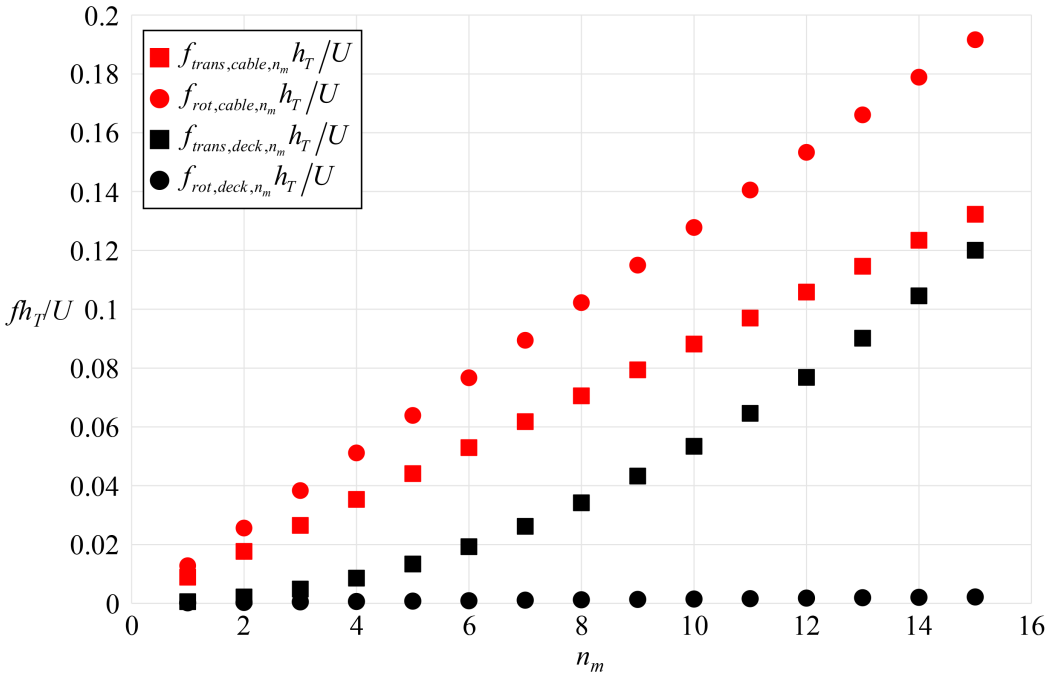

Figure 4.2. Theoretical natural frequencies of the cable and deck for the transverse and rotational motions with the mode.

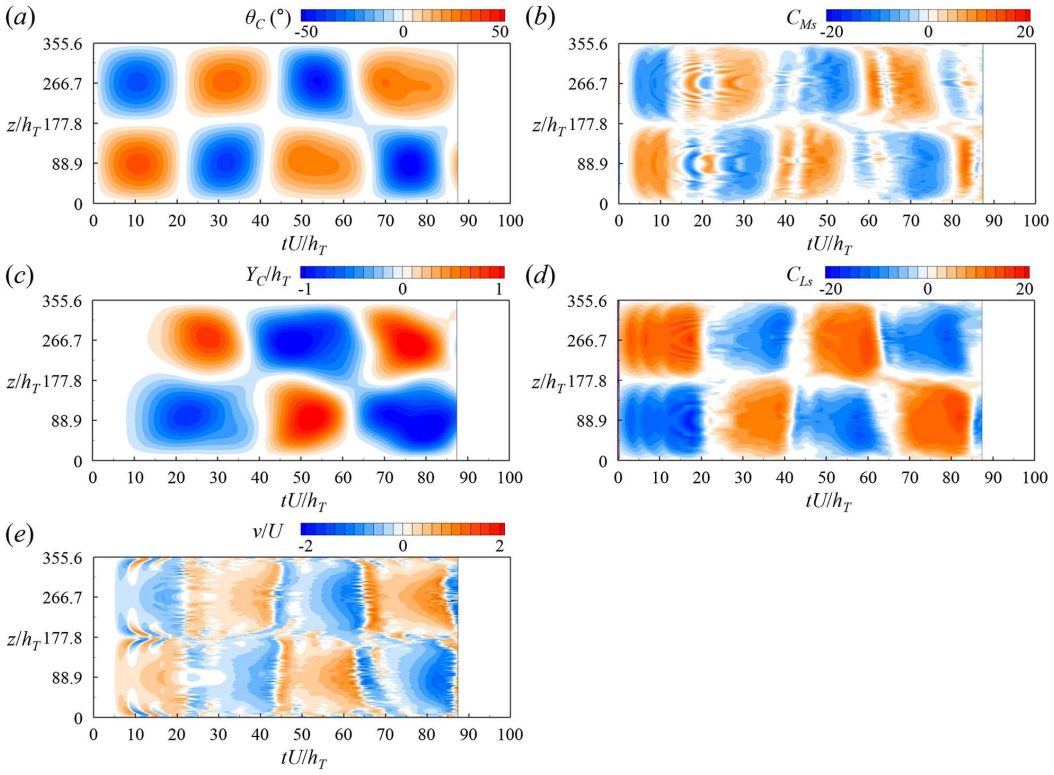

Figure 4.3. Time traces of the rotational angle, sectional moment coefficient, transverse displacement, sectional lift coefficient, and transverse velocity along the spanwise direction: (*a*) θ_C (°); (*b*) C_{Ms}; (*c*) Y_C/h_T; (*d*) C_{Ls} ; (*e*) v/U at $x/h_T = 5$ and $y = 0$.

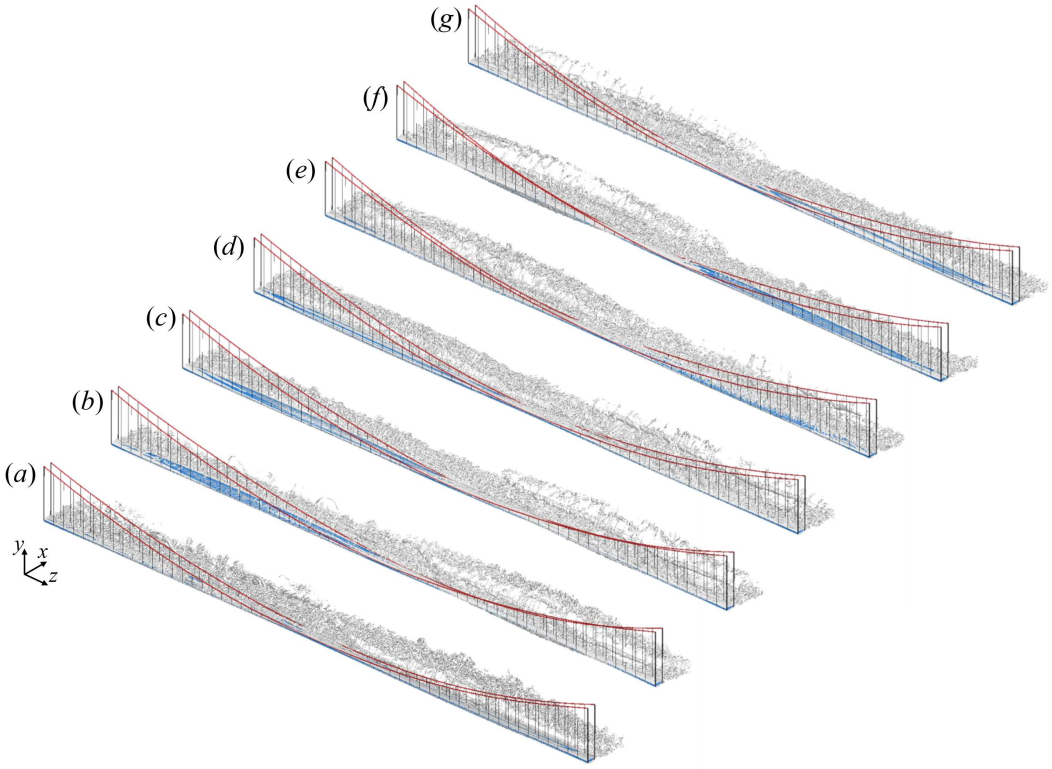

Figure 4.4. Instantaneous vortical structures around the Tacoma Narrows Bridge: (*a*) $tU/h_T = 45.5$; (*b*) 52.4; (*c*) 58.8; (*d*) 64.0; (*e*) 70.2; (*f*) 76.7; (*g*) 82.6.

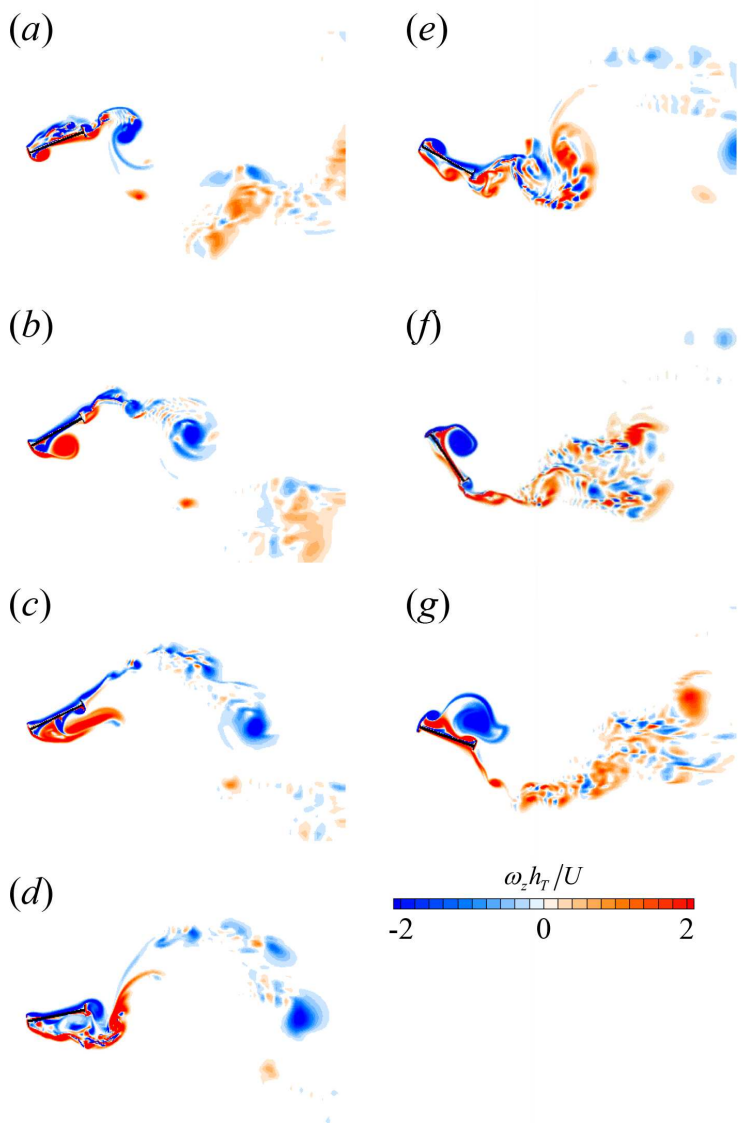

Figure 4.5. Contours of the instantaneous spanwise vorticity at $z/L_T = 0.25$: (*a*) $tU/h_T = 45.5$; (*b*) 52.4; (*c*) 58.8; (*d*) 64.0; (*e*) 70.2; (*f*) 76.7; (*g*) 82.6.

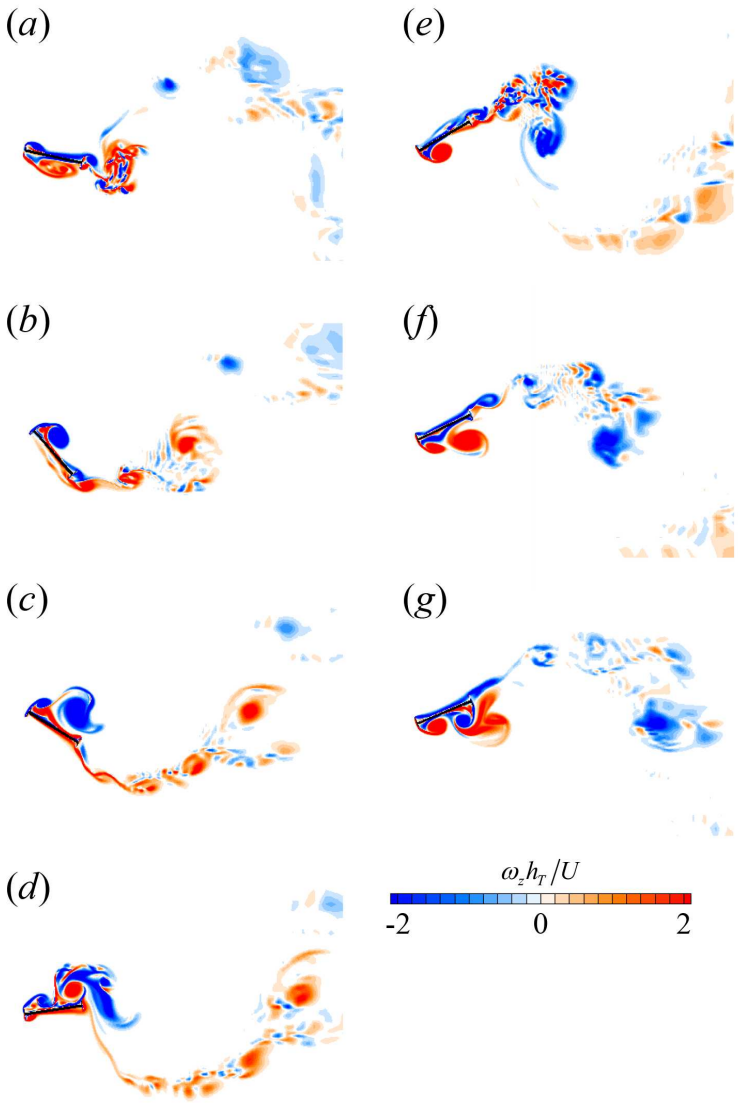

Figure 4.6. Contours of the instantaneous spanwise vorticity at $z/L_T = 0.75$: (a) $tU/h_T = 45.5$; (b) 52.4; (c) 58.8; (d) 64.0; (e) 70.2; (f) 76.7; (g) 82.6.

References

Ahmed, A. & Bays-Muchmore, B. 1992 Transverse flow over a wavy cylinder. *Phy. Fluids A.* **4**, 1959–1967.

Arioli, G. & Gazzola, F. 2017 Torsional instability in suspension bridges: the Tacoma Narrows Bridge case. *Commun. Nonlinear Sci. Numer. Simulat.* **42**, 342–357.

Bearman, P. W. 1984 Vortex shedding from oscillating bluff bodies. *Annu. Rev. Fluid Mech.* **16**, 195–222.

Bearman, P. W. 2011 Circular cylinder wakes and vortex-induced vibrations. *J. Fluids Struct.* **27**, 648–658.

Bearman, P. & Brankovic, M. 2004 Experimental studies of passive control of vortex-induced vibration. *Eur. J. Mech. B-Fluids* **23**, 9–15.

Beyer, R. P. & LeVeque, R. J. 1992 Analysis of a one-dimensional model for the immersed boundary method. *SIAM J. Numer. Anal.* **29**, 332–364.

Billah, K. Y. & Scanlan, R. H. 1991 Resonance, Tacoma Narrows bridge failure, and undergraduate physics textbooks. *Am. J. Phys.* **59**, 118–124.

Bistritz, Y. 1984 Zero location with respect to the unit circle of discrete-time linear system polynomials. *Proc. IEEE* **72**, 1131–1142.

Blackburn, H. M. & Karniadakis, G. E. 1993 Two-and three-dimensional simulations of vortex-induced vibration of a circular cylinder. *in: Third international Offshore and Polar Engineering Conference*, pp. 715–720.

Bleich, F. 1948 Dynamic instability of truss-stiffened suspension bridges under wind action. *Proc ASCE* **74**, 1269-1314.

Blevins, R. D. & Coughran, C. S. 2009 Experimental investigation of

vortex-induced vibration in one and two dimensions with variable mass, damping, and Reynolds number. *J. Fluids Eng.-Trans ASME* **131**, 101202.

Borazjani, I., Ge, L. & Sotiropoulos, F. 2008 Curvilinear immersed boundary method for simulating fluid structure interaction with complex 3D rigid bodies. *J. Comput. Phys.* **227**, 7587–7620.

Bourguet, R., Karniadakis, G. E. & Triantafyllou, M. S. 2011 Vortex-induced vibrations of a long flexible cylinder in shear flow. *J. Fluid Mech.* **677**, 342–382.

Breuer, M., De Nayer, G., Munsch, M., Gallinger, T. & Wuchner, R. 2012 Fluid-structure interaction using a partitioned semi-implicit predictor-corrector coupling scheme for the application of large-eddy simulation. *J. Fluids Struct.* **29**, 107–130.

Causin, P., Gerbeau, J. & Nobile, F. 2005 Added-mass effect in the design of partitioned algorithms for fluid-structure problems. *Comput. Methods Appl. Mech. Eng.* **194**, 4506–4527.

Chaplin, J. R., Bearman, P. W., Huarte, F. H. & Pattenden, R. J. 2005 Laboratory measurements of vortex-induced vibrations of a vertical tension riser in a stepped current. *J. Fluids Struct.* **21**, 3–24.

Choi, H. & Moin, P. 1994 Effects of the computational time step on numerical solutions of turbulent flow. *J. Comput. Phys.* **113**, 1–4.

Chung, J. & Hulbert, G. M. 1993 A time integration algorithm for structural dynamics with improved numerical dissipation: the generalized-α method. *J. Appl. Mech.* **60**, 371–375.

Dahl, J. M., Hover, F. S., Triantafyllou, M. S., Dong, S. & Karniadakis, G. E. 2007 Resonant vibrations of bluff bodies cause multivortex shedding and high frequency forces. *Phys. Rev. Lett.* **99**, 144503.

Deparis, S., Fernandez, M. A. & Formaggia, L. 2003 Acceleration of a fixed point algorithm for fluid-structure interaction using transpiration conditions. *Math. Model Numer. Anal.* **37**, 601–616.

Dettmer, W. G. & Peric, D. 2013 A new staggered scheme for fluid-structure interaction. *Int. J. Numer. Methods Eng.* **93**, 1–22.

Ding, Z. J., Balasubramanian, S., Lokken, R. T. & Yang, T. 2004 Lift and damping characteristics of bare and straked cylinders at riser scale Reynolds numbers. In *Offshore Technology Conference,* OTC-16341, Houston, TX.

Fadlun, E. A., Verzicco, R., Orlandi, P. & Mohd-Yusof, J. 2000 Combined immersed-boundary finite-difference methods for three-dimensional complex flow simulations. *J. Comput. Phys.* **161**, 35–60.

Farhat, C., Rallu, A., Wang, K. & Belytschko, T. 2010 Robust and provably second-order explicit-explicit and implicit-explicit staggered time-integrators for highly nonlinear compressible fluid-structure interaction problems. *Int. J. Numer. Methods Eng.* **84**, 73–107.

Farhat, C., van der Zee, K. G. & Geuzaine, P. 2006 Provably second-order time-accurate loosely-coupled solution algorithms for transient nonlinear computational aeroelasticity. *Comput. Methods Appl. Mech. Eng.* **195**, 1973–2001.

Farquharson, F. B. since June 1949 to June 1954 Aerodynamic stability of suspension bridges. *University of Washington Enginnering Experimental Stations Bulletin* No. 116, Pts. 1–5.

Felippa, C. A., Park, K. & Farhat, C. 2001 Partitioned analysis of coupled mechanical systems. *Comput. Methods Appl. Eng.* **190**, 3247–3270.

Feng, C. C. 1968 The measurements of vortex-induced effects in flow past a

stationary and oscillating circular and D-section cylinders. Master's thesis, University of British Columbia, Vancouver, B.C., Canada.

Fernandez, M. A. & Moubachir, M. 2005 A Newton method using exact jacobians for solving fluid-structure coupling. *Comput. Struct.* **83**, 127–142.

Forster, C., Wall, W. A. & Ramm, E. 2007 Artificial added mass instabilities in sequential staggered coupling of nonlinear structures and incompressible viscous flows. *Comput. Methods Appl. Mech. Eng.* **196**, 1278–1293.

Frank, W. R., Tognarelli, M. A., Slocum, S. T., Campbell, R. B. & Balasubramanian, S. 2004 Flow-induced vibration of a long, flexible, straked cylinder in uniform and linearly sheared currents. In *Offshore Technology Conference,* OTC-16340, Houston, TX.

Fuller, R. G., Lang, C. R., & Lang, R. H. 2008 Twin views of the Tacoma Narrows bridge collapse. *American Association of Physics*.

Gabbai, R. D. & Benaroya, H. 2005 An overview of modeling and experiments of vortex-induced vibration of circular cylinders. *J. Sound Vibr.* **282**, 576–616.

Gao, Y., Fu, S., Xiong, Y., Zhao, Y., & Liu, L. 2017 Experimental study on response performance of vortex-induced vibration on a flexible cylinder. *Ships Offshore Struct.* **12**, 116–134.

Gedikli, E. D. & Dahl, J. M. 2017 Mode excitation hysteresis of a flexible cylinder undergoing vortex-induced vibrations. *J. Fluids Struct.* **69**, 308–322.

Gerbeau, J. & Vidrascu, M. 2003 A quasi-Newton algorithm based on a reduced model for fluid-structure interaction problems in blood flows. *Math. Model. Numer. Anal.* **37**, 631–647.

Gilmanov, A., Le, T. B. & Sotiropoulos, F. 2015 A numerical approach for simulating fluid structure interaction of flexible thin shells undergoing arbitrarily large deformations in complex domains. *J. Comput. Phys.* **300**, 814–843.

Gilmanov, A. & Sotiropoulos, F. 2005 A hybrid Cartesian/immersed boundary method for simulating flows with 3D, geometrically complex, moving bodies. *J. Comput. Phys.* **207**, 457–492.

Goldstein, D., Handler, R. & Sirovich, L. 1993 Modeling a no-slip flow boundary with an external force field. *J. Comput. Phys.* **105**, 354–366.

Govardhan, R. & Williamson, C. H. K. 2000 Modes of vortex formation and frequency response of a freely vibrating cylinder. *J. Fluid Mech.* **420**, 85–130.

Green, D. & Unruh, W. G. 2006 Tacoma bridge failure: a physical model. *Am. J. Phys.* **74**, 706–716.

Gsell, S., Bourguet, R. & Braza, M. 2016 Two-degree-of-freedom vortex-induced vibrations of a circular cylinder at Re = 3900. *J. Fluids Struct.* **67**, 156–172.

Hinton, E., Rock, T. & Zienkiewicz, O. C. 1976 A note on mass lumping and related processes in the finite element method. *Earthq. Eng. Struct. D.* **4**, 245–249.

Hou, G., Wang, J. & Layton, A. 2012 Numerical methods for fluid-structure interaction-a review. *Commun. Comput. Phys.* **12**, 337–377.

Huang, S. 2011 VIV suppression of a two-degree-of-freedom circular cylinder and drag reduction of a fixed circular cylinder by the use of helical grooves. *J. Fluids Struct.* **27**, 1124–1133.

Huang, W.-X. & Sung, H. J. 2009 An immersed boundary method for fluid-

flexible structure interaction. *Comput. Methods Appl. Mech. Eng.* **198**, 2650–2661.

Huera-Huarte, F. J., Bangash, Z. A., & Gonzalez, L. M. 2014 Towing tank experiments on the vortex-induced vibrations of low mass ratio long flexible cylinders. *J. Fluids Struct.* **48**, 81–92.

Irons, B. M. & Tuck, R. C. 1969 A version of the Aitken accelerator for computer iteration. *Int. J. Numer. Methods Eng.* **1**, 275–277.

Jauvtis, N. & Williamson, C. H. K. 2004 The effect of two degrees of freedom on vortex-induced vibration at low mass and damping. *J. Fluid Mech.* **509**, 23–62.

Jeong, J. & Hussain, F. 1995 On the indentification of a vortex. *J. Fluid Mech.* **285**, 69–94.

Jung, J. H. & Yoon, H. S. 2014 Large eddy simulation of flow over a twisted cylinder at a subcritical Reynolds number. *J. Fluid Mech.* **759**, 579–611.

Khalak, A. & Williamson, H. K. 1999 Motions, forces and mode transitions in vortex-induced vibrations at low mass-damping. *J. Fluids Struct.* **13**, 813–851.

Kang, Z., Ni, W. & Sun, L. 2017 A numerical investigation on capturing the maximum transverse amplitude in vortex induced vibration for low mass ratio. *Mar. Struct.* **52**, 94–107.

von Karman, T. & Edson, L. 1967 The wind and beyond. Little, Brown & Company

Kassiotis, C., Ibrahimbegovic, A., Niekamp, R. & Matthies, H. G. 2011 Nonlinear fluid-structure interaction problem. Part I: implicit partitioned algorithm, nonlinear stability proof and validation examples. *Comput. Mech.* **47**, 305–323.

Kim, K., Baek, S.-J. & Sung, H. J. 2002 An implicit velocity decoupling procedure for the incompressible Navier-Stokes equations. *Int. J. Numer. Methods Fluids* **38**, 125–138.

Kim, J., Kim, D. & Choi, H. 2001 An immersed-boundary finite-volume method for simulations of flow in complex geometries. *J. Comput. Phys.* **171**, 132–150.

Kim, W., Lee, J. & Choi, H. 2016 Flow around a helically twisted elliptic cylinder. *Phys. Fluids* **28**, 053602.

Kuttler, U. & Wall, W. A. 2008 Fixed-point fluid-structure interaction solvers with dynamic relaxation. *Comput. Mech.* **43**, 61–72.

Lai, M.-C. & Peskin, C. S. 2000 An immersed boundary method with formal second-order accuracy and reduced numerical viscosity. *J. Comput. Phys.* **160**, 705–719.

Lam, K. & Lin, Y. F. 2009 Effects of wavelength and amplitude of a wavy cylinder in cross-flow at low Reynolds numbers. *J. Fluid Mech.* **620**, 195–220.

Le Tallec, P. & Mouro, J. 2001 Fluid structure interaction with large structural displacements. *Comput. Methods Appl. Mech. Eng.* **190**, 3039–3067.

Lee, I. & Choi, H. 2015 A discrete-forcing immersed boundary method for the fluid-structure interaction of an elastic slender body. *J. Comput. Phys.* **280**, 529–546.

Lee, J., Kim, J., Choi, H. & Yang, K.-S. 2011 Sources of spurious force oscillations from an immersed boundary method for moving-body problems. *J. Comput. Phys.* **230**, 2677–2695.

Lee, J. & You, D. 2013 An implicit ghost-cell immersed boundary method

for simulations of moving body problems with control of spurious force oscillations. *J. Comput. Phys.* **233**, 295–314.

Lee, J., Choi, H. & Park, N. 2010 Dynamic global model for large eddy simulation of transient flow. *Phys. Fluids* **22**, 075106.

Luhar, M. & Nepf, H. M. 2011 Flow-induced reconfiguration of buoyant and flexible aquatic vegetation. *Limnol. Oceanogr.* **56**, 2003–2017.

Lucor, D., Mukundan, H. & Triantafyllou, M. S. 2006 Riser modal identification in CFD and full-scale experiments. *J. Fluids Struct.* **22**, 905–917.

Luo, H., Mittal, R., Zheng, X., Bielamowicz, S. A., Walsh, R. J. & Hahn, J. K. 2008 An immersed-boundary method for flow-structure interaction in biological systems with application to phonation. *J. Comput. Phys.* **227**, 9303–9332.

Matthies, H. G. & Steindorf, J. 2003 Partitioned strong coupling algorithms for fluid-structure interaction. *Comput. Struct.* **81**, 805–812.

Matthies, H. & Strang, G. 1979 The solution of nonlinear finite element equations. *Int. J. Numer. Methods Eng.* **14**, 1613–1626.

Mckenna, P. J. 1999 Large torsional oscillations in suspension bridges revisited: fixing an old approximation. *Am. Math. Mon.* **106**, 1–18.

Mittal, R. & Iaccarino, G. 2005 Immersed boundary methods. *Annu. Rev. Fluid Mech.* **37**, 239–261.

Newman, D. J. & Karniadakis, G. E. 1997 A direct numerical simulation study of flow past a freely vibrating cable. *J. Fluid Mech.* **344**, 95–136.

Norberg, C. 2003 Fluctuating lift on a circular cylinder: review and new measurements. *J. Fluids Struct.* **17**, 57–96.

Owen, J. C., Bearman, P. W. & Szewczyk, A. A. 2001 Passive control of VIV with drag reduction. *J. Fluids Struct.* **15**, 597–605.

Park, N., Lee, S., Lee, J., & Choi, H. 2006 A dynamic subgrid-scale eddy viscosity model with a global model coefficient. *Phys. Fluids* **18**, 125109.

Peskin C. S. 1972 Flow patterns around heart valves: a numerical method. *J. Comput. Phys.* **10**, 252–271.

Piperno, S., Farhat, C. & Larrouturou, B. 1995 Partitioned procedures for the transient solution of coupled aeroelastic problems Part I: Model problem, theory and two-dimensional application. *Comput. Methods Appl. Mech. Eng.* **124**, 79–112.

Piperno, S. & Farhat, C. 2001 Partitioned procedures for the transient solution of coupled aeroelastic problems - Part II: energy transfer analysis and three-dimensional applications. *Comput. Methods Appl. Mech. Eng.* **190**, 3147–3170.

Pittel, B. G. & Yakubovich, V. A. 1961 Application of the theory of parametric resonance to explain the collapse of the Tacoma Narrows Bridge (Russian). *Uspekhi Mat. Nauk* **15**, 183–184.

Pittel, B. G. & Yakubovich, V. A. 1969 A mathematical analysis of the stability of suspension bridges based on the example of the Tacoma Bridge (Russian) *Vestnik Leningrad Univ* **24**, 80–91.

Quen, L. K., Abu, A., Kato, N., Muhamad, P., Sahekhaini, A. & Abdullah, H. 2014 Investigation on the effectiveness of helical strakes in suppressing VIV of flexible riser. *Appl. Ocean Res.* **44**, 82–91.

Sarpkaya, T. 2004 A critical review of the intrinsic nature of vortex-induced vibrations. *J. Fluids Struct.* **19**, 389–447.

Saiki, E. M. & Biringen, S. 1996 Numerical simulation of a cylinder in

uniform flow: application of a virtual boundary method. *J. Comput. Phys.* **123**, 450–465.

Scott, R. 2001 In the wake of Tacoma. Suspension bridges and the quest for aerodynamic stability. *ASCE, Reston*.

Song, J. N., Lu, L., Teng, B., Park, H. I., Tang, G. Q. & Wu, H. 2011 Laboratory tests of vortex-induced vibrations of a long flexible riser pipe subjected to uniform flow. *Ocean Eng.* **38**, 1308–1322.

Sui, J., Wang, J., Liang, S. & Tian, Q. 2016 VIV suppression for a large mass-damping cylinder attached with helical strakes. *J. Fluids Struct.* **62**, 125–146.

Tezduyar T. E. 2001 Finite element methods for flow problems with moving boundaries and interfaces. *Arch. Comput. Methods Eng.* **8**, 83–130.

Tian, F.-B., Dai, H., Luo, H., Doyle, J. F. & Rousseau, B. 2014 Fluid-structure interaction involving large deformations: 3D simulations and applications to biological systems. *J. Comput. Phys.* **258**, 451–469.

Trim, A. D., Braaten, H., Lie, H. & Tognarelli, M. A. 2005 Experimental investigation of vortex-induced vibration of long marine risers. *J. Fluids Struct.* **21**, 335–361.

Turek, S. & Hron, J. 2006 Proposal for numerical benchmarking of fluid-structure interaction between an elastic object and laminar incompressible flow. *in: H.J. Bungartz, M. Schafer (Eds.), Fluid-Structure interaction: Modelling, Simulation, Optimisation, Springer-Verlag, Berlin, Heidelberg, Netherlands*, pp. 371–385.

van Brummelen E. H. 2009 Added mass effects of compressible and incompressible flows in fluid-structure interaction. *J. Appl. Mech.* **76**, 021206.

Vandiver, J. K. 1993 Dimensionless parameters important to the prediction

of vortex-induced vibration of long, flexible cylinders in ocean currents. *J. Fluids Struct.* **7**, 423–455.

Vandiver, J. K., Allen, D. & Li, L. 1996 The occurrence of lock-in under highly sheared conditions. *J. Fluids Struct.* **10**, 555–561.

Vandiver, J. K., Swithenbank, S., Jaiswal, V., & Marcollo, H. 2006 The effectiveness of helical strakes in the suppression of high-mode-number VIV. In *Offshore Technology Conference,* OTC-18276, Houston, TX.

Vandiver, J. K., Jaiswal, V. & Jhingran, V. 2009 Insights on vortex-induced, traveling waves on long risers. *J. Fluids Struct.* **25**, 641–653.

Wang, E. & Xiao, Q. 2016 Numerical simulation of vortex-induced vibration of a vertical riser in uniform and linearly sheared currents. *Ocean Eng.* **121**, 492–515.

Weeratunga, S. & Pramono, E. 1994 Direct coupled aeroelastic analysis through concurrent implicit time integration on a parallel computer. *AIAA Paper No. 94-1550*.

Williamson, C. H. K. & Govardhan, R. 2004 Vortex-induced vibrations. *Annu. Rev. Fluid Mech.* **36**, 413–455.

Williamson, C. H. K. & Govardhan, R. 2008 A brief review of recent results in vortex-induced vibrations. *J. Wind Eng. Ind. Aerodyn.* **96**, 713–735.

Williamson, C. H. K. & Roshko, A. 1988 Vortex formation in the wake of an oscillating cylinder. *J. Fluids Struct.* **2**, 355–381.

Wu, X., Ge, F. & Hong, Y. 2012 A review of recent studies on vortex-induced vibrations of long slender cylinders. *J. Fluids Struct.* **28**, 292–308.

Yakubovich, V. A. & Starzhinskii, V. M. 1975 Linear differential equations with periodic coefficients, vol. 2. Wiley.

Yang, J. & Balaras, E. 2006 An embedded-boundary formulation for large-eddy simulation of turbulent flows interacting with moving boundaries. *J. Comput. Phys.* **215**, 12–40.

Yang, J., Preidikman, S. & Balaras, E. 2008 A strongly coupled, embedded-boundary method for fluid-structure interactions of elastically mounted rigid bodies. *J. Fluids Struct.* **24**, 167–182.

Yang, J. & Stern, F. 2015 A non-iterative direct forcing immersed boundary method for strongly-coupled fluid-solid interactions. *J. Comput. Phys.* **295**, 779–804.

Zdravkovich, M. M. 1981 Review and classification of various aerodynamic and hydrodynamic means for suppressing vortex shedding. *J. Wind Eng. Ind. Aerodyn.* **7**, 145–189.

Zhao, M., Tong, F. & Cheng, L. 2012 Numerical simulation of two-degree-of-freedom vortex-induced vibration of a circular cylinder between two lateral plane walls in steady currents. *J. Fluids Eng.-Trans. ASME* **134**, 104501.

Zhou, T., Razali, S. M., Hao, Z. & Cheng, L. 2011 On the study of vortex-induced vibration of a cylinder with helical strakes. *J. Fluids Struct.* **27**, 903–917.

큰 진폭 진동의 유체–구조물 상호 작용과 수동 제어

서울대학교 대학원
기계항공공학부
김우진

요 약

본 연구에서는 고체와 유체의 저밀도 비(ρ)에서 유체–구조물 상호작용을 위한 약한 결합법을 제시하고 다음의 구조물 주위 유동에 대한 비정상 3차원 시뮬레이션을 수행한다. 구조물은 탄성 강체 원형 실린더와 나선형 비틀림 타원(HTE) 실린더, 직선형 전단류에서의 유연 원형 및 HTE 실린더, 그리고 타코마 브릿지이다.

약한 결합법에서 정확하고 안정적인 해를 얻기 위해 각 시간 단계에서 유체–구조물 경계의 임시 속도와 위치를 예측하는 예측기(명시적 2단계 방법 및 임시적 오일러 방법)를 도입한다. 비압축성 나비에–스토크스 방정식은 유체–구조물 경계면에서의 임시 속도 및 위치와 엇갈림 격자에서 가상 경계 방법 및 유한 체적 방법을 사용하여 오일러 좌표로 풀린다. 유체 및 구조물에 대한 각 지배방정식은 2차 시간 적분기를 사용하여 임시적으로 해결된다. 전반적인 2차 시간 정확도는 낮은 정확도의 예측기를 사용하더라도 보존된다. 또한 선형 안정성 분석은 가장 낮은 밀도 비로 안정적인 해를 제공하는 최적의 명시적 2단계 방법을 찾기 위한 이상적인 경우에 대해 수행되었다. 현재의 약한 결합법으로 3가지 다른 유체–구조물 상호 작용 문제에 대해 시뮬레이션을 하였다. 탄성 강체 원형 실린더, 고정된 원형 실린더의 베이스에 부착된 탄성 빔, 그리고 유연 플레이트($\rho = 0.678$) 주위 유동이다. 안정된 해를 제공하는 최저 밀도 비는 처음 두 가지 문제에 대해 탐색되며 1보다 훨씬 낮다(각각 $\rho_{min} = 0.21$과 0.31). 시뮬레이션 결과는 제안된 강한 결합법과 이전의 수치 및 실험 연구 결과와 잘 일치하며 현재의 약한 결합법의 효율성과 정확도를 나타낸다.

탄성 강체 원형 실린더 주위 유동 시뮬레이션은 2의 질량비, 6의 환산 속도, 0의 감쇠비 및 4200의 레이놀즈 수를 갖는다. $1.19D$의 횡 방향 변위 진폭을 갖는 진동은 원형 실린더의 횡 방향 두 면에서의 큰 압력차에 의해 유도된다. 여기서 D는 원형 실린더의 직경 또는 HTE 실린더의 장축과 단축의 길이 곱의 제곱근이

다. 전방 및 후방에서 발생된 전단층에서 생성된 시작 와류에 의해 유도된 유동이 원형 실린더의 횡방향 면에 충돌함으로 인해 실린더의 횡 방향 이동과 반대되는 면에서 압력이 높고 다른 면은 유동 가속과 박리 지연으로 인해 압력이 낮다. 한편, 큰 진폭 진동을 억제하기 위해 탄성 강체 HTE 실린더의 파장(λ_H) 및 종횡비(AR_H)에 대한 매개 변수 연구가 수행된다. AR_H = 2.6 및 λ_H = 10D을 가지는 탄성 강체 HTE 실린더의 경우 유동에 의한 진동이 완전히 억제되고 평균 항력 계수는 탄성 강체 원형 실린더에 비해 현저히 감소하지만 고정 원형 실린더 보다는 약간 더 크다.

유연한 원형 실린더 주위 유동 시뮬레이션은 7.64의 질량비, 4.55의 인장 계수, 9.09의 굽힘 계수, 3.67의 최소 속도에 대한 최대 속도의 비, 200의 직경에 대한 길이의 비, 선형 전단류 유입에서의 최대 속도에 기반한 레이놀즈 수 330을 갖는다. 락인 현상은 고속 영역에서 0.148, 0.162 및 0.174의 세 가지 주파수에 대해 발생하며, 이는 다중 모드 응답을 유도하고 고속 영역에서 저속 영역으로 전파하는 진행파를 유도한다. 횡 방향 변위 진폭은 1D보다 작으며 정상파와 진행파가 관찰된다. 후류에서는 주기 당 2개의 단일 와류가 생성된다(2S 모드). 한편, 유연한 원형 실린더 주위 유동 시뮬레이션은 2.55의 질량비, 5의 인장 계수, 10의 굽힘 계수, 9의 최소 속도에 대한 최대 속도의 비, 선형 전단류에서의 최대 속도에 기반한 레이놀즈 수 4000을 갖는다. 유연한 원형 실린더는 길이의 2배 파장으로 진동한다(mode 1). 횡방향 변위 진폭은 2D보다 크고 유동 방향 변위는 유연한 원형실린더 중간 부근에서 심하게 변동한다. 전단층으로부터 강한 시작 와류가 발생하고 실린더의 이동 방향의 반대쪽 근처에 위치한다. 다중 모드 및 단일 모드 응답의 경우 모두, AR_H = 2.6 및 λ_H = 10D인 유연한 HTE 실린더는 유동으로 인한 진동을 완전히 억제하고 흐름 방향으로의 처짐을 감소시킨다.

타코마 브릿지 주위 유동은 갑판 높이를 기준으로 레이놀즈 300에서 시뮬레이션된다. 타코마 브릿지가 길이의 1배 파장으로 비틀림 진동할 때 타코마 브릿지 뒤의 와류 흘림은 스팬 방향 및 횡 방향을 따라 번갈아 생성된다. 타코마 브릿지의 비틀림 진동은 선단 소용돌이와 상호 작용한다. 갑판 단면의 더 높은 받음각으로 인해 선단 소용돌이가 강해지고 선단 소용돌이가 강해지면 데크에서 더 높은 모멘트가 발생한다. 비틀림 진동을 겪고 있는 타코마 브릿지 후류에서의 와류 방출 주파수는 정지된 타코마 브릿지 후류에서의 와류 방출 주파수 보다는 훨씬 낮은 반면 케이블에 의해 유도된 비틀림 고유 주파수와는 잘 일치한다.

……

주요어: 유체-구조물 상호 작용, 큰 진폭 진동, 와류, 뭉툭한 물체, 수동 제어
학 번: 2010-20661